الجمهورية الجزائرية الديمقراطية الشعبية

People's Democratic Republic of Algeria

وزارة التعليم العالي و البحث العلمي

Ministry of Higher Education and Scientific Research

جامعة أبي بكر بلقايد -- تلمسان

University of Abou Bekr Belkaid – Tlemcen

كلية التكنولوجيا

Faculty of Technology

Laboratory of Computational Mechanics

THESIS

Presented in Partial fulfillment of the requirements for the degree of **DOCTORATE** (3rd cycle)

in Mechanical Engineering

Specialty: Computational Mechanics

Presented by: **Lakhdar ZEDDOUNE**

Subject

Design and Optimization Study of Shell Structures Made of Advanced Materials Under Different Types of Loadings

Publicly defended on 23/01/2025, in front of the thesis committee:

Benachour Mustapha	Professor	Univ. Tlemcen	Chairman
Belalia Sid Ahmed	Professor	Univ. Tlemcen	Supervisor
Chorfi Sidi Mohammed	Assoc.Prof (Class 'A')	Univ. Tlemcen	Co-Supervisor
Bensaid Ismail	Assoc.Prof (Class 'A')	Univ. Tlemcen	Examiner
Nadjib Serdoun	Assoc.Prof (Class 'A')	Univ. Tlemcen	Examiner

Academic year:2024-2025

بسم الله الرحمن الرحيم

I would like to dedicate this thesis to my MOTHER

Acknowledgments

I would like to express my profound gratitude to **Pr.Belalia Sid-Ahmed** for his invaluable guidance and support throughout the course of my research. His expertise and insightful advice have greatly contributed to the successful completion of this thesis.
My deepest appreciation is also extended to **Dr.Chorfi Sidi Mohammed**, whose academic mentorship has been of immense value. Beyond his guidance and constructive feedback, his unwavering emotional support provided me with the resilience needed to persevere. Without this support, the completion of this work would not have been possible.
I am deeply grateful to the president of the jury,**Pr.Benachour Mustapha**, for presiding over the evaluation of this work and ensuring the smooth execution of the defense process. I also wish to extend my heartfelt thanks to the distinguished members of the jury **Dr.Bensaid Ismail** & **Dr.Serdoun Nadjib** for their time, effort, and insightful feedback, which have been invaluable in refining this research.
Finally, I wish to acknowledge the enduring support of my **father** and **mother**. Their encouragement, understanding, and belief in my abilities have been a source of strength throughout my academic journey.

ملخص

يؤدي التقدم المستمر في التكنولوجيا إلى مشاريع معقدة بشكل متزايد، وهي أكثر تكلفة من الناحية الحسابية. تمثل الأشكال الهندسية للألواح المنحنية تعقيدات إضافية، بما في ذلك الانحناء والسماكة المتفاوتة، والتي يمكن أن تجعل صياغة وتنفيذ العناصر المنحنية المزدوجة أكثر صعوبة من عناصر العوارض والألواح الأبسط. وعلاوة على ذلك، فإنها غالباً ما تتطلب موارد حسابية أعلى وتقنيات عددية أكثر تعقيداً لالتقاط سلوكها بدقة، مما يؤدي إلى زيادة التكلفة الحسابية والتعقيد. بالإضافة إلى ذلك، يستلزم تطوير العناصر المنحنية المضاعفة والتحقق من صحتها إجراء اختبارات تجريبية ورقمية مكثفة، مما قد يحد من توافر تركيبات دقيقة وموثوقة مقارنةً بعناصر العارضة والصفائح. وأخيراً، عادةً ما يكون تطبيق العناصر المنحنية المزدوجة أكثر تخصصاً وتحديداً لصناعات أو تخصصات هندسية معينة، مما يؤدي إلى تركيز بحثي أضيق نطاقاً مقارنةً بالتطبيق الأوسع لعناصر العوارض والألواح في مختلف المجالات.

في السنوات الأخيرة، اكتسبت النسخة p من طريقة العناصر المحدودة أهمية كبيرة نظراً لدقتها العالية ومعدلات تقاربها الأسرع مقارنةً بالطرق التقليدية، حيث تتطلب درجات حرية أقل للحصول على نتائج دقيقة. وهي توفر تمثيلاً أفضل للأشكال الهندسية المعقدة، وزيادة المرونة في تكييف الشبكات، وتقليل التذبذبات الزائفة في الحلول، مما يجعلها أداة قيمة للمحاكاة الهندسية. من خلال الاستفادة من نظرية الغلاف السميك، يتم دمج الإصدار p من طريقة العناصر المحدودة مع نظرية تشوه القص من الدرجة الثالثة (TSDT) لتطوير نوع جديد من عناصر الغلاف من الإصدار . تم تطوير كود حاسوبي يعتمد على هذا النوع من العناصر واختباره والتحقق من صحته بنجاح. تم تقييم أداء الكود ومتانته من خلال تحليل مجموعة واسعة من الهياكل الصدفية التي تُظهر سلوك الاهتزاز الحر والانحناء والالتواء الحراري، والمواد متساوية الخواص وثنائية الاتجاه المتدرجة وظيفياً، والأشكال الهندسية الاعتباطية. يتم عرض الصيغة الرياضية وهيكل الكود والنتائج في الأقسام التالية.

الكلمات المفتاحية: لوحة منحنية مزدوجة؛ النسخة p من طريقة العناصر المحدودة؛ العنصر المحدود؛ مادة متساوية الخواص؛ مادة متدرجة وظيفياً ثنائية الاتجاه؛ اهتزاز حر؛ انحناء؛ التواء حراري.

Abstract

The ongoing advancement in technology leads to increasingly intricate projects, which are more computationally expensive. Shell geometries present additional complexities, including varying curvature and thickness, which can render the formulation and implementation of shell elements more challenging than simpler beam and plate elements. Moreover, they often demand higher computational resources and more sophisticated numerical techniques to accurately capture their behavior, resulting in increased computational cost and complexity. Additionally, the development and validation of shell elements entail extensive experimental and numerical testing, potentially limiting the availability of accurate and reliable formulations compared to beam and plate elements. Lastly, the application of shell elements is typically more specialized and specific to certain industries or engineering disciplines, leading to a narrower research focus compared to the broader applicability of beam and plate elements across various fields.

In recent years, the p-version of the finite element method has gained prominence due to its higher accuracy and faster convergence rates compared to traditional methods, requiring fewer degrees of freedom for accurate results. It provides better representation of complex geometries, increased flexibility in mesh adaptation, and reduced spurious oscillations in solutions, making it a valuable tool for engineering simulations. By leveraging the thick shell theory, the p-version of the finite element method is combined with the third-order shear deformation theory (TSDT) to develop a new type of p-version shell element. A computer code based on this element type has been developed, tested, and successfully validated. The code's performance and robustness were assessed through the analysis of a wide range of shell structures exhibiting free vibration, bending, and thermal buckling behavior, isotropic and bi-directional functionally graded materials, and arbitrary geometrical shapes. The mathematical formulation, code structure, as well as results, are presented in the following sections.

Keywords: doubly curved shell panel;the p-version of finite element method; shell finite element; isotropic material;bi-directional functionally graded material;free vibration;bending;thermal buckling.

Résumé

Les progrès continus de la technologie conduisent à des projets de plus en plus complexes, qui sont plus coûteux en termes de calcul. Les géométries de coque présentent des complexités supplémentaires, notamment des courbures et des épaisseurs variables, ce qui peut rendre la formulation et la mise en œuvre des éléments de coque plus difficiles que celles des éléments plus simples tels que les poutres et les plaques. De plus, elles demandent souvent des ressources computationnelles plus élevées et des techniques numériques plus sophistiquées pour capturer avec précision leur comportement, ce qui se traduit par un coût et une complexité computationnels accrus. De plus, le développement et la validation des éléments de coque nécessitent des tests expérimentaux et numériques approfondis, limitant potentiellement la disponibilité de formulations précises et fiables par rapport aux éléments de poutre et de plaque. Enfin, l'application des éléments de coque est généralement plus spécialisée et spécifique à certains secteurs industriels ou disciplines de l'ingénierie, ce qui entraîne une attention plus étroite de la recherche par rapport à l'applicabilité plus large des éléments de poutre et de plaque dans différents domaines. Ces dernières années, la méthode des éléments finis en version p a gagné en importance en raison de sa précision accrue et de ses taux de convergence plus rapides par rapport aux méthodes traditionnelles, nécessitant moins de degrés de liberté pour des résultats précis. Elle offre une meilleure représentation des géométries complexes, une plus grande flexibilité dans l'adaptation du maillage et une réduction des oscillations parasites dans les solutions, ce qui en fait un outil précieux pour les simulations d'ingénierie. En combinant la théorie de la coque épaisse avec la méthode des éléments finis en version p, la théorie de la déformation de cisaillement du troisième ordre (TSDT) est utilisée pour développer un nouveau type d'élément de coque en version p. Un code informatique basé sur ce type d'élément a été développé, testé et validé avec succès. Les performances et la robustesse du code ont été évaluées à travers l'analyse d'une large gamme de structures de coque présentant des comportements de vibration libre, de flexion et de flambage thermique, de matériaux isotropes et bidirectionnels à gradient fonctionnel, ainsi que de formes géométriques arbitraires. La formulation mathématique, la structure du code, ainsi que les résultats, sont présentés dans les sections suivantes.

Mots Clés : coque doubelement courbe, la version p de la method des elements finis, element finis des coques, materiau isotrope, materiau gradue fonctionnellement bi-directionel, vibration libre, flexion, flambage thermique.

Contents

List of Figures

List of Tables

List of Symbols

$u(x, y, z)$	displacement in x-direction	16
$v(x, y, z)$	displacement in y-direction	16
$w(x, y, z)$	displacement in z-direction	16
u_0, v_0, w_0	displacements of the neutral plane	16
θ_x, θ_y	rotations	16
$\overline{u_0}, \overline{v_0}, \overline{\theta_x}, \overline{\theta_y}$	displacements higher order terms	16
$\{\delta_0\}$	generalized displacements array	16
$\{\varepsilon\}$	Strain array	16
R_x, R_y	Radius of curvature in x as well y-directions	16
n_x, n_z	gradient indexes in x and z directions	17
T	Temperature	18
ΔT	Temperature change	18
T_b	Temperature at the bottom of the shell	18
T_t	Temperature at the top of the shell	18
$P_{c/m}(T)$	mechanical property of Ceramic/metal	17
$P_c(T)$	mechanical property of Ceramic	17
$P_m(T)$	mechanical property of Metal	17
$P(z, x, T)$	mechanical property of bi-FGM	17
$P_0, P_{-1}, P_1, P_2, P_3$	Material properties coefficients	17
$k_{(z,x)}$	Thermal conductivity	18
k_c	Thermal conductivity of ceramic	18
k_m	Thermal conductivity of metal	18
$\{\varepsilon_{thermal}\}$	Thermal strain array	19
$\{\sigma\}$	Stress array	19
$E_{(z,x)}$	Young Modulus	19
$\nu_{(z,x)}$	Poison Ratio	19
$\alpha_{(z,x)}$	Thermal expansion coefficient	19
$[C]$	Elastic Coefficient matrix	19

Glossary

BFGP Bi-directional functionally graded porous. 8

bi-FGM bi-directional Functionally graded material. vii, 1–7, 12, 13, 17, 37, 84, 105, 110, 111, 117

CAD Computer Aided Design. 14, 31

CST Classical shell theory. 12, 66

DQM Differential Quadrature Method. 5, 6, 8, 9, 90, 91

ESDT exponential shear deformation theory. 66

FEA Finite Element Analysis. 34

FEM Finite element method. 7, 8, 12–14, 30–33, 36, 121, 122

FG Functionally graded. 11, 12, 19, 22, 24, 25, 38–40, 60, 61, 84, 90, 121, 123, 124

FGM Functionally graded material. i, iv, v, 1, 2, 4–11, 14, 15, 19, 28, 39–41, 44–49, 54–57, 59, 63, 65, 67, 69, 76, 78–80, 83, 84, 86, 87, 89, 93, 95, 96, 107, 110, 112, 114, 119, 123

FSDT first order shear deformation theory. 5–10, 12, 66, 90, 91

GDQM Generalized Differential Quadrature Method. 6, 7

HSDT Hyperbolic shear deformation theory. 10, 14, 16, 37, 40, 64–66, 119, 122

IHSDT Inverse-Hyperbolic shear deformation theory. 8

iTrSDT inverse trigonometric shear deformation theory. 41–44

LENS Laser-Engineered Net Shaping technique. 4

MCST Modified-Couple-Stress-Theory. 8, 10

NSDT N-th Order Shear deformation theory. 90, 91

NURBS Non-Uniform Rational B-Spline. 8, 125

PSDT Parabolic shear deformation theory of Reddy. 66

Q3D Quasi three dimensional. 41–44

RBCM Radial Basis Collocation Method. 5

SSDT Sinusoidale shear deformation theory. 41, 42

TD Temperature-dependent material. 11, 98–102, 104, 105, 117

TID Temperature-Independent material. ii, iii, v, 11, 92, 98–105, 107, 108, 110, 111, 113–115, 117, 118

TSDT third order shear deformation theory. 1, 2, 8, 9, 11, 12, 33, 41–44, 60, 66, 67, 121

General Introduction

In recent years, the study and design of functionally graded materials (FGMs) have gained considerable interest in structural engineering due to their unique mechanical properties and their potential for optimization in a wide range of applications. FGMs are characterized by gradual variations in material composition and properties across their volume, allowing for tailored performance to meet specific design requirements. This makes them especially suitable for structural components subjected to complex loading conditions and diverse environmental exposures.

Among the different types of FGMs, bi-directional functionally graded materials (bi-FGMs) stand out as an important area of research. With material gradations occurring in two directions and complex geometries, bi-FGM shell panels present unique challenges in terms of mechanical behavior and structural analysis. Understanding how these materials respond under various loading conditions is essential for designing and optimizing their performance in industries such as aerospace, automotive, marine, and civil engineering.

This thesis is focused on a comprehensive conception study of shell panels, where the free vibration, thermal buckling, and static bending analyses form the backbone of the investigation. These types of analyses are critical for assessing the structural integrity, stability, and flexibility of shell panels under different conditions. The third-order shear deformation theory (TSDT) is utilized to capture the significant shear deformation effects, which are particularly important in thin shell structures. Additionally, the p-version finite element method is employed for its superior convergence properties and its ability to handle complex geometries more efficiently than traditional finite element methods.

The primary goal of this work is to provide a deeper understanding of how bi-FGM shell panels behave under these different loading conditions and to propose optimization strategies for their design. By analyzing the effects of material gradation, geometric parameters, and loading conditions on the structural response, valuable insights are gained

into how these materials can be tailored for improved performance in practical engineering applications.
Ultimately, this research seeks to deepen the understanding of bi-FGM shell structures and provide a framework for their effective design and optimization. By focusing on the critical analyses of free vibration, thermal buckling, and static bending, this work lays the groundwork for the development of advanced materials and structural systems that are both efficient and robust, tailored for the demanding requirements of modern engineering applications.

0.1 Aim and Focus of the Current thesis

The aim of this research is to create a comprehensive mathematical framework for analyzing bi-directional functionally graded doubly-curved shallow shell panels. This involves integrating the third order shear deformation theory with the p-version finite element method to account for temperature effects throughout the thickness and calculate linear structural responses. The study also assesses the effective material properties of the bi-directional functionally graded material using micromechanical model with a power-law distribution, where the volume fractions of each constituent vary with position and temperature. Additionally,linear response is determined numerically using the isoparametric finite element method. The specific objectives of the research are detailed below:

- The study investigates the free vibration, thermal buckling, and flexural behavior of functionally graded (FGM) shell panels with various geometries, including spherical, cylindrical, hyperbolic, and elliptical shapes. The panels are subjected to uniformly or sinusoidally distributed transverse loads. The analysis is conducted using a third-order shear deformation theory (TSDT) combined with the p-version finite element method.

- Incorporate the influence of porosity into bi-directional functionally graded materials composed of a mixture of three constituents.

- Providing a solution to the non-linear temperature distribution across the shell panel for bi-directional functionally graded materials (bi-FGM) based on the steady-state heat conduction equation for thermal buckling analysis.

0.2 Outline of the Thesis

in Chapter 1;A comprehensive literature review will be conducted, summarizing the research that has been done to date on bi-directional functionally graded materials (bi-FGMs). This chapter will highlight key findings, methodologies, and gaps in the existing literature.Chapter 2 will present the mathematical formulation of the problem, establishing the foundational equations and principles necessary for subsequent analysis. Detailed derivations and assumptions will be discussed to ensure clarity and completeness.The third Chapter 3 will investigate the static bending behavior of bi-FGMs under mechanical loading. Various loading conditions and configurations will be examined to understand the material's response and performance. In Chapter 4, the free vibration characteristics of sandwich shell panels with different geometries will be explored. The analysis will consider various parameters to assess their impact on the vibrational behavior of the structures. The thermal buckling behavior of a single-layer shell panel will be investigated in Chapter 5. Different thermal loading scenarios will be analyzed to determine critical buckling temperatures and modes. The final Chapter will synthesize the findings from the previous chapters, drawing general conclusions from the investigation. Recommendations for future research and potential applications of bi-FGMs will also be discussed.

Chapter 1

Literature Review

1.1 Introduction

Bi-directional functionally graded materials (bi-FGMs) have garnered significant attention in recent years due to their unique combination of properties and potential applications in various engineering fields. These materials exhibit spatial variations in composition and microstructure along two orthogonal directions, offering tailored mechanical, thermal, and electrical properties that cannot be achieved with conventional homogeneous materials. The development of bi-directional bi-FGMs represents a promising avenue for enhancing the performance and reliability of structural components in aerospace, automotive, biomedical, and other industries.

1.2 Significance of Bi-directional FGMs

The unique properties of bi-directional functionally graded materials (FGMs) render them highly appealing for a diverse array of engineering applications. These materials have been extensively explored for their potential utility in structural components, thermal management systems, biomedical implants, electronic devices, and various other advanced technologies. Through careful optimization of the spatial distribution of material properties, bi-directional FGMs have the capacity to enhance the efficiency, durability, and functionality of engineering systems, thereby contributing to improved performance and reduced environmental impact.

The Laser-Engineered Net Shaping (LENS) technique, a type of additive manufacturing, holds significant promise for fabricating bi-directional FGMs. This method operates by depositing powders layer by layer and selectively melting them with lasers, allowing for gradual composition changes in the material.For a comprehensive overview of these manufacturing techniques and their applications, reference [4] is recommended.

1.3 Free vibration and Static bending

To address the limitations of traditional composite materials, a novel type called functionally graded materials (FGMs) was introduced in the mid-80s by a Japanese laboratory, leading to a surge in research on this topic. FGMs offer a smooth transition in material properties by blending two or more ingredients according to a specified law, resulting in uni-directional or bi-/three-directional variations. However, much of the existing literature tends to focus on binary material combinations, neglecting the exploration of porosity distribution in more complex mixtures. Yet, considering multiple materials in FGMs becomes crucial for applications requiring finely tuned properties. While promising enhanced performance, this approach adds complexity to design, processing, and analysis.

Various studies have investigated the dynamic and free vibration characteristics of bi-directional functionally graded materials (FGMs) in various structural configurations. For instance, Ammar et al. [5] explored the behavior of porous plates supported on elastic foundations using the Differential Quadrature Method (DQM). Similarly, Kumar et al. [6] employed the Radial Basis Collocation Method (RBCM) to analyze the free vibration response of elastically supported porous bi-directional functionally graded (bi-FGM) plates. Saini et al. [7] investigated axisymmetric vibrations of non-uniform bi-directional functionally graded rings under two-dimensional temperature distribution, utilizing the FSDT with the DQM. Hashemi et al. [8] focused on the nonlinear free vibration analysis of rectangular plates with porosities, made from bi-directional functionally graded material and resting on elastic foundations. Their study derived equations of motion using Hamilton's principle and von Karman nonlinear strain-displacement relations based on classical plate theory. Bathini et al. [9] proposed a refined FSDT theory to study the free vibration behavior of bi-directional functionally graded porous plates, satisfying transverse shear stress-free conditions and eliminating the need for a shear correction factor. Alipour et al. [10] developed a semi-analytical approach to investigate the free vibration characteristics of variable thickness bi-directional functionally graded material (FGM) plates resting on an elastic foundation.Guojun Nie et al. [11] applied a semi-analytical numerical technique known as the space-based differential quadrature method to conduct dynamic analysis of multi-directional FGM annular plates. Likewise, Kermani et al. [12]

examined the free vibration behavior of multi-directional functionally graded circular annular plates. Shariyat and Alipour [13] formulated a power series solution for analyzing the free vibration and damping characteristics of viscoelastic FGM plates with variable thickness on elastic foundations. Mahinzare et al. [14] investigated the impact of thermal loads on the vibrational behavior of spinning bi-directional FGM microplates. Lieu et al. [15] presented an isogeometric model to study the bending and free vibration analysis of bi-directional FGM plates with variable thickness. Shojaeefard et al. [16] combined the FSDT with the DQM to analyze the free vibration of rotating variable thickness bi-directional FGM circular microplates. Chih-Ping Wu et al. [17] proposed a finite annular prism method to explore the three-dimensional free vibration analysis of bi-directional FGM annular plates under various combinations of boundary conditions based on the Reissner mixed variational theorem. Thai et al. [18] employed a three-dimensional isogeometric model to investigate the bending and free vibration analysis of multi-directional FGM plates under the influence of temperature. Wang et al. [19] conducted an optimization study to determine the optimal shape and material properties of bi-directional FGM plates. Dehshahri [20] analyzed the free vibration characteristics of three-dimensional functionally graded material nanoplates considering the small-scale effect. Ahlawat and Ral [21] investigated a bi-directional circular plate with varying thickness resting on an elastic foundation and subjected to uniform in-plane peripheral loading. Esmaeilzadeh et al. [22] examined the dynamic analysis of stiffened bi-directional FGM plates with porosities under a moving load using the dynamic relaxation method with kinetic damping. Furthermore, a circular bi-directional FGM plate under in-plane distributed load based on Kirshoff theory was analyzed using the GDQM as described by the authors in reference [23].

Numerous studies have been dedicated to examining the behavior of beam elements. For instance, Sharma et al. [24] explored the impact of temperature on the vibrational characteristics of bi-FGM beams. Similarly, Ye Tang et al. [25] introduced a novel model based on the GDQM to analyze the vibration of similar beam geometries. Abbas Barati et al. [26] investigated the vibrational properties of bi-nanobeams under magnetic fields with the aim of controlling their mode shapes. Zhao et al. [27] employed a symplectic approach to conduct a vibration analysis of bi-FGM beams subject to arbitrary boundary conditions. Free and forced vibrations of bi-FGM Timoshenko beams under diverse boundary condition configurations were demonstrated by Mesutid [28]. Lezgy [29] employed an isogeometric finite element model to perform a coupled thermo-mechanical analysis of bi-FGM beams. Tang and Ding [30] investigated the nonlinear vibrational behavior of bi-FGM beams under hygro-thermal loads. Truong et al. [31] presented an isogeometric optimization study focusing on bi-FGM beams under static loading conditions. Li Thi Ha [32] examined the free vibration behavior of a bi-FGM graded porous sandwich beam using a high-order shear deformation theory and the FEM. Ahmadi et al. [33] investigated the free vibration behavior of thick curved nanobeams with concentrated mass under various boundary conditions. Their investigation involved formulating governing equations using Hamilton's principle and the FSDT, while also considering the small-scale effect through nonlocal elasticity theory. Meanwhile, Viet et al. [34] proposed models to analyze the free vibration of FGM sectioned beams using the FEM, taking into account the influence of material properties and dimensions of FGM sections on the beam's natural frequencies and mode shapes. Furthermore, Ohab-Yazdi et al. [35] conducted a free vibration analysis of imperfect bi-FGM nanobeams subjected to rotational velocity. Nejad and Hadi [36] utilized GDQM to explore the free vibration behavior of Euler–Bernoulli bi-FGM nanobeams. Zhao et al. [37] proposed a symplectic framework for analyzing bi-FGM plane problems. Additionally, a combination of shear deformation theory and GDQM was employed to conduct free vibration analysis of curved beams as discussed by Fariborz et al. [38]. Yang et al. [39] investigated the nonlinear bending, buckling, and vibration of bi-FGM nanobeams. Moreover, Pydah [40] presents shear deformation theory using a logarithmic function for thick circular beams and provides analytical solutions for bi-FGM circular beams.

Shell elements represent a category of finite elements used in structural analysis to simulate the behavior of thin-walled structures such as pressure vessels, tanks, and aerospace components. Despite their widespread application in engineering and manufacturing, there is a noticeable scarcity of literature dedicated to shell elements compared to plate and beam elements. This disparity can be attributed to the inherent complexity and computational challenges associated with shell elements. Their analysis necessitates a more intricate mathematical model and demands a higher degree of numerical precision. Furthermore, understanding the response of shell elements under diverse loading conditions is more intricate and poses greater challenges compared to plate and beam elements, thereby discouraging researchers from delving into their study. To illustrate, Ramteke et al. [41] investigated the vibrational characteristics of a multi-directional functionally graded structure featuring varying porosity distribution and grading patterns using FEM. Similarly, Nguyen-Ngoc et al. [42] introduced an innovative three-dimensional polyhedral finite element approach tailored for the analysis of multi-directional functionally graded solid shells. Additionally, Nguyen et al. [43] explored the free vibration of rotating functionally graded sandwich cylindrical shells with a metal-foam core and two coating FGM layers, employing the FSDT and Rayleigh-Ritz method to analyze the vibration behavior of these complex structures. Naveen Kumar et al. [44] investigated the nonlinear vibration behavior of a bi-FGM doubly curved shell panel with porosities based on the FSDT.

1.4 Thermal Buckling

Buckling behavior of bi-directional functionally graded materials FGM has been investigated in several studies. For the sake of completeness, in the following paragraphs, a review of the bibliography regarding buckling behavior in the context of FGM will be presented.To illustrate, Pham Van Vinh et al. [45] employed an improved First-Order Shear Deformation Theory (FSDT) and the Finite Element Method to examine the static bending and buckling behavior of bi-directional functionally graded plates with porosity (BFGP). Similarly, Hai Qing et al. [46] used the Modified Couple Stress Theory (MCST) to evaluate the bending, buckling, and vibration behavior of functionally graded circular/annular microplates.Alessandro Fiorini et al. [47] discussed the buckling behavior of bi-directional FGM thin circular plates in axial and transverse directions. The author used a direct approach to determine the critical load multiplier and buckling mode based on the plate's geometry and constitutive properties. An isogeometric model has been presented by Shuangpeng Li et al. [48] for the investigation of static bending, free vibration, and buckling analysis of porous bi-directional functionally graded plates using the First-Order Shear Deformation Theory (FSDT). Qui X. Lieu et al. [49] introduced a Non-Uniform Rational B-Spline (NURBS) based material mesh to represent the material distribution in combination with the Generalized Shear Deformation Theory to investigate the free vibration and buckling problems of in-plane bi-directional functionally graded plates. A numerical analysis of buckling and bending behavior of bi-directional FG plates using a finite element model and a novel Third-Order Shear Deformation Theory (TSDT) has been reported by Thom Van Do et al. [50]. Minh-Chien Trinh et al. [51] derived a closed-form solution for buckling loads and used Monte Carlo simulation to conduct a comprehensive stochastic quantification of plate behavior. Mohammed Arefi et al. [52] studied the mechanical stability of functionally graded rectangular plates bonded with functionally graded piezoelectric layers, using a classical plate theory to derive the equation of motion. Moreover, a new modified power-law formulation to analyze the critical buckling of functionally graded sandwich plates under axial and biaxial loads, considering both even and uneven porosity distribution, has been conducted by Abdelhak Zohra et al. [53]. An investigation of the impact of porosity distribution on the static and buckling response of a functionally graded porous plate, using an Inverse Hyperbolic Shear Deformation Theory (IHSDT), has been carried out by Mohit Dhuria et al. [54]. Five schemes of porosity distribution have been taken into consideration, and the Navier solution has

been used to obtain the exact solution. Likewise, a combination of DQM with FEM has been used to investigate the buckling behavior of functionally graded porous rectangular plates under different loading conditions, considering three porosity distributions throughout the thickness [55]. Da Chen et al. [56] proposed a novel functionally graded porous plate made of closed-cell aluminum foams with varying material properties across the thickness to avoid interfacial failure in sandwich structures. The Chybyshev-Ritz method has been used for the analysis of its buckling and bending behavior. A similar approach has been followed by Jie Yang et al. [57] for the investigation of the buckling and free vibration behavior of functionally graded reinforced porous nanocomposite plates.
Numerous studies and research articles have explored the behavior of beam geometry.In the subsequent paraphraphs, we will highlight some of the articles pertaining to this specific geometric aspect.for instance;DQM in conjunction with iteration technique the linear and non-linear buckling response of bi-directional FGM nanotubes with the inclusion of porosity effect has been conducted by Pin-Fa Wang et al [58].Likewise Rong Hai Zhang et al [59] investigated the free vibrtion,buckling,and post-buckling behaviour of bi-directional functionally graded microbeams using a mixture between Timoshenko Beam theory and consistent couple stress theory with the DQM.moroever the Ritz method and Reddy beam theory has been used for the investigation of static stability and dynamic characteristic of bi-directional functionally graded beams under various variable axial loads by Somi Naidu et al [60].Chu-Feng Gao et al [61] presented a high-order cylindrical beam model that considers shear deformation to analyze the buckling behaviours of bi-FGM cylindrical beams.Likewise, Yan-Ming Ren et al [62] followed a theoretical approach based on stress-Driven nonlocal integral model for the static bending and elastic buckling of Euler-Brenoulli beams made of FGM.Talal Salem et al [63] investigated the postbuckling behaviour of multi-directional anisotropic FGM beam subjected to billateral constraint using a theoretical model.Likewise,Mohamed Attia et al [64] investigated the non-linear vibration characteristics of pre- and post-buckled nonuniform bi-directional functionally graded microbeams subjected to nonlinear thermal loading.Using a non-local refined simple shear deformation theory; Doan Trac Luat et al [65] investigated the bending, free vibration,and buckling analysis of a novel bi-FGM sandwich nano-beam.A integration between multi-objective particle swarm optimization algorithm and semi analytical solution has been used by Abo-bakr R et al [66] to conduct a vibration and buckling anlysis of bi-FGM beams.
Jian Lei et al [67] investigated the postbuckling response of porous bi-FGM beams considering the transverse shear deformation based on a novel third-order shear deformation theory using a DQM method.
for shell geometry,Farshid Allahkarami et al. [68] conducted a buckling analysis of bi-

directional FGM for porous conical shell under axial compression loading using FSDT and DQM.The same author [69] conducted a similar analysis for porous cylindrical shell embeded in elastic foundation using a combination of TSDT with DQM.Taghizadeh et al [70] analyzed the buckling behavior of bi-directional functionally graded conical micro-shells under axial loading, using MCST in conjuction with Ritz method.Vu Hoai Nam et al. [71] investigated the buckling and postbuckling behavior of stiffened porous cylindrical shell under thermal environment using closed form solution.Van Doan Cao et al. [72] presented the buckling and postbuckling of a newly designed stiffened functionally graded graphene-reinforced composite laminated toroidal shell segment with piezoelectric layer.likewise the buckling behavior of FG carbon nanotube reinforced composite cylindrical shell panels with cutout has been investigated using HSDT by [73].Hajlauoi et al. [74] proposed a modified solid-shell element based on FSDT formulation to analyze the thermal buckling behavior of FG shell structures.Abuteir et al. [75] conducted a dynamic buckling analysis of FGM shell structures in thermal environments with tempearture dependent materials.

Mohamed Saad et al. [76] analyzed the thermal buckling of porous, thick rectangular FGM plates using a combination of Higher-Order Shear Deformation Theory (HSDT) and Navier's solution. Shirayat et al. [77] investigated the dynamic thermal buckling behavior of imperfect FGM cylindrical shells subjected to combined thermal and mechanical loads. Ghiasian et al. [77] examined the bifurcation behavior of moderately thick FGM annular plates under uniform temperature rise and heat conduction loading, incorporating temperature-dependent properties and First-Order Shear Deformation Theory (FSDT). Their study derived stability equations, revealing that critical buckling temperatures and buckled configurations can exhibit asymmetry. Hadi Babaei et al. [78] conducted a thermal buckling and post-buckling analysis of geometrically imperfect FGM clamped tubes resting on a nonlinear elastic foundation. This work employed a closed-form methodology, considering various thermal loading scenarios and temperature-dependent material properties, with the formulation based on a higher-order theory. Nguyen Dinh Duc et al. [79] analyzed the thermal buckling of FGM sandwich truncated conical shells reinforced with FGM stiffeners and supported by Pasternak elastic foundations using FSDT. The Galerkin method was applied to derive a closed-form solution. Y. Kiani et al. [80] investigated the thermal buckling and post-buckling response of imperfect, temperature-dependent sandwich FGM plates on an elastic foundation, employing FSDT and deriving a closed-form solution through a single-mode approach combined with the Galerkin technique. Bagheri et al. [81] studied the asymmetric thermal buckling and post-buckling behavior of temperature-dependent annular FGM plates resting on a partial elastic foundation, utilizing FSDT and von Kármán-type geometric nonlinearity. Finally, J. Torabi

et al. [82] performed a linear thermal buckling analysis of truncated hybrid FGM conical shell panels using classical shell theory and Sanders' nonlinear kinematic relations.
From the aforementioned literature review, it is evident that most of the earlier work focused on buckling under mechanical loads with FGM in one direction.Surpringly, there has been relatively little attention given to the complexity of shell geometry, even though it represents the most realistic and common structure found in real-world applications. Moreover, only a limited number of studies have explored the bi-directional aspect of Functionally Graded Materials (FGM), and the majority of existing works on the p-version Finite Element Method predominantly focus on vibration behavior. Consequently, this article pioneers a thermal buckling analysis of bi-directional FGM shells with diverse geometries. The novelty of this study lies in its use of the p-version Finite Element Method with the Third Order Shear Deformation Theory (TSDT), offering a first-of-its-kind exploration. One notable advantage of the p-version Finite Element Method is its capacity to provide higher accuracy when compared to the traditional h-version FEM . Allowing the order of approximation polynomials (p) to vary within an element, the p-version method reduces computational costs in specific scenarios. Furthermore, it demonstrates lower sensitivity to mesh distortion compared to the h-version. This attribute proves advantageous, especially when dealing with irregular or distorted meshes, as the method still yields accurate solutions without requiring excessive mesh refinement. Another strength lies in its high convergence rate for singular or nearly singular solutions. Additionally, its compatibility with isogeometric analysis makes it more suitable for capturing complex geometries. The primary objective of this study is to conduct a comprehensive investigation into the influence of various parameters, including aspect ratio, thickness ratio, and material gradation indexes, on the critical buckling load. Three distinct temperature distributions will be considered: uniform, linear, and non-linear, with the option of either temperature-dependent (TD) or temperature-independent (TID) materials.

1.5 Observations

The review above highlights a significant gap in the research regarding the flexural and thermal buckling, as well as the vibrational responses of functionally graded (FG) single and doubly-curved shell panels subjected to thermal fields. Drawing from the existing literature and subsequent discussions, the following points elucidate the knowledge gaps in previous contributions:

- **Limited Focus on Curvature:**The analysis predominantly emphasizes flat and singly-curved FG shell panels, with very few studies exploring the complexities associated with doubly-curved shell panels. This limitation restricts our understanding of how geometric intricacies influence buckling and vibration behaviors under thermal conditions.

- **Material Orientation Constraints:**Most of the research conducted has primarily focused on uni-directional functionally graded materials. This narrow approach may overlook the potential benefits of multi-directional material gradation, which could enhance the performance and durability of shell structures.

- **Formulation Techniques:**The formulations utilized in these analyses often rely on the First-Order Shear Deformation Theory (FSDT) or the Classical Shell Theory (CST). Notably, this study aims to pioneer the application of the Third-Order Shear Deformation Theory (TSDT) within the context of the p-version Finite Element Method (FEM), marking a significant advancement in modeling techniques.

Addressing these knowledge gaps could pave the way for more comprehensive analyses and enhance the design and performance of FG shell panels in various engineering applications.

1.6 Summary

This chapter presented a comprehensive literature review focusing on the free vibration, static bending, and thermal buckling of bi-directional functionally graded materials (bi-FGMs). The significance of bi-FGMs was discussed, emphasizing their unique properties and potential applications across various engineering fields, particularly in enhancing the performance and reliability of structural components.
The review synthesized existing research and identified critical gaps in the literature concerning the flexural and thermal responses of functionally graded shell panels subjected to thermal fields. This included a limited exploration of doubly-curved geometries, a predominant focus on uni-directional materials, and a reliance on traditional formulation techniques. These gaps underscored the need for more comprehensive analyses and innovative modeling approaches.

Chapter 2

General Mathematical Formulation

2.1 Introduction

Generally, structural components encounter various loads and environmental conditions throughout their service life. As time passes, the actual performance of these components gradually deteriorates, leading to structural failure. Therefore, understanding structural responses such as frequency, deformation, and critical load is crucial for ensuring structural sustainability under harsh environmental conditions. There are two main methods for determining structural responses: laboratory experimentation and numerical simulation. This study specifically focuses on numerically analyzing structures made of bi-direciontla functionally graded materials (bi-FGMs), which exhibit microscopic heterogeneity. While closed-form solutions are feasible for simple geometries and material models, complex problems require numerical techniques like the finite element method (FEM) for accurate solutions. Incorporating higher-order shear deformation terms ensures the accuracy of structural responses. Finite element methods offer several advantages over closed-form solutions. Firstly, they provide flexibility by accommodating complex geometries and boundary conditions more effectively. This versatility makes FEM suitable for a wide array of engineering problems, ranging from simple structures to highly nonlinear systems. Additionally, FEM can be scaled to address problems of varying complexity, allowing for adjustments in mesh density and refinement to enhance analysis accuracy. Moreover, FEM generally yield more accurate results for complex problems compared to closed-form solutions. This is particularly true in scenarios where simplifications are required in closed-form solutions, leading to potential errors. Furthermore, finite element methods are versatile in their ability to model various physical phenomena, including structural mechanics, heat transfer, fluid dynamics, and electromagnetics, enabling comprehensive analysis of multi-physics problems. Another advantage is the ease with which

finite element methods handle complex boundary conditions, such as mixed boundary conditions, constraints, and contact interactions. These features are challenging to incorporate into closed-form solutions, highlighting the superiority of finite element methods in practical applications. Additionally,FEM can adaptively refine the mesh in regions of interest, balancing accuracy and computational cost efficiently. Moreover, finite element methods can be seamlessly integrated with Computer-Aided Design (CAD) software, facilitating streamlined design and analysis workflows. This integration enables rapid prototyping, optimization, and visualization of analysis results in 3D. Overall, the advantages of finite element methods make them indispensable tools for engineers and researchers in various fields of study.
This chapter presents a comprehensive mathematical formulation for the functionally graded (FGM) doubly curved shell panel within the framework of Higher-order Shear Deformation Theory (HSDT) kinematics. The formulation is developed based on a combination of general and specific assumptions and includes the evaluation of effective material properties using Voigt's micromechanical model with power-law distribution, where the gradation is assumed to occur in both thickness and x-direction. Additionally, a versatile model for a doubly-curved shallow shell panel is established and can be adapted to accommodate various shell configurations by adjusting curvature values.

2.2 Assumptions

The following assumptions are made in the current mathematical formulation:

1) The main geometric assumption is a doubly curved shell panel with a rectangular planform.A doubly curved shell means that the shell surface is curved in two orthogonal directions, giving it a more complex geometry compared to single curvature (like a cylindrical shell). This kind of geometry is common in structures designed for strength and rigidity, as doubly curved surfaces can distribute loads more efficiently.A rectangular planform describes the flat projection of the shell's shape onto a horizontal plane, meaning that the boundary of the shell, when viewed from above, forms a rectangle.In essence, the assumption implies a shell structure with curvature in two directions, designed with a rectangular boundary when viewed in a top-down projection.

2) In order to model a three-dimensional shell panel, a corresponding two-dimensional single-layer theory is employed. This approach simplifies the complex three-dimensional

structure into a two-dimensional framework by focusing on a single representative layer. Such a model captures the essential mechanical behavior of the shell, including its deformation and stress distribution, while reducing computational complexity. This method is particularly useful in analyzing shell structures efficiently without compromising the accuracy of the overall structural response.

3) The fundamental configuration of the model is designed as a doubly curved shell panel, which provides a versatile framework for various applications in structural analysis. However, the flexibility of the custom-made code enables adjustments to the curvature parameters. By modifying these curvature values, one can easily simulate and analyze different geometric configurations, including flat panels, spherical panels, cylindrical panels, hyperbolic panels, and elliptical panels.

4) In this analysis, the reference plane is defined as the mid-plane of the shell panel. This mid-plane serves as a critical point of reference for understanding the structural behavior and mechanical response of the shell. It is positioned equidistantly between the upper and lower surfaces of the shell, providing a balanced framework for evaluating various stresses, strains, and deformation patterns.

5) The formulation employed in this analysis assumes a plane stress condition, which is a fundamental simplification in the study of shell structures. Under this assumption, we neglect the transverse normal stress, thereby focusing exclusively on the in-plane stresses acting within the shell panel. This approach is particularly applicable to thin shells, where the thickness is significantly smaller than the other dimensions, allowing for the dominant influence of in-plane forces while minimizing the effects of out-of-plane stresses.

6) A bi-directional gradation of Functionally Graded Material (FGM) constituent is assumed, occurring in both the thickness and x-direction of the shell panel.

7) The effect of porosity is assumed to vary solely in the thickness direction, reflecting the layer-by-layer manufacturing technique typically used for such materials. In this context, porosity is regarded as a manufacturing defect occurring when residuals block the nozzle projecting the material. However, it is assumed that any changes in porosity are negligible within each layer during the manufacturing process, with alterations only occurring when transitioning from one layer to the next.

2.3 Displacement Field

In this thesis, a higher-order shear deformation theory is employed (HSDT) to express the displacement field for a bi-directional funtionally graded shell,which is represented by the following formula [83]:

$$\begin{cases} u(x,y,z) = u_0(x,y) + z\theta_x(x,y) + z^2\overline{u_0}(x,y) + z^3\overline{\theta_x}(x,y) \\ v(x,y,z) = v_0(x,y) + z\theta_y(x,y) + z^2\overline{v_0}(x,y) + z^3\overline{\theta_y}(x,y) \\ w(x,y,z) = w_0(x,y) \end{cases} \tag{2.1}$$

where the mid-plane displacements along (x, y, z) coordinates are indicated, respectively, by (u_0, v_0, w_0). The higher-order terms specified in the mid-plane of the curved panel are ($\overline{u_0}$,$\overline{v_0}$,$\overline{\theta_x}$,$\overline{\theta_y}$), and the shear rotations around the x- and y-axes are θ_y and θ_x, respectively. a matrix form of the last equation can written in the following form:

$$\{\delta\} = [Sr]\{\delta_0\} \tag{2.2}$$

where, $\{\delta\} = \{u, v, w\}^T$ and $\{\delta_0\} = \{u_0, v_0, w_0, \theta_x, \theta_y, \overline{u_0}, \overline{v_0}, \overline{\theta_x}, \overline{\theta_y}\}$ and :

$$[Sr] = \begin{bmatrix} 1 & 0 & 0 & z & 0 & z^2 & 0 & z^3 & 0 \\ 0 & 1 & 0 & 0 & z & 0 & z^2 & 0 & z^3 \\ 0 & 0 & 1 & 0 & 0 & 0 & 0 & 0 & 0 \end{bmatrix} \tag{2.3}$$

2.3.1 Strain-Displacement Relationship

The strain-displacement relationship is described as follows [84]:

$$\begin{cases} \varepsilon_{xx} = \frac{\partial u}{\partial x} + \frac{w}{R_x} \\ \varepsilon_{yy} = \frac{\partial v}{\partial x} + \frac{w}{R_y} \\ \varepsilon_{xy} = \frac{\partial u}{\partial y} + \frac{\partial v}{\partial x} \\ \varepsilon_{xz} = \frac{\partial u}{\partial z} + \frac{\partial w}{\partial x} - \frac{u}{R_x} \\ \varepsilon_{yz} = \frac{\partial v}{\partial z} + \frac{\partial w}{\partial y} - \frac{v}{R_y} \end{cases} \tag{2.4}$$

the deformation tensor could be rearranged to the following form:

$$\{\varepsilon\} = \begin{Bmatrix} \varepsilon_x^0 \\ \varepsilon_y^0 \\ \varepsilon_{xy}^0 \\ \varepsilon_{xz}^0 \\ \varepsilon_{yz}^0 \end{Bmatrix} + z \begin{Bmatrix} k_x^1 \\ k_y^1 \\ k_{xy}^1 \\ k_{xz}^1 \\ k_{yz}^1 \end{Bmatrix} + z^2 \begin{Bmatrix} k_x^2 \\ k_y^2 \\ k_{xy}^2 \\ k_{xz}^2 \\ k_{yz}^2 \end{Bmatrix} + z^3 \begin{Bmatrix} k_x^3 \\ k_y^3 \\ k_{xy}^3 \\ k_{xz}^3 \\ k_{yz}^3 \end{Bmatrix} = [T_l] \cdot \{\overline{\varepsilon}\} \tag{2.5}$$

where:

$$\{\overline{\varepsilon}\} = \{\varepsilon_x^0\varepsilon_y^0\varepsilon_{xy}^0\varepsilon_{xz}^0\varepsilon_{yz}^0 k_x^1 k_y^1 k_{xy}^1 k_{xz}^1 k_{yz}^1 k_x^2 k_y^2 k_{xy}^2 k_{xz}^2 k_{yz}^2 k_x^3 k_y^3 k_{xy}^3 k_{xz}^3 k_{yz}^3\} \tag{2.6}$$

and $[T_l]$ is (5×20) matrix holding z coefficients.
The linear mid-plane strain vectors are denoted by $\overline{\varepsilon}$. The components of these vectors are listed in Appendix. Specifically, terms marked with superscript 0 represent membrane effects, those with superscript 1 represent curvature effects, and the remaining terms represent higher-order strain effects. The linear thickness coordinate matrices $[T_l]$ are provided, and the detailed components are listed in the Appendix.

2.4 Thermal Buckling

2.4.1 Material Properties of bi-FGM

The properties of functionally graded material are assumed to vary from the bottom surface to the top surface and from left to right (x=0, x=a) according to a power-law distribution. Thus, the variation occurs in both the x and z directions. For temperature-dependent properties, the variation is assumed to follow the form presented by Reddy [2]:

$$P_{c/m}(T) = P0 \times (\frac{P_{-1}}{T} + 1 + P_1 \times T + P_2 \times T^2 + P_3 \times T^3) \tag{2.7}$$

where $P_{-1}, P_1, P_2, P_3, P_0$;are the material properties coefficients for the material,and T represent the temperature.
and the power-law distribution is as follows [15]:

$$P(z, x, T) = (P_c(T) - P_m(T)) \times (\frac{z}{h} + \frac{1}{2})^{n_z} \times (\frac{x}{a})^{n_x} + P_m(T) \tag{2.8}$$

Where:

$$-0.5 < \frac{z}{h} < 0.5 \qquad 0 < \frac{x}{a} < 1 \tag{2.9}$$

2.4.2 Temperature Distributions

To obtain a generic case study, three temperature distributions will be considered: uniform, linear, and non-linear; temperature change will be assumed to be in the thickness direction.

2.4.2.1 Uniform Temperature Distribution

The temperature is expressed as:

$$T = T_0 + \Delta T \tag{2.10}$$

in this case,as it is assumed to be uniform across the thickness regardless of the coordinates,where: ΔT represent the temperature change,and T_0 is the ambient temperature.

2.4.2.2 Linear Temperature Distribution

The temperature field is assumed to vary linearly in the direction of thickness.Let T_b and T_t represent the temperature at the bottom and top surfaces,respectively.The temperature field with a linear gradient along the thickness direction is denoted by [85]:

$$T(z) = T_b + (T_t - T_b)(\frac{z}{h} + \frac{1}{2}) \tag{2.11}$$

2.4.2.3 Non-Linear Temperature Distribution

The temperature field exhibiting non-linear variation in the thickness direction is obtained and defined as follows by applying a two-dimensional heat conduction equation:

$$\frac{d}{dz}(k(z,x)\frac{dT}{dz}) + \frac{d}{dx}(k(z,x)\frac{dT}{dx}) = 0 \tag{2.12}$$

The temperature gradient in the x-direction becomes negligible in comparison to the temperature gradient in the z-direction, assuming that main heat conduction occurs mostly in the z-direction, as is usual in real-world applications. As a result, the above equation may be simplified to the following form:

$$\frac{d}{dz}(k(z,x)\frac{dT}{dz}) = 0 \tag{2.13}$$

$$T(z,x) = T_b + \frac{(T_t - T_b)}{\int_{-h/2}^{h/2} \frac{1}{k(z,x)} dz} \int_{-h/2}^{z} \frac{1}{k(z,x)} dz \tag{2.14}$$

Substituting Equation 2.8 into Equation 2.14:

$$T(z,x) = T_b + \frac{(T_t - T_b)}{\int_{-h/2}^{h/2} \frac{dz}{k_m + \Delta k(\frac{z}{h}+\frac{1}{2})^{n_z}(\frac{x}{a})^{n_x}}} \int_{-h/2}^{z} \frac{dz}{k_m + \Delta k(\frac{z}{h}+\frac{1}{2})^{n_z}(\frac{x}{a})^{n_x}} \tag{2.15}$$

here $\Delta k = k_c - k_m$. In this scenario, it is assumed that the thermal conductivity (k) is independent of temperature.A polynomial series might be used to further resolve previous equation:

$$T(z,x) = T_b + (T_t - T_b) \times \frac{\sum_{q=0}^{5} (-1)^q \left(\frac{\Delta k}{k_m}\right)^q \left(\frac{x}{a}\right)^{qn_x} \left(\frac{z}{h} + \frac{1}{2}\right)^{qn_z+1} \frac{1}{qn_z+1}}{\sum_{q=0}^{5} (-1)^q \left(\frac{\Delta k}{k_m}\right)^q \left(\frac{x}{a}\right)^{qn_x} \frac{1}{qn_z+1}} \tag{2.16}$$

Furthermore, it should be made clear that this solution is a more generalized version than the one suggested by [85]. They made the assumption that the Functionally Graded Material (FGM) is solely graded in the z-direction when they derived the data. On the other hand, the current approach can deal with both bi-directional FGM graded in both the x and z directions, as well as uni-directional FGM, by setting $n_x = 0$.

2.4.3 Shell panel geometry

The current analysis focuses on a uniform thickness doubly curved functionally graded (FGM) panel with a rectangular base, featuring sides of lengths a and b, depicted in Figure 2.1. The principal radii of curvature along the x and y directions are denoted as R_x and R_y, respectively. For different types of panels—flat, cylindrical, spherical, hyperbolic paraboloid, and ellipsoid—the principal radii of curvature can be expressed as follows: R_x and R_y are infinite for flat panels, R_x is R and R_y is infinite for cylindrical panels, R_x and R_y are both R for spherical panels, R_x is R and R_y is -R for hyperbolic paraboloid panels, and R_x is R and R_y is 2R for ellipsoid panels.

2.4.4 Constitutive Equations

The stress field resulting from thermal and elastic effects in the FG shell panel can be expressed as:

$$\{\sigma\} = [C] \cdot (\{\varepsilon\} - \{\varepsilon_{thermal}\}) \tag{2.17}$$

$$\{\sigma\} = \{\sigma_{xx} \quad \sigma_{yy} \quad \tau_{xy} \quad \tau_{xz} \quad \tau_{yz}\} \tag{2.18}$$

$$\begin{Bmatrix} \sigma_{xx} \\ \sigma_{yy} \\ \tau_{xy} \\ \tau_{xz} \\ \tau_{yz} \end{Bmatrix} = \begin{pmatrix} \frac{E(z,x)}{1-\upsilon^2} & \frac{E(z,x)\cdot\upsilon}{1-\upsilon^2} & 0 & 0 & 0 \\ \frac{E(z,x)}{1-\upsilon^2} & \frac{E(z,x)\cdot\upsilon}{1-\upsilon^2} & 0 & 0 & 0 \\ 0 & 0 & \frac{E(z,x)}{2\cdot(1+\upsilon)} & 0 & 0 \\ 0 & 0 & 0 & \frac{E(z,x)}{2\cdot(1+\upsilon)} & 0 \\ 0 & 0 & 0 & 0 & \frac{E(z,x)}{2\cdot(1+\upsilon)} \end{pmatrix} \cdot \left(\begin{Bmatrix} \varepsilon_{xx} \\ \varepsilon_{yy} \\ \varepsilon_{xy} \\ \varepsilon_{xz} \\ \varepsilon_{yz} \end{Bmatrix} - \begin{Bmatrix} \alpha \cdot \Delta T \\ \alpha \cdot \Delta T \\ 0 \\ 0 \\ 0 \end{Bmatrix} \right) \tag{2.19}$$

Where α represent thermal expansion coefficient,while ΔT represents the temperature rise.

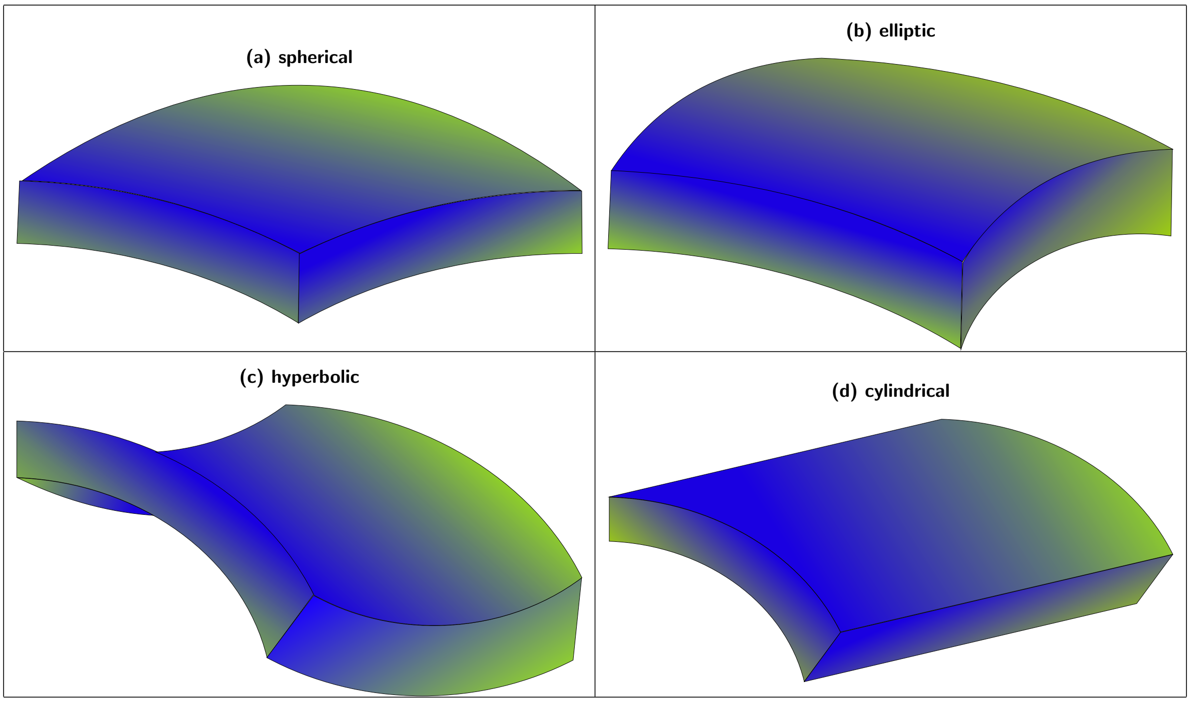

Figure 2.1: Representation of different shell panels geometries

2.4.5 Strain-Energy

The work resulting from in-plane compressive thermal loading in Green-Lagrange sense for a doubly curved shell panel can be defined as follows [86]:

$$U_{thr} = \int_V \{\varepsilon_{nonl}\}^T \cdot \{N_{\Delta T}\}\, dV \tag{2.20}$$

$$\begin{aligned} U_{thr} = \int_V \Bigg(&\frac{1}{2}\{(u_{,x} + w/R_x)^2 + (v_{,x})^2 + (w_{,x} - u/R_x)^2\} N_{\Delta T_x} \\ &+ \frac{1}{2}\{(u_{,y})^2 + (v_{,y} + w/R_y)^2 + (w_{,y} - v/R_y)^2\} N_{\Delta T_y} \\ &+ \{(u_{,x} + w/R_x)(u_{,y}) + (v_{,x})(v_{,y} + w/R_y) + (w_{,x} - u/R_x)(w_{,y} - v/R_y)\} N_{\Delta T_{xy}} \Bigg)\, dV \end{aligned} \tag{2.21}$$

Where $N_{\Delta T}$: represent the in-plane thermal force vector,and ε_{nonl} is the nonlinear Green-Langrange strain tensor

This equation (2.20) can be expressed in matrix form, as initially proposed by Cook [87]:

$$U_{thr} = \frac{1}{2}\int_V \left\{ \begin{array}{c} \frac{\partial u}{\partial x} + \frac{w}{R_x} \\ \frac{\partial u}{\partial y} \\ \frac{\partial v}{\partial x} \\ \frac{\partial v}{\partial y} + \frac{w}{R_y} \\ \frac{\partial w}{\partial x} - \frac{u}{R_x} \\ \frac{\partial w}{\partial y} - \frac{v}{R_y} \end{array} \right\}^T \tag{2.22}$$

$$\times \begin{pmatrix} N_{\Delta Tx} & 2N_{\Delta Txy} & 0 & 0 & 0 & 0 \\ 2N_{\Delta Txy} & N_{\Delta Ty} & 0 & 0 & 0 & 0 \\ 0 & 0 & N_{\Delta Tx} & 2N_{\Delta Txy} & 0 & 0 \\ 0 & 0 & 2N_{\Delta Txy} & N_{\Delta Ty} & 0 & 0 \\ 0 & 0 & 0 & 0 & N_{\Delta Tx} & 2N_{\Delta Txy} \\ 0 & 0 & 0 & 0 & 2N_{\Delta Txy} & N_{\Delta Ty} \end{pmatrix}$$

$$\times \left\{ \begin{array}{c} \frac{\partial u}{\partial x} + \frac{w}{R_x} \\ \frac{\partial u}{\partial y} \\ \frac{\partial v}{\partial x} \\ \frac{\partial v}{\partial y} + \frac{w}{R_y} \\ \frac{\partial w}{\partial x} - \frac{u}{R_x} \\ \frac{\partial w}{\partial y} - \frac{v}{R_y} \end{array} \right\} \cdot dV \tag{2.23}$$

Where: $N_{\Delta Tx} = N_{\Delta Ty} = (C_{11} + C_{12})\alpha\Delta T; N_{\Delta Txy} = 0$

2.4.5.1 p-version Finit element formulation

the displacement vector can be conducted to the new form by employing the FEM concept as:

$$\{\delta\} = [N_i]\{\delta\}_i \qquad \{\bar{\varepsilon}\} = [B_l]\{\delta\} \tag{2.24}$$

Where $[B_l]$ represents the gradient of displacements,and $[N_i]$ is the heirarchical shifted Legendre polynomial shape functions [1].Using equations 2.24 and 2.20;The strain energy would becomes:

$$U = \frac{1}{2}\int_V \{\delta\}^T [B_l]^T [D][B_l]\{\delta\} dV \tag{2.25}$$

where:

$$[D] = [T_l]^T [C][T_l] \tag{2.26}$$

following a similar procedure the thermal strain energy could be rearranged to the following form:

$$U_{thr} = \frac{1}{2}\int_V \{\varepsilon_G\}^T[D_G]\{\varepsilon_G\}dV \tag{2.27}$$

and $\{\varepsilon_G\}$ could be further simplified to the following form:

$$\{\varepsilon_G\} = [H_G][B_G]\{\delta\} \tag{2.28}$$

Where $[H_G]$ is a matrix holding z coefficients (similar to $[T_l]$).
using equations 2.28 and 2.27 we could have:

$$U_{thr} = \frac{1}{2}\int_V \{\delta\}^T[B_G]^T[S_G][B_G]\{\delta\}dV \tag{2.29}$$

where:

$$[S_G] = [H_G]^T[D_G][H_G] \tag{2.30}$$

The governing equation for the buckling of a shell panel under thermal loading can be derived by minimizing the total energy expression:

$$\Pi = U_e - U_{thr} \qquad \frac{\partial \Pi}{\partial \delta_i} = 0 \tag{2.31}$$

$$([K] - \lambda_{cr}\cdot[K_G]) = 0 \tag{2.32}$$

where:

$$[K] = \int_V [B_l]^T[D][B_l]dV \qquad [K_G] = \int_V [B_G]^T[S_G][B_G]dV \tag{2.33}$$

2.5 Static Bending & Free vibration analysis

The Displacement field in this case is kept as it is in this case also.in addition, it is assumed in this case the doubly curved shell panel is sandwich shell panel (2.2), and porosity effect is taken into account, also the effect of temperature on material properties in not taken into account.

The stress field of FG curved shell panel can be expressed as:

$$\{\sigma\} = [C]\cdot\{\varepsilon\} \tag{2.34}$$

$$\{\sigma\} = \{\sigma_{xx} \quad \sigma_{yy} \quad \tau_{xy} \quad \tau_{xz} \quad \tau_{yz}\} \tag{2.35}$$

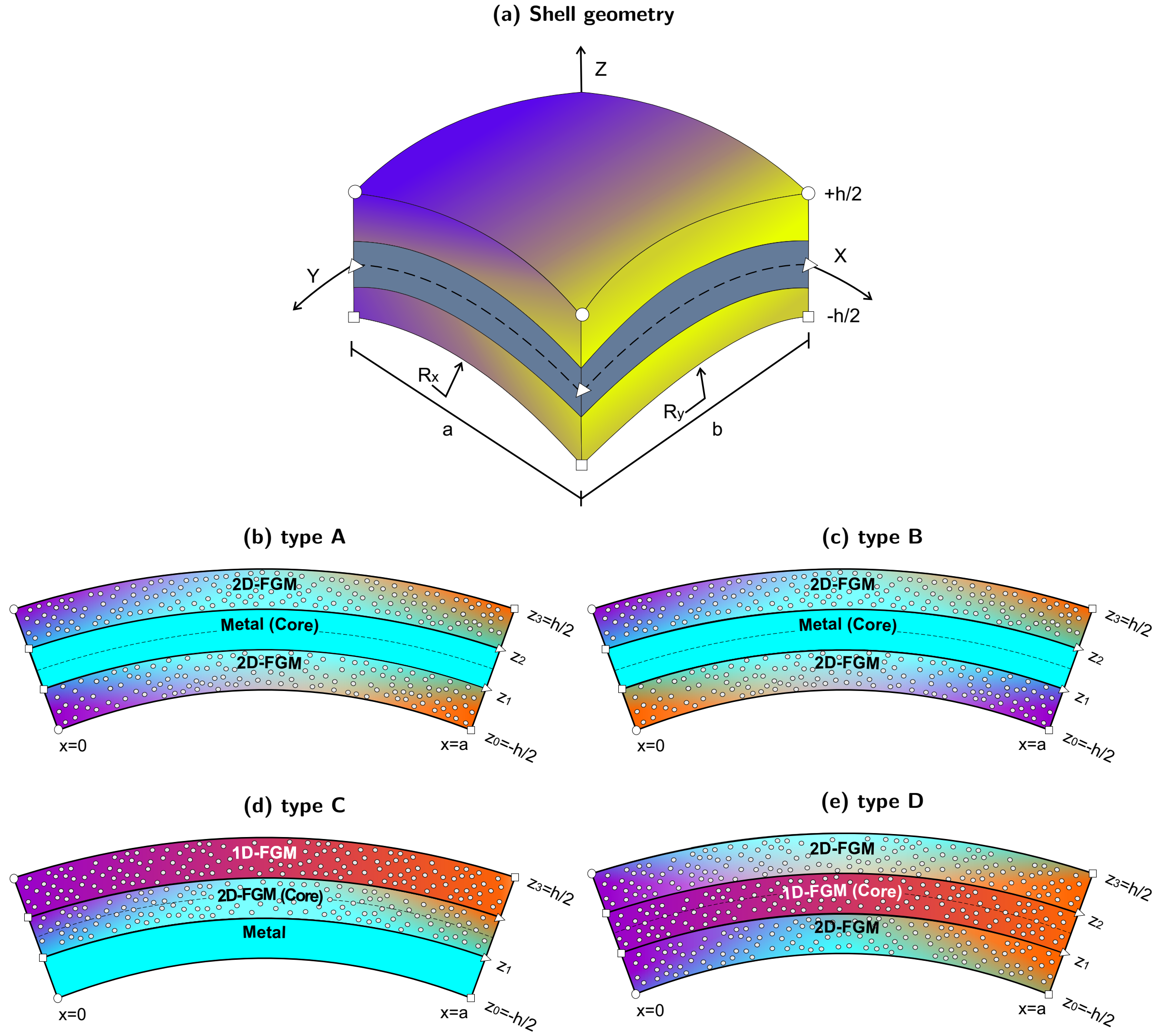

Figure 2.2: Sandwich doubly curved shell panel material distribution for Free vibration and Static Bending analysis case studies

$$\left\{\begin{array}{c}\sigma_{xx}\\ \sigma_{yy}\\ \tau_{xy}\\ \tau_{xz}\\ \tau_{yz}\end{array}\right\}=\begin{pmatrix}\frac{E(z,x)}{1-\upsilon^2} & \frac{E(z,x)\cdot\upsilon}{1-\upsilon^2} & 0 & 0 & 0\\ \frac{E(z,x)}{1-\upsilon^2} & \frac{E(z,x)\cdot\upsilon}{1-\upsilon^2} & 0 & 0 & 0\\ 0 & 0 & \frac{E(z,x)}{2\cdot(1+\upsilon)} & 0 & 0\\ 0 & 0 & 0 & \frac{E(z,x)}{2\cdot(1+\upsilon)} & 0\\ 0 & 0 & 0 & 0 & \frac{E(z,x)}{2\cdot(1+\upsilon)}\end{pmatrix}\cdot\left\{\begin{array}{c}\varepsilon_{xx}\\ \varepsilon_{yy}\\ \varepsilon_{xy}\\ \varepsilon_{xz}\\ \varepsilon_{yz}\end{array}\right\} \tag{2.36}$$

The total strain energy of the FG shell panel can be written as:

$$U_e=\frac{1}{2}\int\{\varepsilon\}^T\cdot[C]\cdot\{\varepsilon\}\cdot\ dV \tag{2.37}$$

In the present analysis, the FG curved shell panel is under the influence of the uniformly distributed mechanical transverse load (q).Therefore,the total external work can be expressed as:

$$W_e=\int\int\{\delta\}\cdot\{q\}\cdot dxdy \tag{2.38}$$

The elemental displacement vector is obtained using the corresponding shape function and represented in the following form:

$$\{\delta\}=\sum_{n=1}^{nn}[N]\cdot\{\overline{\delta}\} \tag{2.39}$$

where nn represent the number of nodes in the elements.and $\overline{\delta}$ represent the nodal displacement vector.

$$\{\overline{\delta}\}=\{u_{0i}\quad v_{0i}\quad w_{0i}\quad \theta_{xi}\quad \theta_{yi}\quad \overline{u}_{0i}\quad \overline{v}_{0i}\quad \overline{\theta}_{xi}\quad \overline{\theta}_{yi}\} \tag{2.40}$$

Again, the strain tensor can expressed in terms of nodal displacement vector as:

$$\{\overline{\varepsilon}\}=[B]\cdot\{\overline{\delta}\} \tag{2.41}$$

Where [B] represent the product form of the differential operator matrix and the shape functions.

Now the elemental equation of the total strain energy can be expressed as:

$$U^e=\frac{1}{2}\int(\{\overline{\delta}\}^T\cdot[K^e]\cdot\{\overline{\delta}\}) \tag{2.42}$$

similarly, the elemental equation of work done due to distributed load can be presented in the following form:

$$W^e = \{\delta\}^e \cdot \{F_m\} \tag{2.43}$$

where:

$$\{F_m\}^e = \int_0^1 \int_0^1 [N] \cdot \{q\}|J|d\xi d\eta \tag{2.44}$$

The governing equation of FG curved shell panel for bending behavior is derived using variational principle and can be written as:

$$\delta\Pi = \delta U_e - \delta W_e = 0 \tag{2.45}$$

where $\delta\Pi$ represent the variation of the total energy.
The kinetic energy for the shell is expressed as follows:

$$T = \frac{1}{2}\int_V \{\delta\}^T [T_l]^T \rho [T_l]\{\delta\} dV \tag{2.46}$$

The final form of governing equation for the linear free vibrated shell panel is obtained by using the Hamilton's principle.This results in:

$$\delta \int_{t1}^{t2} L dt = 0 \tag{2.47}$$

Where : $L = (T - U)$
A comperhensive derivation procedure has been published in panda's article [84].
so the final form of the equations is as follows:

$$\text{Static Bending:}[K_e] \cdot \{\delta_e\} = \{F_m\}^e \tag{2.48}$$

$$\text{Free Vibration:}([K_e] - \omega^2 \cdot [M]) \cdot \{\delta_e\} = 0 \tag{2.49}$$

$$\text{Thermal Buckling:}([K_e] - \lambda_{cr} \cdot [K_G]) \cdot \{\delta_e\} = 0 \tag{2.50}$$

2.5.1 Porosity Distribution in the Shell panel

In the case of free vibration and static bending, the mixture is assumed to consist of three materials—two ceramics and one metallic. Accordingly, the mechanical properties are defined as follows:

$$P = P_{c1} \times\ V_{c1} + P_{c2} \times\ V_{c2} + P_m \times\ V_m - \kappa \tag{2.51}$$

In the previous equation, P represents the mechanical property, V denotes the volume fraction, and κ accounts for the contribution of porosity.

Four sandwich mixtures, labeled A/B/C/D, were originally proposed by Vinh [88]. The functionally graded sandwich shell consists of three layers: a core layer and two face sheets. The thicknesses of the bottom, core, and top layers are represented by $h_1 - h_2 - h_3$, respectively. The top and bottom coordinates of each layer, relative to the neutral plane (indicated by a dashed line in Figure 2.2), are denoted by z.

typeA

$$\begin{cases} V_{c1} = V(x) \times (\frac{z-z_1}{z_0-z_1})^{n_z}, V_{c2} = (1-V(x)) \times (\frac{z-z_1}{z_0-z_1})^{n_z}, V_m = 1-(\frac{z-z_1}{z_0-z_1})^{n_z} & z_0 \leq z \leq z_1 \\ V_{c1} = 0, V_{c2} = 0, V_m = 1 & z_1 \leq z \leq z_2 \\ V_{c1} = V(x) \times (\frac{z-z_2}{z_3-z_2})^{n_z}, V_{c2} = (1-V(x)) \times (\frac{z-z_2}{z_3-z_2})^{n_z}, V_m = 1-(\frac{z-z_2}{z_3-z_2})^{n_z} & z_2 \leq z \leq z_3 \end{cases} \tag{2.52}$$

typeB

$$\begin{cases} V_{c2} = V(x) \times (\frac{z-z_1}{z_0-z_1})^{n_z}, V_{c1} = (1-V(x)) \times (\frac{z-z_1}{z_0-z_1})^{n_z}, V_m = 1-(\frac{z-z_1}{z_0-z_1})^{n_z} & z_0 \leq z \leq z_1 \\ V_{c1} = 0, V_{c2} = 0, V_m = 1 & z_1 \leq z \leq z_2 \\ V_{c1} = V(x) \times (\frac{z-z_2}{z_3-z_2})^{n_z}, V_{c2} = (1-V(x)) \times (\frac{z-z_2}{z_3-z_2})^{n_z}, V_m = 1-(\frac{z-z_2}{z_3-z_2})^{n_z} & z_2 \leq z \leq z_3 \end{cases} \tag{2.53}$$

typeC

$$\begin{cases} V_{c1} = 0, V_{c2} = 0, V_m = 1 & z_0 \leq z \leq z_1 \\ V_{c1} = V(x) \times (\frac{z-z_1}{z_2-z_1})^{n_z}, V_{c2} = (1-V(x)) \times (\frac{z-z_1}{z_2-z_1})^{n_z}, V_m = 1-(\frac{z-z_1}{z_2-z_1})^{n_z} & z_1 \leq z \leq z_2 \\ V_{c1} = V(x), V_{c2} = (1-V(x)), V_m = 0 & z_2 \leq z \leq z_3 \end{cases} \tag{2.54}$$

TypeD

$$\begin{cases} V_{c1} = V(x) \times (\frac{z-z_0}{z_1-z_0})^{n_z}, V_{c2} = (1-V(x)) \times (\frac{z-z_0}{z_1-z_0})^{n_z}, V_m = 1-(\frac{z-z_0}{z_1-z_0})^{n_z} & z_0 \leq z \leq z_1 \\ V_{c1} = V(x), V_{c2} = 1-V(x), V_m = 0 & z_1 \leq z \leq z_2 \\ V_{c1} = V(x) \times (\frac{z-z_3}{z_2-z_3})^{n_z}, V_{c2} = (1-V(x)) \times (\frac{z-z_3}{z_2-z_3})^{n_z}, V_m = 1-(\frac{z-z_3}{z_2-z_3})^{n_z} & z_2 \leq z \leq z_3 \end{cases} \tag{2.55}$$

four types of porosity distribution has been introduced to analyse the shell behaviour: for type A and B

$$\kappa = \left\{ \begin{array}{ll} typeI \rightarrow & \begin{cases} \frac{(P_{c1}+P_{c2}+P_m)}{3} \times \xi & z_0 \leq z \leq z_1 \\ 0 & z_1 \leq z \leq z_2 \\ \frac{(P_{c1}+P_{c2}+P_m)}{3} \times \xi & z_2 \leq z \leq z_3 \end{cases} \\ typeII \rightarrow & \begin{cases} \frac{(P_{c1}+P_{c2}+P_m)}{3} \times \xi \times (1 - \frac{|2z-(h_0+h_1)|}{h_1-h_0}) & z_0 \leq z \leq z_1 \\ 0 & z_1 \leq z \leq z_2 \\ \frac{(P_{c1}+P_{c2}+P_m)}{3} \times \xi \times (1 - \frac{|2z-(h_2+h_3)|}{h_3-h_2}) & z_2 \leq z \leq z_3 \end{cases} \\ typeIII \rightarrow & \begin{cases} \log(1+\frac{\xi}{3}) \times (P_{c1}+P_{c2}+P_m) \times (1 - \frac{|2z-(h_0+h_1)|}{h_1-h_0}) & z_0 \leq z \leq z_1 \\ 0 & z_1 \leq z \leq z_2 \\ \log(1+\frac{\xi}{3}) \times (P_{c1}+P_{c2}+P_m) \times (1 - \frac{|2z-(h_2+h_3)|}{h_3-h_2}) & z_2 \leq z \leq z_3 \end{cases} \\ typeVI \rightarrow & \begin{cases} \xi \times \frac{(P_{c1}+P_{c2}+P_m)}{3} \times (1 - \frac{(z-h_1)|}{h_0-h_1}) & z_0 \leq z \leq z_1 \\ 0 & z_1 \leq z \leq z_2 \\ \xi \times \frac{(P_{c1}+P_{c2}+P_m)}{3} \times (1 - \frac{(z-h_3)|}{h_2-h_3}) & z_2 \leq z \leq z_3 \end{cases} \end{array} \right\} \tag{2.56}$$

for type C:

$$\kappa = \left\{ \begin{array}{ll} typeI \rightarrow & \begin{cases} 0 & z_0 \leq z \leq z_1 \\ \frac{(P_{c1}+P_{c2}+P_m)}{3} \times \xi & z_1 \leq z \leq z_2 \\ \frac{(P_{c1}+P_{c2})}{2} \times \xi & z_2 \leq z \leq z_3 \end{cases} \\ typeII \rightarrow & \begin{cases} 0 & z_0 \leq z \leq z_1 \\ \frac{(P_{c1}+P_{c2}+P_m)}{3} \times \xi \times (1 - \frac{|2z-(h_2+h_1)|}{h_2-h_1}) & z_1 \leq z \leq z_2 \\ \frac{(P_{c1}+P_{c2})}{2} \times \xi \times (1 - \frac{|2z-(h_2+h_3)|}{h_3-h_2}) & z_2 \leq z \leq z_3 \end{cases} \\ typeIII \rightarrow & \begin{cases} 0 & z_0 \leq z \leq z_1 \\ \log(1+\frac{\xi}{3}) \times (P_{c1}+P_{c2}+P_m) \times (1 - \frac{|2z-(h_1+h_2)|}{h_2-h_1}) & z_1 \leq z \leq z_2 \\ \log(1+\frac{\xi}{2}) \times (P_{c1}+P_{c2}) \times (1 - \frac{|2z-(h_2+h_3)|}{h_3-h_2}) & z_2 \leq z \leq z_3 \end{cases} \\ typeVI \rightarrow & \begin{cases} 0 & z_0 \leq z \leq z_1 \\ \xi \times \frac{(P_{c1}+P_{c2}+P_m)}{3} \times (1 - \frac{(z-h_2)}{h_1-h_2}) & z_0 \leq z \leq z_1 \\ \xi \times \frac{(P_{c1}+P_{c2})}{2} \times (1 - \frac{(z-h_3)}{h_2-h_3}) & z_2 \leq z \leq z_3 \end{cases} \end{array} \right\} \tag{2.57}$$

for type D:

$$\kappa = \begin{Bmatrix} typeI \rightarrow & \begin{cases} \frac{(P_{c1}+P_{c2}+P_m)}{3} \times \xi & z_0 \leq z \leq z_1 \\ \xi \times \frac{(P_{c1}+P_{c2})}{2} & z_1 \leq z \leq z_2 \\ \frac{(P_{c1}+P_{c2}+P_m)}{3} \times \xi & z_2 \leq z \leq z_3 \end{cases} \\ typeII \rightarrow & \begin{cases} \frac{(P_{c1}+P_{c2}+P_m)}{3} \times \xi \times (1 - \frac{|2z-(h_0+h_1)|}{h_1-h_0}) & z_0 \leq z \leq z_1 \\ \xi \times \frac{(P_{c1}+P_{c2})}{2} \times (1 - \frac{|2z-(h_1+h_2)|}{h_2-h_1}) & z_1 \leq z \leq z_2 \\ \frac{(P_{c1}+P_{c2}+P_m)}{3} \times \xi \times (1 - \frac{|2z-(h_2+h_3)|}{h_3-h_2}) & z_2 \leq z \leq z_3 \end{cases} \\ typeIII \rightarrow & \begin{cases} \log(1+\frac{\xi}{3}) \times (P_{c1}+P_{c2}+P_m) \times (1 - \frac{|2z-(h_0+h_1)|}{h_1-h_0}) & z_0 \leq z \leq z_1 \\ \log(1+\frac{\xi}{2}) \times (P_{c1}+P_{c2}) \times (1 - \frac{|2z-(h_1+h_2)|}{h_2-h_1})0 & z_1 \leq z \leq z_2 \\ \log(1+\frac{\xi}{3}) \times (P_{c1}+P_{c2}+P_m) \times (1 - \frac{|2z-(h_2+h_3)|}{h_3-h_2}) & z_2 \leq z \leq z_3 \end{cases} \\ typeVI \rightarrow & \begin{cases} \xi \times \frac{(P_{c1}+P_{c2}+P_m)}{3} \times (1 - \frac{(z-h_1)}{h_0-h_1}) & z_0 \leq z \leq z_1 \\ \xi \times \frac{(P_{c1}+P_{c2})}{2} \times (1 - \frac{(z-h_2)}{h_1-h_2}) & z_1 \leq z \leq z_2 \\ \xi \times \frac{(P_{c1}+P_{c2}+P_m)}{3} \times (1 - \frac{(z-h_3)|}{h_2-h_3}) & z_2 \leq z \leq z_3 \end{cases} \end{Bmatrix} \tag{2.58}$$

where in the aferomentioned equations V (x) denotes the variation of volume fraction in x-direction, and it is calculated as follows: $V(x) = (\frac{a-x}{a})^{n_x}$.

Figure 2.3 illustrates the variation in the effective Young's modulus of a bi-directional functionally graded sandwich shell, considering thickness ratios of $1-1-1$ and $1-0-1$ under the influence of uniformly distributed porosity. Each plot highlights three layers: the top represents an ideal FGM, while the bottom shows an imperfect FGM with a porosity value of ξ=0.2. The shell structure is made up of Al_2O_3 and ZrO_2 as ceramics (layers 1 and 2), and Al as the metallic component. The introduction of porosity reduces the Young's modulus, disrupting material continuity, particularly for the $1-1-1$ configuration. Here, a significant decrease in modulus is observed at the interface between the core layer and the outer face sheets, causing the material to behave similarly to a conventional composite, which could potentially lead to delamination under specific conditions. For the $1-0-1$ configuration, this behavior is noted only once in FGM type C, as the bottom layer remains homogeneous. This phenomenon occurs when a homogeneous layer is adjacent to an FGM layer, a factor that should be carefully considered during the manufacturing process.

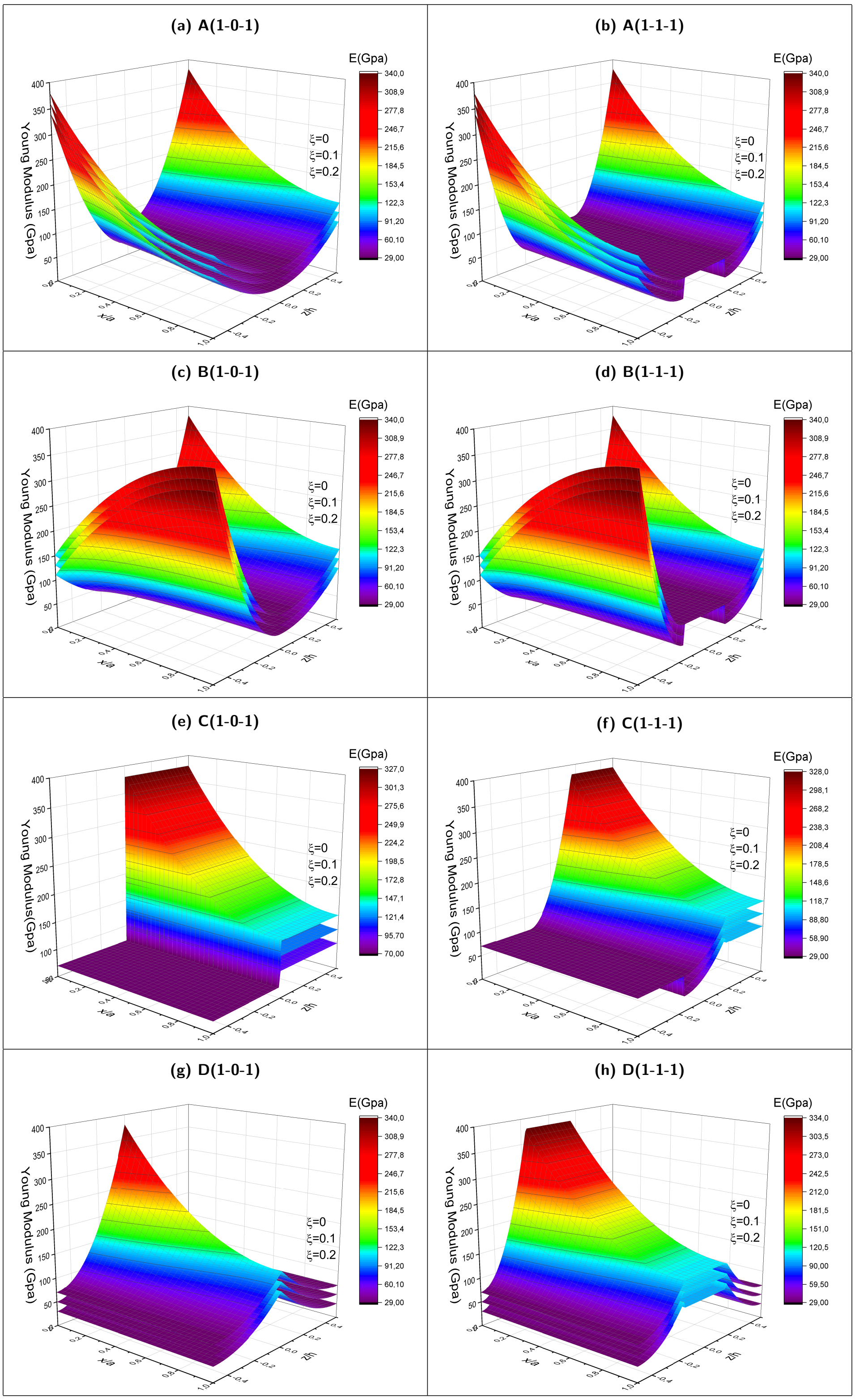

Figure 2.3: porosity effect on young's modulus variation for a bi-directional functionally graded sandwich shell with thickness ration 1−0−1 and 1−1−1.

2.6 P-version Finite element Method

The finite element method (FEM) is a powerful computational technique used for solving complex engineering and physical problems by breaking down structures into smaller, manageable parts called elements. Traditional finite element methods, commonly referred to as the h-version, rely on refining the mesh by increasing the number of elements (reducing the element size, h) to improve the solution's accuracy. However, this approach can lead to a significant increase in computational cost and complexity, especially for problems involving intricate geometries and higher-order behaviors. An alternative approach is the p-version of the finite element method, which enhances the solution accuracy by increasing the polynomial order of the shape functions within each element rather than subdividing the mesh. This method maintains a coarser mesh but employs higher-order polynomials to approximate the solution more accurately within each element. The p-version FEM has gained prominence due to its several advantages over the traditional h-version:

1) **Higher Accuracy with Fewer Degrees of Freedom:**The p-version finite element method (FEM) offers a significant advantage in achieving higher accuracy while minimizing the number of degrees of freedom in a computational model. This is primarily accomplished through the utilization of higher-order polynomial functions, which provide a more refined approximation of the solution within each finite element. Unlike traditional methods that may require a finer mesh—thereby increasing the number of elements to enhance accuracy—the p-version FEM leverages these higher-order polynomials to effectively capture complex behavior with relatively fewer elements.This capability translates to a more efficient computational process. By requiring fewer degrees of freedom, the p-version FEM not only reduces the overall computational load but also decreases the time and resources necessary for simulations. Consequently, this efficiency allows for more complex problems to be tackled within reasonable time frames, enabling researchers and engineers to explore a wider range of scenarios and refine their analyses without the prohibitive costs often associated with extensive mesh refinement.

2) **Faster Convergence Rates:**One of the notable advantages of the p-version finite element method (FEM) is its ability to achieve faster convergence rates when compared to the h-version of FEM.As the degree of the polynomial increases, the approximation error diminishes at a more accelerated pace. This characteristic allows the p-version FEM to yield highly accurate solutions even when utilizing relatively coarse meshes, which consist of fewer elements. In contrast, the h-version FEM often requires a finer mesh to achieve similar levels of accuracy, resulting in

a greater number of elements and, consequently, a more substantial computational burden.The faster convergence rates of the p-version FEM not only facilitate quicker attainment of accurate solutions but also make it particularly advantageous in scenarios where computational resources are limited or time constraints are critical. For instance, in engineering design optimizations or real-time simulations, the ability to derive precise results efficiently can lead to enhanced decision-making and improved outcomes.Moreover, this rapid convergence means that practitioners can invest less time in mesh refinement and focus more on exploring various design alternatives or conducting sensitivity analyses. It also opens up possibilities for more complex geometries and boundary conditions to be analyzed within a practical timeframe, thereby broadening the scope of problems that can be effectively addressed.

3) **Better Representation of Complex Geometries:**One of the standout benefits of the p-version finite element method (FEM) is its superior capability to represent complex geometrical features and curved boundaries with remarkable accuracy. The utilization of higher-order polynomial functions in this method allows for a more precise approximation of intricate shapes, which is particularly advantageous in engineering applications that involve challenging geometries, such as shell structures, automotive components, and aerospace designs.Traditional finite element methods often struggle to adequately capture the nuances of complex geometries, leading to potential inaccuracies in stress and deformation predictions. In contrast, the p-version FEM excels in this regard, as the higher-order polynomials enable a finer representation of curves and surfaces within the finite elements. This capability is essential for modeling features like fillets, chamfers, and other intricate shapes that are prevalent in modern engineering designs.Additionally, the p-version FEM's isogeometric capabilities further enhance its ability to handle complex geometries. For instance, it can be integrated with Coons patches, a mathematical tool used to create smooth surfaces that blend multiple boundary curves. This integration allows engineers to model curved geometries more naturally and intuitively, aligning closely with the actual design intent. Such an approach not only improves accuracy but also streamlines the design process, as engineers can directly utilize CAD geometries without extensive meshing or simplifications.The improved representation of complex geometries is crucial for many engineering applications, where the performance of a structure can be heavily influenced by its shape. In the case of shell structures, for instance, accurate modeling of curved boundaries is vital for predicting phenomena such as buckling, vibrations, and load distribution. By accurately capturing these geometric intricacies, the p-version FEM enables more reliable analyses and

optimizations, ultimately leading to safer and more efficient designs.

4) **Flexibility in Mesh Adaptation:**The p-version finite element method (FEM) offers remarkable flexibility in mesh adaptation, a critical feature for effectively addressing complex engineering problems. One of the key advantages of this approach is the ability to vary the polynomial degree across the mesh, which allows for a tailored representation of the solution based on the specific needs of different regions within the model.In practical applications, some areas of a structure may experience high-stress concentrations, complex loading conditions, or intricate geometrical features that demand a higher level of accuracy. In such cases, the p-version FEM enables the use of higher-order polynomial approximations in these critical regions. This targeted application of more sophisticated approximations ensures that the model captures the nuances of behavior in areas where it matters most, leading to more precise predictions of stress, strain, and deformation.Conversely, in regions where the structural response is less critical or where the geometry is simpler, the p-version FEM allows for the use of lower-order polynomials. This not only conserves computational resources but also simplifies the analysis without sacrificing the overall accuracy of the model. By optimizing the polynomial degree throughout the mesh, engineers can achieve a balanced and efficient computational process that minimizes unnecessary complexity.This flexibility in mesh adaptation is particularly beneficial in iterative design processes, where engineers may need to refine models based on evolving requirements or new insights. It allows for rapid adjustments to be made without the need for extensive re-meshing, making the analysis more efficient and responsive to design changes. As a result, engineers can conduct sensitivity analyses, explore various design alternatives, and optimize performance more effectively.Furthermore, this adaptive approach enhances the robustness of the numerical solution, as it mitigates the potential for convergence issues that can arise from overly refined or uniformly coarse meshes. By intelligently distributing the polynomial degrees based on the local characteristics of the problem, the p-version FEM improves overall solution stability and accuracy.

5) **Reduction of Spurious Oscillations**: In certain problems, especially those involving sharp gradients or discontinuities, the p-version FEM is more effective in reducing spurious oscillations in the solution, leading to more stable and reliable results.

In the context of shell structures, the p-version FEM is particularly advantageous. Shell structures, with their varying curvatures and thicknesses, pose significant challenges in terms of numerical modeling and accuracy. The p-version FEM, combined with advanced theories such as the third-order shear deformation theory (TSDT), can provide a robust framework for analyzing the static, dynamic, and thermal behaviors of these complex structures. In this thesis, we leverage the p-version finite element method to develop a new type of shell element based on the thick shell theory and TSDT. The developed shell element is implemented in a computer code, which is tested and validated through various numerical experiments. The code's performance is evaluated by analyzing a range of shell structures exhibiting free vibration, bending, and thermal buckling behaviors, for both isotropic and bi-directional functionally graded materials. The results demonstrate the effectiveness and accuracy of the p-version FEM in capturing the intricate behaviors of shell structures.

2.6.1 Heirarchical shape Functions

Hierarchical shape functions, derived from the integrals of Legendre polynomials, represent the nodes, edges, and vertices of quadrilateral and triangular elements. These shape functions are identical for nodes and edges in both the product and trunk spaces, differing only in the number of internal shape functions.In the subsequent section, only the shape functions for quadrilateral elements will be detailed, as they are the focus of this thesis.

- four-node shape functions:

$$
\begin{aligned}
N_1(\xi,\eta) &= \phi_1(\xi) \times \phi_1(\eta) \\
N_2(\xi,\eta) &= \phi_2(\xi) \times \phi_1(\eta) \\
N_3(\xi,\eta) &= \phi_2(\xi) \times \phi_2(\eta) \\
N_4(\xi,\eta) &= \phi_1(\xi) \times \phi_2(\eta)
\end{aligned}
\tag{2.59}
$$

- The side shape functions are created by multiplying linear blending functions by the shape functions provided for the one-dimensional element (4(p-1) shape function):

$$
\begin{aligned}
&\text{side1:} \quad N_1(\xi,\eta) = \phi_1(\eta) \times \phi_{i+2}(\xi) \\
&\text{side2:} \quad N_2(\xi,\eta) = \phi_2(\xi) \times \phi_{i+2}(\eta) \\
&\text{side3:} \quad N_3(\xi,\eta) = \phi_2(\eta) \times \phi_{i+2}(\xi) \\
&\text{side4:} \quad N_4(\xi,\eta) = \phi_1(\xi) \times \phi_{i+2}(\eta)
\end{aligned}
\tag{2.60}
$$

- $(\text{p-1})^2$ internal shape function:

$$
N_{kl}(\xi,\eta) = \phi_{i+2}(\xi)\phi_{j+2}(\eta) \tag{2.61}
$$

The bubble mode can be created using following integarle:

$$\phi_1(\xi) = 1 - \xi; \phi_2(\xi) = \xi; \phi_{k+1}(\xi) = \sqrt{2k-1}\int_0^{\xi} P_{k-1}(t)dt, k = 2, 3, \ldots \tag{2.62}$$

$$\phi_1(\eta) = 1 - \eta; \phi_2(\eta) = \eta; \phi_{k+1}(\eta) = \sqrt{2k-1}\int_0^{\eta} P_{k-1}(t)dt, k = 2, 3, \ldots \tag{2.63}$$

Where P_{k-1} could be evaluated using the following recursive relationship:

$$P_0(t) = 1; P_1(t) = 2t - 1 \tag{2.64}$$

$$P_{r+1}(t) = \frac{1}{r+1}[(-2r - 1 + (4r+2)t)P_r(t) - rP_{r-1}(t)]; r = 1, 2, \cdots \tag{2.65}$$

These functions adhere to the following orthogonality condition:

$$\int_0^1 \frac{\mathrm{d}\phi_i(\xi)}{\mathrm{d}\xi}\frac{\mathrm{d}\phi_j(\xi)}{\mathrm{d}\xi}\,\mathrm{d}\xi = \begin{cases} 1 & \text{if } j = i \\ 0 & \text{if } j \neq i \end{cases} \tag{2.66}$$

Table 2.1: Internal shape functions g_{j+1} (j=2,3,...,10), [1]

j	g_{j+1}
2	$\sqrt{3}(\xi^2 - \xi)$
3	$\sqrt{5}(2\xi^3 - 3\xi^2 + \xi)$
4	$\sqrt{7}(5\xi^4 - 10\xi^3 + 6\xi^2 - \xi)$
5	$3(14\xi^5 - 35\xi^4 + 30\xi^3 - 10\xi^2 + \xi)$
6	$\sqrt{11}(42\xi^6 - 126\xi^5 + 140\xi^4 - 70\xi^3 + 15\xi^2 - \xi)$
7	$\sqrt{13}(132\xi^7 - 462\xi^6 + 630\xi^5 - 420\xi^4 + 140\xi^3 - 21\xi^2 + \xi)$
8	$\sqrt{15}(429\xi^8 - 1716\xi^7 + 2772\xi^6 - 2310\xi^5 + 1050\xi^4 - 252\xi^3 + 28\xi^2 - \xi)$
9	$\sqrt{17}(1430\xi^9 - 6435\xi^8 + 12012\xi^7 - 12012\xi^6 + 6930\xi^5 - 2310\xi^4 + 420\xi^3 - 36\xi^2 + \xi)$
10	$\sqrt{19}(4862\xi^{10} - 24310\xi^9 + 51480\xi^8 - 60060\xi^7 + 42042\xi^6 - 18018\xi^5 + 4620\xi^4 - 660\xi^3 + 45\xi^2 - \xi)$

2.6.2 Mesh Mapping

Mapping functions play a crucial role in finite element analysis (FEA) by transforming a standard, reference element into the individual elements that constitute the mesh of the actual problem domain. In FEA, the standard element, typically defined in a simple coordinate system (e.g., a unit square or triangle), serves as a template. This template

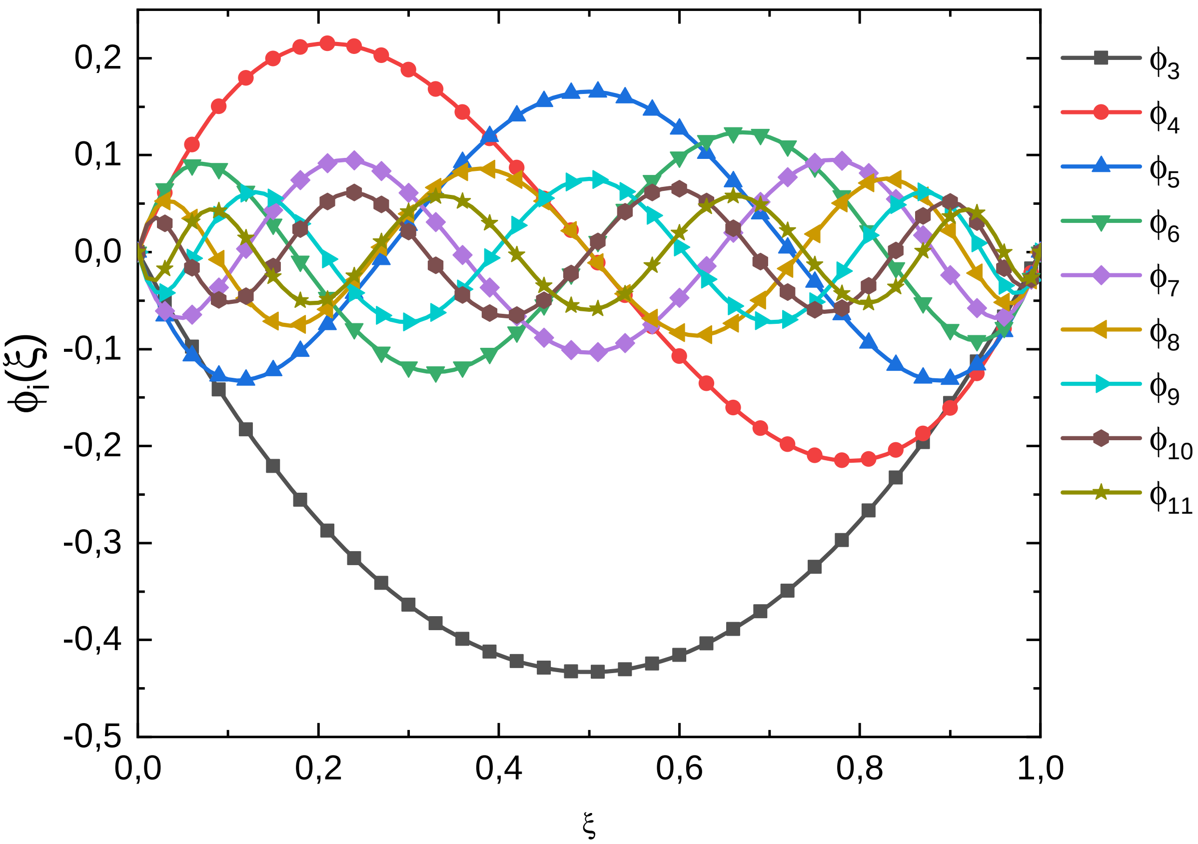

Figure 2.4: bubble modes variation in the domain

is then mapped to different elements within the mesh, which may vary in size, shape, or orientation. The advantage of using a standard element is that the same computational framework can be applied to all elements, reducing complexity and improving efficiency. By applying the mapping function, the geometric properties of the actual elements are accurately represented, while all calculations can still be performed on the standard element in its local coordinate system. This process facilitates the application of shape functions and integration over arbitrary domains, allowing for more flexible meshing strategies that can handle complex geometries with varying element sizes and curvatures.

2.6.2.1 Isoparametric mapping

Isoparametric mapping typically relies on the shape functions described in Section 2.6.1, with the most commonly used procedures being linear and quadratic mappings. These are well-suited for lower-order elements; however, in the present case, we are dealing with higher-order elements, which necessitates a more generalized approach to the mapping function. For a quadrilateral element, the mapping function can be expressed as [89]:

$$x = Q(\xi, \eta) = \sum_{i=1}^{n} N_i(\xi, \eta) X_i \tag{2.67}$$

$$y = Q(\xi, \eta) = \sum_{i=1}^{n} N_i(\xi, \eta) Y_i \tag{2.68}$$

where $N_i(\xi, \eta)$ are the shape functions corresponding to node i, and (X_i, Y_i) are the global coordinates of vertex i of the element, with n representing the total number of nodes.

2.6.2.2 Blending Function method

Although this technique was not utilized in the current work, we provide a brief description for the sake of completeness, as its application in conjunction with the p-version FEM can offer a powerful algorithm for analyzing complex geometries. The blending function method is an effective approach for constructing mapping functions, particularly for elements with curved boundaries. Unlike traditional isoparametric mapping, which primarily relies on shape functions such as Lagrange or Legendre polynomials, the blending function method focuses on smoothly transitioning between known boundary conditions to generate the element's interior.

In this method, blending functions are used to combine the geometries of the edges (or

surfaces in 3D) of an element to generate its internal shape. The method is particularly well-suited for elements with complex or curved boundaries, as it ensures smooth transitions and accurate geometry representation.
The mapping functions are defined by the following equation [90]:

$$\begin{aligned} x(\xi,\eta) =&(1-\eta)x_1(\xi)+\xi x_2(\eta)+\eta x_3(\xi)+(1-\xi)x_4(\eta) \\ &-(1-\xi)(1-\eta)X_1-\xi(1-\eta)X_2-\xi\eta X_3-(1-\xi)\eta X_4 \end{aligned} \tag{2.69}$$

$$\begin{aligned} y(\xi,\eta) =&(1-\eta)y_1(\xi)+\xi y_2(\eta)+\eta y_3(\xi)+(1-\xi)y_4(\eta) \\ &-(1-\xi)(1-\eta)Y_1-\xi(1-\eta)Y_2-\xi\eta Y_3-(1-\xi)\eta Y_4 \end{aligned} \tag{2.70}$$

In the previous relationship, $x_i(\xi,\eta)$ and $y_i(\xi,\eta)$ represent the parametric functions of the element's sides, while X_i and Y_i denote the coordinates of the element's vertex nodes.

2.7 Boundary Conditions

In this research, several types of boundary conditions—namely clamped, simply-supported, and free—are systematically examined along the edges of the panel. These boundary conditions play a crucial role in restricting the movement of the panel, effectively simulating different real-world constraints. By imposing these support conditions, the complexity of the final equilibrium equations is reduced, as the number of degrees of freedom and unknowns is minimized. This simplification not only aids in achieving more efficient computational analysis but also enhances the accuracy of the numerical results. The specific implementation and characteristics of each support condition are detailed in Table 2.2, where their impact on both the structural behavior and the governing equations is thoroughly outlined.

2.8 Summary

This chapter presents a comprehensive mathematical model for the analysis of free vibration, thermal buckling, and static bending of bi-functionally graded materials (bi-FGMs) shell panels.
The mathematical formulation of this model is grounded in the framework of Higher-order Shear Deformation Theory (HSDT). This theoretical framework is crucial as it enables the accurate capture of parabolic variations of transverse shear stresses, which are essential for understanding the structural response of shell panels. By accounting for these

Table 2.2: Sets of Support conditions

CCCC	At x=0,a & y=0,b: u_0=v_0=w_0=θ_x=θ_y= $\overline{u_0}$=$\overline{v_0}$=$\overline{\theta_x}$=$\overline{\theta_y}$=0
SSSS	At x=0,a: v_0=w_0=θ_y=$\overline{v_0}$=$\overline{\theta_y}$=0 At y=0,b: u_0=w_0=θ_x=$\overline{u_0}$=$\overline{\theta_x}$=0
SCSC	At y=0,b: u_0=w_0=θ_x=$\overline{u_0}$=$\overline{\theta_x}$=0 At x=0,a: u_0=v_0=w_0=θ_x=θ_y= $\overline{u_0}$=$\overline{v_0}$=$\overline{\theta_x}$=$\overline{\theta_y}$=0
CCSS	At y=0 & x=a: u_0=v_0=w_0=θ_x=θ_y= $\overline{u_0}$=$\overline{v_0}$=$\overline{\theta_x}$=$\overline{\theta_y}$=0 At x=0: v_0=w_0=θ_y=$\overline{v_0}$=$\overline{\theta_y}$=0 At y=b: u_0=w_0=θ_x=$\overline{u_0}$=$\overline{\theta_x}$=0

shear deformations, the model improves upon classical theories that may overlook such complexities, thereby enhancing the accuracy of the analysis.

The formulation considered three distinct temperature distributions: uniform, linear, and nonlinear. Each of these distributions represents different thermal loading scenarios that can occur in real-world applications. A uniform temperature distribution assumes constant temperature across the thickness, while a linear distribution suggests a gradual change. The nonlinear temperature distribution, on the other hand, reflects more complex thermal profiles that are often observed in practice.

To ensure a comprehensive evaluation of the structural performance, equilibrium equations are derived for a variety of structural scenarios, including static loading conditions, free vibration analyses, and buckling phenomena. These scenarios are crucial for understanding how FG shell panels behave under different operational conditions and for predicting failure modes.

Subsequent chapters will delve into detailed discussions of the results obtained from this analysis, providing insights into the behavior of functionally graded shell panels under thermal loads.

Chapter 3

Static Behaviour of FG shell panel under Mechanical load

3.1 Introduction

Static analysis is a foundational aspect of engineering design and analysis, playing a crucial role in ensuring the safety, stability, and functionality of civil, mechanical, and aerospace systems. Through static analysis, engineers can meticulously evaluate how structures respond to diverse loading conditions, such as gravitational forces, applied loads, and support reactions, without factoring in the effects of time or dynamic forces. This methodical examination allows engineers to comprehensively assess the internal forces, stresses, and deformations present within a structure, offering invaluable insights into its structural integrity and performance. Moreover, static analysis serves as a proactive tool for identifying critical areas susceptible to failure or excessive deformation, empowering engineers to make informed design adjustments and implement optimization strategies aimed at enhancing structural robustness and efficiency. Ultimately, static analysis stands as a cornerstone in the design, construction, and maintenance of engineering structures, ensuring their compliance with regulatory standards and alignment with the functional requirements of their intended applications.

The primary goal of FG shell panel structures and their components is to withstand harsh environmental conditions, including the imposition of high compressive loads resulting from elevated stress fields. Achieving accurate predictions of deformation behavior in such hostile environments necessitates precise modeling of FGM structures, which must account for geometric distortions. It is widely recognized that deflection follows a linear trend within a specific load range. Thus, this chapter is dedicated to analyzing and characterizing the linear flexural behavior of FG shell panels (flat, spherical, cylindrical, hyperbolic, and elliptical) under mechanical stress conditions. To accomplish this objective, a comprehensive linear mathematical model, rooted in the HSDT model, has been developed in preceding chapters. In Section 2, the governing equation for FG shell panels under mechanical loading conditions is derived, accompanied by a detailed explanation of the solution steps.

Table 3.1: The material properties of the ingredients of bi-directional functionally graded sandwich shells

Components	Young's modulus (Gpa)	Poisson's ratio	Mass density kg/m^3
Al_2O_3	380	0.3	3800
ZrO_2	151	0.3	3000
Al	70	0.3	2707

3.2 Solution Methodology

For the static bending analysis, we will examine the behavior of four types of sandwich shell panels, each consisting of three layers. These configurations were originally proposed by Vinh [88] and formulated in the preceding chapter. The dimensions of the shell panels include length (a), width (b), and thickness (h). In the upcoming examples, the functionally graded (FG) shell panels will be subjected to either a uniformly distributed load or a sinusoidally distributed load.

Each functionally graded sandwich shell comprises three layers: a core layer and two face sheets. The thickness of the bottom and top face sheets, as well as the core layer, is denoted by h1, h2, and h3, respectively. The coordinates of the top and bottom of each layer are represented by z with respect to the neutral plane, as depicted by the discontinuous line in Figure 2.2. Commonly found thickness ratios for sandwich shells in literature are 1−0−1, 1−1−1, 1−2−1, and 2−2−1.

Sandwich shells of types A and B consist of a metal core layer and two bi-directional functionally graded material (FGM) face sheets. Type C sandwich shells are composed of a bi-directional FGM core layer, a bottom metal face sheet, and a top in-plane FGM face sheet. Type D shells have an in-plane FGM core and two bi-directional FGM face sheets. The material properties remain constant for the metal layer, vary in the x-direction for the in-plane FGM layer, and vary in both the x- and z-direction for the composite layer. Four types of porosity distribution are introduced and investigated in static bending for different shell geometries. It is assumed that only homogeneous metallic layers among the four types of sandwich shells are unaffected by porosity effects.In the subsequent section, for the sake of consistency, non-dimensional values will be adopted for both center deflection and axial stress: $\overline{w_c} = \frac{10hE_0}{q_0 \cdot a} \cdot w(\frac{a}{2}, \frac{b}{2})$, $\overline{\sigma_x} = \frac{h}{q_0 a}\sigma_x(\frac{a}{2}, \frac{b}{2}, \frac{h}{2})$

3.3 Results & Discussion

3.3.1 Validation Analysis

In the initial validation example (table 3.2), a plate with fully simply supported edges is examined, and its bending behavior under a double sinusoidally distributed load is analyzed. The results of the non-dimensional center of deflection are presented in Table 4. The functionally graded material (FGM) in this case belongs to type D, where ceramic 1 and 2 consist of ZrO_2 and the metal component is Aluminum (Al). The plate has a length-to-thickness ratio of $a/h = 10$ and is subjected to SSSS boundary conditions,the polynome degree was set to p=7 for generating the data. The analysis reveals that the center of deflection values increase with the power law index n_z. Furthermore, the highest deflection values are observed for the 1−0−1 configuration, attributed to the absence of a core layer, which typically acts as reinforcement.

Table 3.2: Dimensionless center deflection ($\overline{w_c}$) of square functionally graded sandwich plates (SSSS, a/h=10)

n_z	Source	1−0−1	2−1−2	2−1−1	1−1−1	2−2−1	1−2−1
0	Present	0.19606	0.19606	0.19606	0.19606	0.19606	0.19606
	TSDT [88]	0.19584	0.19586	0.19584	0.19584	0.19584	0.19584
	TSDT [91]	0.19606	0.19606		0.19606	0.19606	0.19606
	SSDT [91]	0.19605	0.19605		0.19605	0.19605	0.19605
	iTrSDT [92]	0.19597	0.19597	0.19597	0.19597	0.19597	0.19597
	Q3D [93]	0.19487	0.19487		0.19487	0.19487	0.19487
	Q3D [94]		0.19490	0.19490	0.19490	0.19490	0.19490
	Q3D [95]		0.19486	0.19486	0.19686	0.19486	0.19486
1	Present	0.32362	0.30534	0.29679	0.29200	0.28086	0.27094
	TSDT [88]	0.32323	0.30598	0.29643	0.29168	0.28056	0.27066
	TSDT [91]	0.32358	0.30632		0.29199	0.28085	0.27094
	SSDT [91]	0.32349	0.30624		0.29194	0.28082	0.27093

Continued on next page

$\mathbf{n}_z$	**Source**	1–0–1	2–1–2	2–1–1	1–1–1	2–2–1	1–2–1
	iTrSDT [92]	0.32348	0.30622	0.29666	0.29191	0.28077	0.27086
	Q3D [93]	0.32001	0.30275		0.28867	0.27760	0.26815
	Q3D [94]		0.30700	0.29750	0.29290	0.28200	0.27220
	Q3D [95]		0.30430	0.29448	0.29007	0.27874	0.26915
2	Present	0.37348	0.35244	0.33794	0.33296	0.31624	0.30263
	TSDT [88]	0.37292	0.35192	0.33741	0.33252	0.31582	0.30231
	TSDT [91]	0.37335	0.35231		0.33289	0.31617	0.30263
	SSDT [91]	0.37319	0.35218		0.33280	0.31611	0.30260
	iTrSDT [92]	0.37322	0.35221	0.33769	0.33279	0.31608	0.30255
	Q3D [93]	0.36891	0.34737		0.32816	0.31152	0.29874
	Q3D [94]		0.35190	0.33760	0.33290	0.31640	0.30320
	Q3D [95]		0.35001	0.33495	0.33068	0.31356	0.30060
5	Present	0.40944	0.39212	0.37344	0.37167	0.34983	0.33486
	TSDT [88]	0.40880	0.39137	0.37264	0.37102	0.34921	0.33443
	TSDT [91]	0.40927	0.39183		0.37145	0.34960	0.33480
	SSDT [91]	0.40905	0.39160		0.37128	0.34950	0.33474
	iTrSDT [92]	0.40911	0.39170	0.37295	0.37134	0.34950	0.33472
	Q3D [93]	0.40532	0.38612		0.36546	0.34361	0.32966
	Q3D [94]		0.39050	0.37220	0.37050	0.34900	0.33470
	Q3D [95]		0.38934	0.36981	0.36902	0.34649	0.33255
10	Present	0.41781	0.40442	0.38487	0.38582	0.36245	0.34834
	TSDT [88]	0.41724	0.40360	0.38398	0.38506	0.36171	0.34785
	TSDT [91]	0.41772	0.40407		0.38551	0.36215	0.34824
	SSDT [91]	0.41750	0.40376		0.38490	0.34916	0.34119
	iTrSDT [92]	0.41754	0.40393	0.38540	0.38540	0.36202	0.34815
	Q3D [93]	0.41448	0.39856		0.37924	0.35577	0.34259
	Q3D [94]		0.40260	0.38350	0.38430	0.36120	0.34800
	Q3D [95]		0.40153	0.38111	0.38303	0.35885	0.34591

Table 3.3 is provided, with consistent assumptions regarding material composition, plate geometry, and boundary conditions. The results illustrate the dimensionless stress variation for multiple sandwich plates with different index values, exhibiting notable similarities to findings reported in existing literature.

Table 3.3: Comparison of dimensionless axial stress $\overline{\sigma_x}$ of ZrO_2/Al square sandwich plate (a/h=10,type D)

$\mathbf{n}_z$	**Source**	1−0−1	2−1−2	2−1−1	1−1−1	2−2−1	1−2−1
0	Present	1.99392	1.99392	1.99392	1.99392	1.99392	1.99392
	TSDT [88]	1.98542	1.98542	1.98542	1.98542	1.98542	1.98542
	TSDT [91]	2.04985	2.04985		2.04985	2.04985	2.04985
	TSDT [91]	2.05452	2.05452		2.05452	2.05452	2.05452
	iTrSDT [92]	1.99482	1.99482	1.99482	1.99482	1.99482	1.99482
	Q3D [93]	2.09773	2.00773		2.00773	2.00773	2.00773
	Q3D [94]		2.00660	2.00640	2.00660	2.00650	2.00640
	Q3D [95]		1.99524	1.99524	1.99524	1.99524	1.99524
1	Present	1.54199	1.46080	1.35745	1.39239	1.28855	1.29095
	TSDT [88]	1.53769	1.45667	1.35122	1.38811	1.28304	1.28627
	TSDT [91]	1.57923	1.49587		1.42617	1.32062	1.32309
	TSDT [91]	1.58204	1.49859		1.42892	1.32342	1.32590
	iTrSDT [92]	1.54441	1.46297	1.35703	1.39406	1.28852	1.29174
	Q3D [93]	1.57004	1.48833		1.41781	1.30907	1.31204
	Q3D [93]		1.46130	1.37680	1.41370	1.30920	1.31330
	Q3D [95]		1.46131	1.52329	1.39243	1.28274	1.29030
2	Present	1.78002	1.68304	1.53108	1.59085	1.43728	1.44547
	TSDT [88]	1.77592	1.67949	1.52329	1.58710	1.43083	1.44097
	TSDT [91]	1.82167	1.72144		1.62748	1.47095	1.47988
	TSDT [91]	1.82450	1.72412		1.63025	1.47387	1.48283
	iTrSDT [92]	1.78383	1.68682	1.52988	1.59393	1.43693	1.44707
	Q3D [93]	1.81509	1.72030		1.62591	1.46372	1.47421
	Q3D [94]		1.69940	1.54560	1.60880	1.45430	1.46590
	Q3D [95]		1.68472	1.52101	1.59170	1.42887	1.44497
5	Present	1.94615	1.87182	1.68179	1.77678	1.57738	1.60162
	TSDT [88]	1.94141	1.86872	1.67157	1.77381	1.56942	1.59778
	TSDT [91]	1.99272	1.91302		1.81580	1.61181	1.63814
	TSDT [91]	1.99567	1.91547		1.81838	1.61477	1.64106
	iTrSDT [92]	1.95031	1.87709	1.67895	1.78159	1.57620	1.60459
	Q3D [93]	1.97912	1.91504		1.82018	1.60953	1.63906

Continued on next page

n_z	Source	1−0−1	2−1−2	2−1−1	1−1−1	2−2−1	1−2−1
	Q3D [94]		1.88380	1.69090	1.79060	1.58930	1.61950
	Q3D [95]		1.87516	1.66856	1.77919	1.56627	1.60203
10	Present	1.98046	1.92878	1.73267	1.84391	1.63024	1.66651
	TSDT [88]	1.97463	1.92557	1.72123	1.84115	1.62133	1.66305
	TSDT [91]	2.03036	1.97126		1.88376	1.66660	1.70417
	TSDT [91]	2.03360	1.97313		1.88147	1.61979	1.64851
	iTrSDT [92]	1.98382	1.93431	1.72890	1.84933	1.62840	1.67019
	Q3D [93]	2.00692	1.97075		1.89162	2.18558	1.67350
	Q3D [94]		1.93970	1.74050	1.85590	1.63950	1.68320
	Q3D [95]		1.93266	1.71835	1.84705	1.61792	1.66754

In the final example (table 3.4), a comparative study was conducted to validate the accuracy of the bi-directionality in functionally graded materials within our sandwich panels. Drawing reference from Vinh's [88] work, the study focused on four FGM mixtures that had been proposed. Remarkably close findings were demonstrated for each case scenario, affirming the reliability of the bi-directional approach in our analysis.

Table 3.4: Dimensionless deflection parameter $\bar{w}_c$ for SSSS bi-directional functionally graded flat sandwich shell panel

Mixture	n_x	n_z	Source	1−0−1	2−1−2	2−1−1	1−1−1	2−2−1	1−2−1
A	0	1	Present	0.16013	0.17422	0.18660	0.18813	0.20543	0.21358
			TDST [88]	0.15975	0.17346	0.18567	0.18717	0.20431	0.21277
	1	1	Present	0.22588	0.24182	0.25575	0.25727	0.27618	0.28538
			TSDT [88]	0.22553	0.24122	0.25502	0.25659	0.27539	0.28486
	5	1	Present	0.31519	0.33180	0.34583	0.34764	0.36613	0.37605
			TSDT [88]	0.31479	0.33126	0.34521	0.34709	0.36551	0.37561
B	0	1	Present	0.25002	0.26529	0.27818	0.27941	0.29871	0.30473
			TSDT [88]	0.24943	0.26451	0.27763	0.27863	0.29819	0.30419
	1	1	Present	0.22854	0.24442	0.25797	0.25964	0.27814	0.28724
			TSDT [88]	0.22810	0.24374	0.25720	0.25891	0.27734	0.28671
	5	1	Present	0.24089	0.25645	0.26880	0.27107	0.28711	0.29741

Continued on next page

Mixture	n_x	n_z	Source	1−0−1	2−1−2	2−1−1	1−1−1	2−2−1	1−2−1
			TSDT [88]	0.24036	0.25571	0.26786	0.27030	0.28614	0.29686
C	0	1	Present	0.31675	0.31226	0.33461	0.30474	0.32491	0.29160
			TSDT [88]	0.31570	0.31132	0.33318	0.30400	0.32289	0.29112
	1	1	Present	0.37254	0.36928	0.38439	0.36375	0.27851	0.35384
			TSDT [88]	0.37158	0.36841	0.38325	0.36303	0.37765	0.35335
	5	1	Present	0.43692	0.43495	0.44439	0.43158	0.44162	0.42591
			TSDT [88]	0.43604	0.43414	0.44350	0.43086	0.44088	0.42484
D	0	1	Present	0.30966	0.27395	0.25828	0.24743	0.32014	0.21302
			TSDT [88]	0.30949	0.27383	0.25815	0.24735	0.23006	0.23006
	1	1	Present	0.38921	0.35276	0.33591	0.32679	0.30634	0.28810
			TSDT [88]	0.38789	0.35260	0.33574	0.32523	0.30624	0.30624
	5	1	Present	0.47218	0.44151	0.42539	0.41658	0.39891	0.39089
			TSDT [88]	0.47181	0.44119	0.42506	0.41631	0.39772	0.38067

3.3.2 Parametric Study

3.3.2.1 Gradient indexes and sandwich layups effect

In this section, the analysis explores the influence of gradient index variation on the non-dimensional center deflection across various shell panel geometries, as outlined in Tables [3.5-3.8]. The findings consistently reveal that, regardless of the specific sandwich layup configuration, an increase in either the gradient index n_x or n_z leads to a noticeable rise in deflection values. This trend holds true for all shell geometries considered in the study, highlighting a clear relationship between the gradient index and structural response.

Moreover, the results underscore the superior performance of the 1-0-1 sandwich layup configuration, which consistently yields the smallest deflection values when compared to other configurations. This suggests that the 1-0-1 configuration offers enhanced stiffness and structural stability, making it a more effective design choice for minimizing deflections in functionally graded materials (FGM) shell panels. The uniformity of these findings across multiple geometries reinforces the robustness of the observed trends and provides valuable insights into the optimal gradient index and layup configurations for achieving desired deflection characteristics.

Table 3.5: non-dimensional center deflection $\bar{w}_c$ for bi-directional functionally graded sandwich shell panel FGM type A

R_x/a	R_y/b	$\mathbf{n}_x$	$\mathbf{n}_z$	1−0−1	2−1−2	2−1−1	1−1−1	2−2−1	1−2−1
5	5	0	0	0.10996	0.11481	0.12099	0.12136	0.13170	0.13678
			1	0.14701	0.16078	0.17148	0.17409	0.18932	0.19817
			5	0.24485	0.26908	0.28287	0.29013	0.30853	0.32504
		1	0	0.16170	0.16766	0.17554	0.17544	0.18817	0.19310
			1	0.20719	0.22270	0.23499	0.23740	0.25428	0.26371
			5	0.31376	0.33810	0.35099	0.35860	0.37539	0.39124
		5	0	0.23453	0.24171	0.25002	0.25049	0.26340	0.26965
			1	0.28666	0.30287	0.31352	0.31789	0.33235	0.34424
			5	0.39206	0.41371	0.42183	0.43129	0.44238	0.45802
5	∞	0	0	0.11956	0.12346	0.13024	0.12974	0.14098	0.14540
			1	0.15697	0.17102	0.18287	0.18481	0.20147	0.20996
			5	0.25968	0.28546	0.30078	0.30799	0.32830	0.34564
		1	0	0.17517	0.18000	0.18856	0.18743	0.20118	0.20536
			1	0.22134	0.23722	0.25071	0.25251	0.27089	0.28021
			5	0.33411	0.36032	0.37461	0.38254	0.40109	0.41817
		5	0	0.25537	0.26103	0.27045	0.26926	0.28384	0.28859
			1	0.30815	0.32471	0.33734	0.34038	0.35723	0.36832
			5	0.42036	0.44389	0.45414	0.46312	0.47661	0.49259
5	-5	0	0	0.12383	0.12736	0.13447	0.13355	0.14531	0.14937
			1	0.16151	0.17573	0.18821	0.18976	0.20720	0.21543
			5	0.26654	0.29304	0.30917	0.31624	0.33751	0.35511
		1	0	0.18124	0.18561	0.19451	0.19292	0.20718	0.21102
			1	0.22780	0.24389	0.25794	0.25947	0.27854	0.28783
			5	0.34345	0.37049	0.38541	0.39347	0.41281	0.43042
		5	0	0.26469	0.26972	0.27996	0.27775	0.29357	0.29721
			1	0.31786	0.33462	0.34876	0.35060	0.36924	0.37926
			5	0.43316	0.45753	0.46956	0.47749	0.49286	0.50815
5	7.5	0	0	0.11362	0.11812	0.12452	0.12457	0.13524	0.14008
			1	0.15082	0.16471	0.17583	0.17820	0.19397	0.20269
			5	0.25054	0.27536	0.28972	0.29698	0.31610	0.33294

Continued on next page

R_x/a	R_y/b	$\mathbf{n}_x$	$\mathbf{n}_z$	1−0−1	2−1−2	2−1−1	1−1−1	2−2−1	1−2−1
		1	0	0.16683	0.17238	0.18051	0.18003	0.19314	0.19780
			1	0.21261	0.22826	0.24101	0.24319	0.26064	0.27004
			5	0.32156	0.34661	0.36004	0.36777	0.38523	0.40155
		5	0	0.24246	0.24908	0.25778	0.25766	0.27116	0.27690
			1	0.29487	0.31123	0.32256	0.32650	0.34179	0.35346
			5	0.40289	0.42526	0.43409	0.44347	0.45538	0.47162

Table 3.6: non-dimensional center deflection $\bar{w}_c$ for bi-directional functionally graded sandwich shell panel FGM type B

R_x/a	R_y/b	$\mathbf{n}_x$	$\mathbf{n}_z$	1−0−1	2−1−2	2−1−1	1−1−1	2−2−1	1−2−1
5	5	0	0	0.17922	0.18854	0.19569	0.19716	0.20773	0.21441
			1	0.22703	0.24237	0.25584	0.25616	0.27523	0.28030
			5	0.32640	0.34870	0.37345	0.36759	0.39782	0.39791
		1	0	0.16238	0.16915	0.17750	0.17720	0.19039	0.19491
			1	0.20864	0.22425	0.23674	0.23885	0.25582	0.26486
			5	0.31443	0.33854	0.35142	0.35888	0.37563	0.39133
		5	0	0.17899	0.18724	0.19334	0.19549	0.20816	0.21279
			1	0.22625	0.24164	0.25088	0.25570	0.26851	0.28050
			5	0.32789	0.35071	0.35362	0.36996	0.37540	0.40072
5	∞	0	0	0.19702	0.20505	0.21033	0.21299	0.22209	0.22994
			1	0.24457	0.25993	0.27293	0.27400	0.29319	0.29907
			5	0.34847	0.37234	0.39894	0.39273	0.42554	0.42573
		1	0	0.17709	0.18262	0.19119	0.19021	0.20404	0.20801
			1	0.22369	0.23955	0.25297	0.25465	0.27287	0.28190
			5	0.33516	0.36105	0.37523	0.38304	0.40147	0.41840
		5	0	0.19255	0.19942	0.20746	0.20709	0.22215	0.22432
			1	0.23966	0.25519	0.26661	0.26966	0.28473	0.29559
			5	0.34656	0.37116	0.37523	0.39209	0.39881	0.42584
5	-5	0	0	0.20471	0.21214	0.21674	0.21979	0.22847	0.23666
			1	0.25217	0.26758	0.28058	0.28182	0.30129	0.30737
			5	0.35830	0.38292	0.41048	0.40400	0.43807	0.43823

Continued on next page

R_x/a	R_y/b	$\mathbf{n}_x$	$\mathbf{n}_z$	1−0−1	2−1−2	2−1−1	1−1−1	2−2−1	1−2−1
		1	0	0.18363	0.18866	0.19705	0.19609	0.21000	0.21400
			1	0.23051	0.24653	0.26020	0.26188	0.28054	0.28973
			5	0.34465	0.37133	0.38606	0.39406	0.41322	0.43071
		5	0	0.19570	0.20207	0.21102	0.20963	0.22573	0.22700
			1	0.24298	0.25868	0.27113	0.27342	0.28960	0.29999
			5	0.35265	0.37814	0.38293	0.39992	0.40743	0.43516
5	7.5	0	0	0.18599	0.19485	0.20131	0.20323	0.21325	0.22038
			1	0.23376	0.24912	0.26240	0.26302	0.28212	0.28752
			5	0.33488	0.35778	0.38322	0.37723	0.40844	0.40857
		1	0	0.16798	0.17429	0.18276	0.18218	0.19563	0.19993
			1	0.21440	0.23011	0.24297	0.24490	0.26236	0.27139
			5	0.32237	0.34716	0.36054	0.36814	0.38553	0.40170
		5	0	0.18447	0.19220	0.19902	0.20023	0.21380	0.21749
			1	0.23169	0.24713	0.25719	0.26134	0.27500	0.28656
			5	0.33532	0.35881	0.36214	0.37869	0.38459	0.41057

Table 3.7: non-dimensional center deflection $\bar{w}_c$ for bi-directional functionally graded sandwich shell panel FGM type C

R_x/a	R_y/b	$\mathbf{n}_x$	$\mathbf{n}_z$	1−0−1	2−1−2	2−1−1	1−1−1	2−2−1	1−2−1
5	5	0	0	0.26919	0.23976	0.26919	0.21657	0.23976	0.18647
			1	0.26919	0.26594	0.29034	0.26048	0.28136	0.25083
			5	0.26919	0.28299	0.30329	0.28949	0.30636	0.29605
		1	0	0.32223	0.29939	0.32223	0.27924	0.29939	0.25022
			1	0.32223	0.31981	0.33778	0.31570	0.33192	0.30830
			5	0.32223	0.33202	0.34781	0.33674	0.35133	0.34227
		5	0	0.39140	0.37388	0.39140	0.35710	0.37388	0.33075
			1	0.39140	0.38971	0.40376	0.38680	0.39991	0.38148
			5	0.39140	0.39869	0.41235	0.40251	0.41615	0.40769
5	∞	0	0	0.30431	0.27170	0.30431	0.24472	0.27170	0.20916
			1	0.30431	0.30017	0.32343	0.29322	0.31383	0.28105
			5	0.30431	0.31787	0.33386	0.32324	0.33590	0.32779

Continued on next page

R_x/a	R_y/b	n_x	n_z	1−0−1	2−1−2	2−1−1	1−1−1	2−2−1	1−2−1
		1	0	0.35890	0.33460	0.35890	0.31176	0.33460	0.27809
			1	0.35890	0.35588	0.37203	0.35077	0.36611	0.34160
			5	0.35890	0.36787	0.37984	0.37147	0.38269	0.37535
		5	0	0.42792	0.41129	0.42792	0.39375	0.41129	0.36483
			1	0.42792	0.42597	0.43715	0.42261	0.43389	0.41648
			5	0.42792	0.43362	0.44362	0.43621	0.44708	0.43999
5	-5	0	0	0.31947	0.28564	0.31947	0.25707	0.28564	0.21915
			1	0.31947	0.31493	0.33748	0.30735	0.32769	0.29410
			5	0.31947	0.33278	0.34676	0.33759	0.34837	0.34122
		1	0	0.37572	0.35077	0.37572	0.32668	0.35077	0.29082
			1	0.37572	0.37243	0.38768	0.36685	0.38174	0.35686
			5	0.37572	0.38428	0.39442	0.38733	0.39696	0.39043
		5	0	0.44067	0.42516	0.44067	0.40787	0.42516	0.37857
			1	0.44067	0.43868	0.44821	0.43528	0.44542	0.42905
			5	0.44067	0.44539	0.45372	0.44737	0.45712	0.45056
5	7.5	0	0	0.28238	0.25173	0.28238	0.22713	0.25173	0.19501
			1	0.28238	0.27880	0.30287	0.27280	0.29364	0.26223
			5	0.28238	0.29614	0.31494	0.30226	0.31764	0.30811
		1	0	0.33600	0.31259	0.33600	0.29144	0.31259	0.26070
			1	0.33600	0.33337	0.35072	0.32889	0.34482	0.32084
			5	0.33600	0.34552	0.35996	0.34985	0.36324	0.35479
		5	0	0.40561	0.38832	0.40561	0.37118	0.38832	0.34378
			1	0.40561	0.40381	0.41687	0.40073	0.41321	0.39507
			5	0.40561	0.41236	0.42470	0.41574	0.42836	0.42041

Table 3.8: non-dimensional center deflection $\bar{w}_c$ for bi-directional functionally graded sandwich shell panel FGM type D

R_x/a	R_y/b	n_x	n_z	1−0−1	2−1−2	2−1−1	1−1−1	2−2−1	1−2−1
5	5	0	0	0.10996	0.10996	0.10996	0.10996	0.10996	0.10996
			1	0.26323	0.23264	0.22049	0.21090	0.19733	0.18320
			5	0.50850	0.42758	0.38600	0.36185	0.31892	0.27805

Continued on next page

R_x/a	R_y/b	$\mathbf{n}_x$	$\mathbf{n}_z$	1−0−1	2−1−2	2−1−1	1−1−1	2−2−1	1−2−1
		1	0	0.16170	0.16170	0.16170	0.16170	0.16170	0.16170
			1	0.33514	0.30426	0.29051	0.28130	0.26578	0.25074
			5	0.53734	0.47806	0.44043	0.42516	0.38442	0.34971
		5	0	0.23453	0.23453	0.23453	0.23453	0.23453	0.32453
			1	0.40999	0.38255	0.37114	0.36129	0.34743	0.33165
			5	0.55847	0.51815	0.49410	0.48038	0.45133	0.42138
5	∞	0	0	0.11956	0.11956	0.11956	0.11956	0.11956	0.11956
			1	0.29732	0.26288	0.24826	0.23767	0.22147	0.20514
			5	0.57754	0.49931	0.44800	0.42360	0.37014	0.32146
		1	0	0.17517	0.17517	0.17517	0.17517	0.17517	0.17517
			1	0.37409	0.33990	0.32383	0.31368	0.29558	0.27827
			5	0.60051	0.54438	0.50000	0.48569	0.43716	0.39690
		5	0	0.25537	0.25537	0.25537	0.25537	0.25537	0.25537
			1	0.45583	0.42596	0.41170	0.40200	0.38514	0.36795
			5	0.61835	0.58160	0.55117	0.54137	0.50543	0.47405
5	-5	0	0	0.12383	0.12383	0.12383	0.12383	0.12383	0.12383
			1	0.31231	0.27630	0.26049	0.24955	0.23211	0.31231
			5	0.60824	0.53173	0.47553	0.45155	0.39299	0.60824
		1	0	0.18124	0.18124	0.18124	0.18124	0.18124	0.18124
			1	0.39140	0.35575	0.33875	0.32809	0.30893	0.39140
			5	0.62849	0.57397	0.52678	0.51277	0.46097	0.41798
		5	0	0.26469	0.26469	0.26469	0.26469	0.26469	0.26469
			1	0.47618	0.44525	0.42899	0.42010	0.40134	0.38409
			5	0.64487	0.60976	0.57433	0.56850	0.52780	0.49749
5	7.5	0	0	0.11362	0.11362	0.11362	0.11362	0.11362	0.11362
			1	0.27597	0.24396	0.23091	0.22094	0.20640	0.19145
			5	0.53429	0.45398	0.40893	0.38455	0.33785	0.29412
		1	0	0.16683	0.16683	0.16683	0.16683	0.16683	0.16683
			1	0.34980	0.31767	0.30305	0.29350	0.27701	0.26113
			5	0.56112	0.50279	0.46265	0.44769	0.40407	0.36733
		5	0	0.24246	0.24246	0.24246	0.24246	0.24246	0.24246
			1	0.42728	0.39891	0.38652	0.37664	0.36173	0.34535

Continued on next page

R_x/a	R_y/b	$\mathbf{n}_x$	$\mathbf{n}_z$	1−0−1	2−1−2	2−1−1	1−1−1	2−2−1	1−2−1
			5	0.58111	0.54198	0.51579	0.50323	0.47182	0.44113

3.3.2.2 Mixture type effect on non-dimensional deflection

Figure 3.1 provides a visual representation of the non-dimensional deflection across four distinct mixtures. Here, the focus is on analyzing a rectangular plate configured under an SSSS boundary condition. The non-dimensional deflection is specifically examined at y/b=0.5, encompassing a range of n_x gradient values while maintaining n_z constant at 2. As observed, there is a clear trend indicating that deflection amplifies with increasing n_x values. An intriguing observation emerges as the maximal center of deflection gradually shifts towards the right as n_x escalates, eventually converging back to the center as n_x approaches infinity. This phenomenon underscores the dynamic interplay between gradient index and deflection behavior. However, in the case of configuration B, the deflection pattern remains relatively stable, exhibiting no significant deviations regardless of the gradient index n_x. This contrast highlights the unique deflection characteristics associated with different mixture configurations, shedding light on the intricate dynamics governing their structural response.

3.3.2.3 Gradient Effect of indexes on Axial Stress distribution

Figure 3.2 presents the distribution of normal stress across the thickness of a square bi-directional functionally graded sandwich shell. Specifically, Figures 3.2.c and 3.2.d highlight the influence of the gradient index n_z on the non-dimensional stress distribution for a flat plate compared to a spherical shell, both in the SSSS type D 1−2−1 sandwich configuration.

When $n_z = 0$, the stress exhibits a linear variation throughout the shell thickness, indicating a uniform material property distribution. However, as n_z increases and takes on nonzero values, the stress distribution becomes nonlinear, reflecting the varying material properties across the shell's thickness. In the case of the flat plate, the normal stress distribution is symmetric, with the top and bottom layers experiencing equal stress magnitudes in absolute value but with opposite signs, indicating a balanced stress state.

In contrast, for the spherical shell panel, the neutral plane, where the normal stress $\overline{\sigma_x} = 0$, shifts downward from the mid-plane of the shell. This shift results in a higher stress concentration in the top layer compared to the bottom layer. Despite this asymmetry, the overall shape of the stress variation remains similar to that of the flat plate, demonstrat-

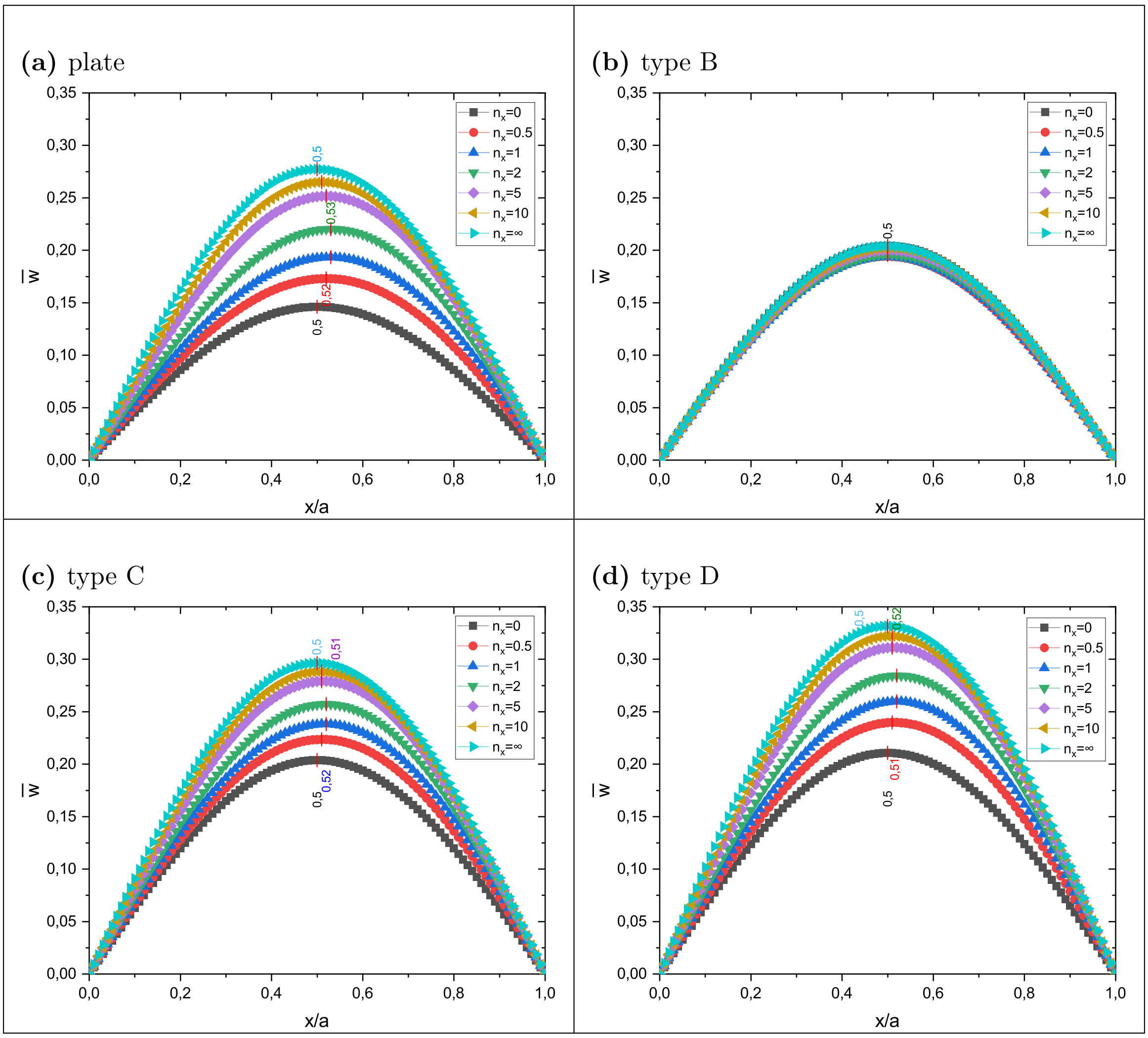

Figure 3.1: Effect of gradient index n_x for different mixtures on SSSS plate non-dimensional deflection n_z=2,h/a=0.1

ing a consistent pattern of stress distribution modified by the shell curvature.
Figures 3.2.a and 3.2.b further illustrate the effect of varying n_x while keeping $n_z = 5$. In this case, the variation of n_x primarily affects the magnitude of the normal stress distribution, while the overall shape remains largely unchanged. This suggests that n_x influences the intensity of the stress response but does not alter the fundamental nature of the stress variation through the thickness of the shell panel.

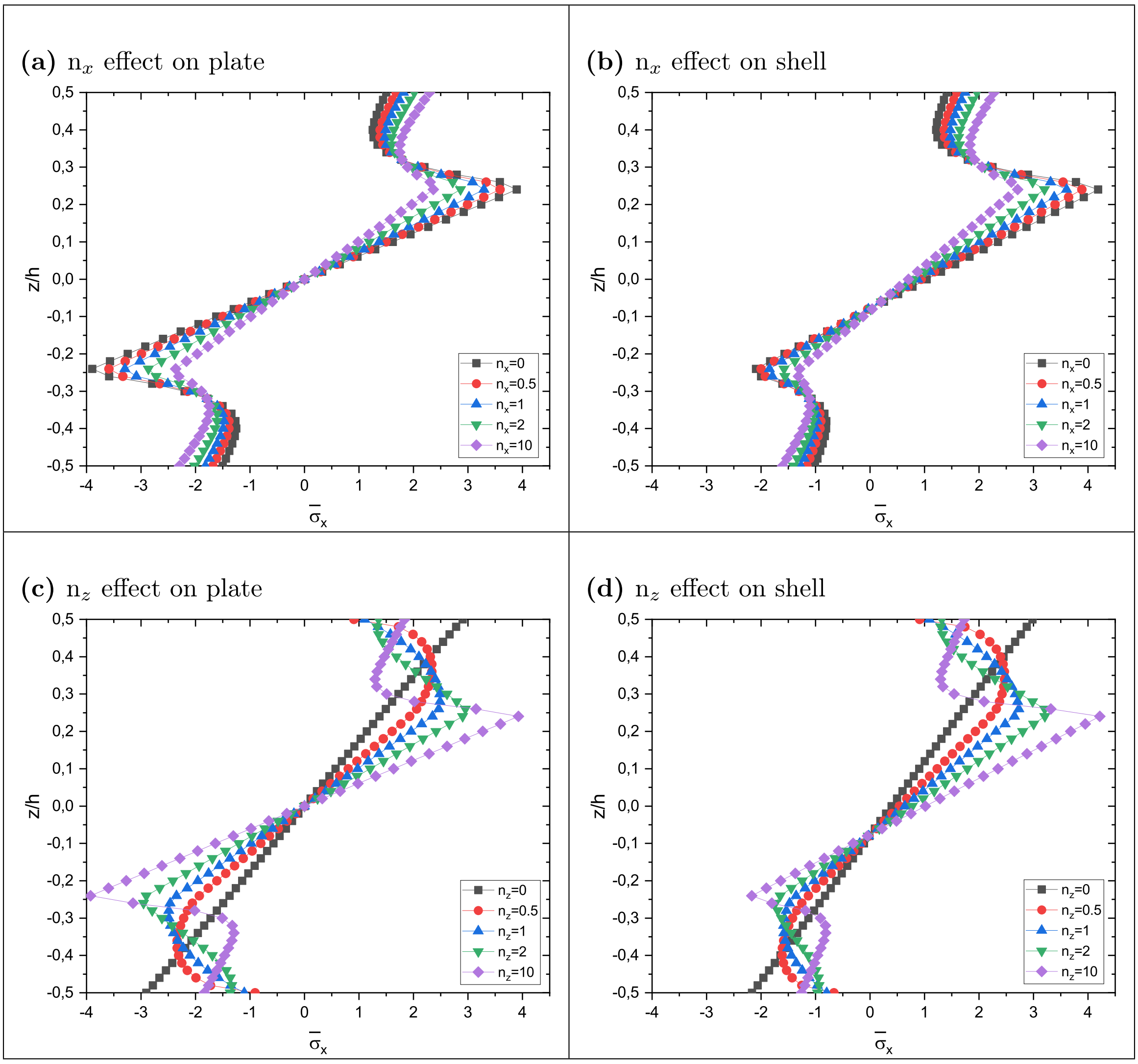

Figure 3.2: The effect of gradient indexes on non-dimensional normal stress $\overline{\sigma_x}$ on a sandwich (1−2−1) type D SSSS plate versus a spherical shell panel,h/a=0.1. (a) R$_x$/a=R$_y$/b=∞,n$_z$=5. (b) n$_z$=5,R$_x$/a=R$_y$/b=5. (c) n$_x$=0.5,R$_x$/a=R$_y$/b=∞. (d) n$_x$=0.5, R$_x$/a=R$_y$/b=5

3.3.2.4 Sandwich-Layups effect on Axial Stress distribution

The influence of the sandwich layup ratio on the non-dimensional normal stress distribution is shown in Figures 3.3. For flat plate configurations, the stress distribution exhibits symmetry across the thickness in most cases, with the exception of the $2-2-1$ and $2-1-1$ sandwich configurations. In these particular cases, the symmetry is disrupted due to the uneven distribution of material properties across the layers, which alters the stress behavior.

In contrast, for spherical shell panels, a distinct lack of symmetry in the stress distribution is observed across all sandwich configurations, regardless of the specific layup. The stress distribution consistently shows a higher concentration of stress in the upper layer compared to the lower layer, a pattern that is not dependent on the sandwich composition. This asymmetry in the spherical shell panels can be attributed to the curvature of the shell. The curvature induces additional bending moments and in-plane forces, which cause the upper layers to experience higher tensile or compressive stresses, while the lower layers are subjected to reduced stress magnitudes.

The consistent observation of higher stress in the upper layers of the spherical shells, as opposed to the more balanced stress distribution seen in the flat plates, emphasizes the critical role of curvature in stress behavior. This finding highlights the necessity of accounting for curvature effects when analyzing functionally graded materials (FGM) in shell structures, particularly in the design of sandwich composites where stress concentration could impact structural integrity.

Ultimately, the results underscore the importance of both sandwich layup ratio and shell geometry in determining stress distribution, with spherical shells requiring more careful consideration of their inherent asymmetry compared to flat plates.

3.3.2.5 Geometry and Mixture Composition effect on Axial stress distribution

Figure 3.4.a provides a comparative analysis of the normal stress distribution across various shell geometries. The results reveal a consistent pattern of stress variation through the thickness, with both the flat plate and hyperbolic shell geometries exhibiting a symmetrical stress distribution. This symmetry suggests that these geometries experience uniform stress behavior across their layers, maintaining balance between the top and bottom surfaces. In contrast, the other geometries, such as spherical or cylindrical shells, display an asymmetrical stress distribution, indicating that their curvature leads to uneven stress magnitudes across the thickness.

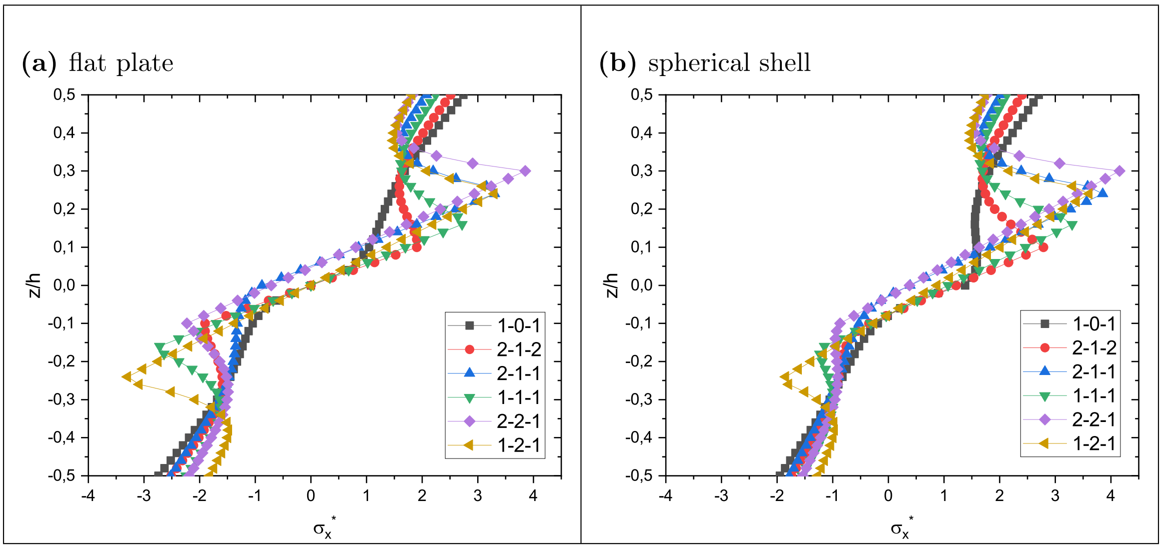

Figure 3.3: The effect of sandwich plate/shell thickness composition on non-dimensional normal stress $\overline{\sigma_x}$ type D SSSS,h/a=0.1. (a) $R_x/a=R_y/b=\infty, n_x=1, n_z=5$. (b) $R_x/a=R_y/b=5, n_x=1, n_z=5$

A noteworthy observation is the similarity in stress values at the top layer across all five geometries, despite differences in overall stress distribution patterns. This indicates that, although curvature impacts the distribution within the structure, the stress behavior at the outermost surface remains relatively consistent across different shell shapes. Such a finding suggests that the outermost layer may be a critical region for structural integrity across various geometries.

In Figure 3.4.b, the stress distribution across four different material mixtures is compared. For three of the mixtures—A, B, and D—the results reveal a similar pattern: a linear variation of stress in the core layer, accompanied by a nonlinear variation in the face sheets. This combination reflects a balanced gradation of material properties in these configurations, leading to predictable stress behavior. However, mixture C presents a different stress profile, which can be attributed to its bi-directional functionally graded material (FGM) core layer. The unique material distribution in mixture C causes the stress variation to deviate from the linear and nonlinear trends observed in the other cases.

Types A and B, despite differing slightly in composition, show nearly identical stress distribution curves. The only noticeable difference occurs in layer 1, where the volume fractions of ceramic materials 1 and 2 are reversed between the two types. This reversal explains the minor variation in stress observed at the bottom of the graph. The small difference highlights how subtle changes in material composition can impact the stress distribution, particularly in layers that are more sensitive to material gradation.

These observations collectively emphasize the importance of both geometry and material composition in determining stress behavior. While curvature introduces asymmetry in certain shell geometries, material gradation—especially in bi-directional FGMs—can further influence the complexity of stress variation across the structure.

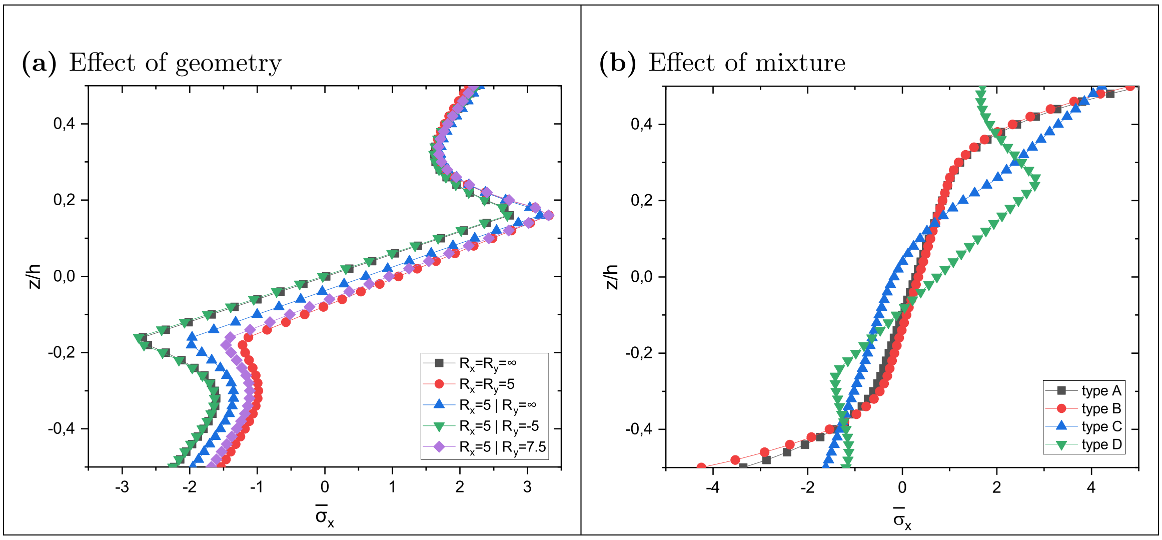

Figure 3.4: The effect of shell geometry and mixture type on non-dimensional normal stress $\overline{\sigma_x}$ disbtribution for SSSS shell panel,h/a=0.1. (a) type D 1−1−1 with n$_x$=1,n$_z$=5. (b) 1−2−1,n$_x$=n$_z$=2,R$_x$/a=R$_y$/b=5

3.3.2.6 Boundary conditions Effect on non-dimensional Deflection

Figure 3.5 illustrates the effect of various boundary conditions on the non-dimensional deflection of a bi-directional functionally graded material (FGM) sandwich plate. The boundary conditions considered include simply supported on all edges (SSSS), clamped on two opposite edges and simply supported on the other two (CSCS), clamped on two adjacent edges and simply supported on the remaining (CCSS), and clamped on all edges (CCCC). The x-axis represents the normalized position along the plate x/a, while the y-axis shows the non-dimensional deflection $\overline{w}$, highlighting the structural response across different configurations.

The results indicate that boundary conditions significantly influence the deflection behavior of the sandwich plate. The curve corresponding to the SSSS condition exhibits the largest deflection, with a peak value around $\overline{w} \approx 0.54$ at the center of the plate. This can be attributed to the simply supported edges, which allow for greater movement and deformation under loading. Conversely, the CCCC case, where all edges are clamped, results in the lowest deflection across the plate, showcasing the increased stiffness provided by clamped boundaries. The CSCS and CCSS conditions, which feature a combination of clamped and simply supported edges, produce intermediate deflections between the fully clamped and fully simply supported cases, reflecting the partial restriction of movement along the edges.

In addition to the boundary conditions, the bi-directional functionally graded material (FGM) plays a critical role in influencing the deflection profile. The material's gradient indexes n_x and n_z, which govern the variation of material properties along the length and thickness, cause a noticeable shift in the location and magnitude of the maximum deflection. For example, the peak deflection for the SSSS boundary condition occurs slightly closer to the plate's center ($x/a = 0.5$), while for the CCCC case, it is more uniformly distributed, indicating a stiffer response due to both the clamped edges and the material gradation. The gradient indexes in the FGM modify the stiffness of the plate in different regions, influencing how the deflection behaves under the same boundary conditions.

These observations underline the combined importance of boundary conditions and material gradation in determining the mechanical behavior of sandwich plates. Clamped edges increase stiffness, reducing deflection and enhancing structural integrity, while simply supported edges allow for greater flexibility and deformation. The bi-directional functionally graded material further adds complexity by shifting the deflection maxima based on the gradient indexes, making it a key factor in the design of structures where deflection control is crucial. This interplay of boundary conditions and material properties must be carefully considered in applications such as aerospace and civil engineering, where optimal performance is essential.

3.3.2.7 Porosity Effect on non-dimensional Deflection

The figure illustrates the effect of varying porosity values on the non-dimensional deflection of a fully simply supported (SSSS) functionally graded material (FGM) sandwich plate. The horizontal axis represents the normalized distance along the plate, x/a, while the vertical axis shows the non-dimensional deflection, $\bar{w}$. Different curves correspond to varying porosity values (ξ) ranging from 0 to 0.3, with porosity increasing from the bottom to the top curve. As the porosity increases, the maximum deflection also increases, indicating that a more porous material leads to higher flexibility in the plate. This behavior is expected since higher porosity introduces voids within the material, reducing stiffness and allowing greater deflection under load.

All porosity levels exhibit a symmetric deflection profile, with the maximum deflection occurring at the center of the plate ($x/a = 0.5$). The peak deflection increases slightly as

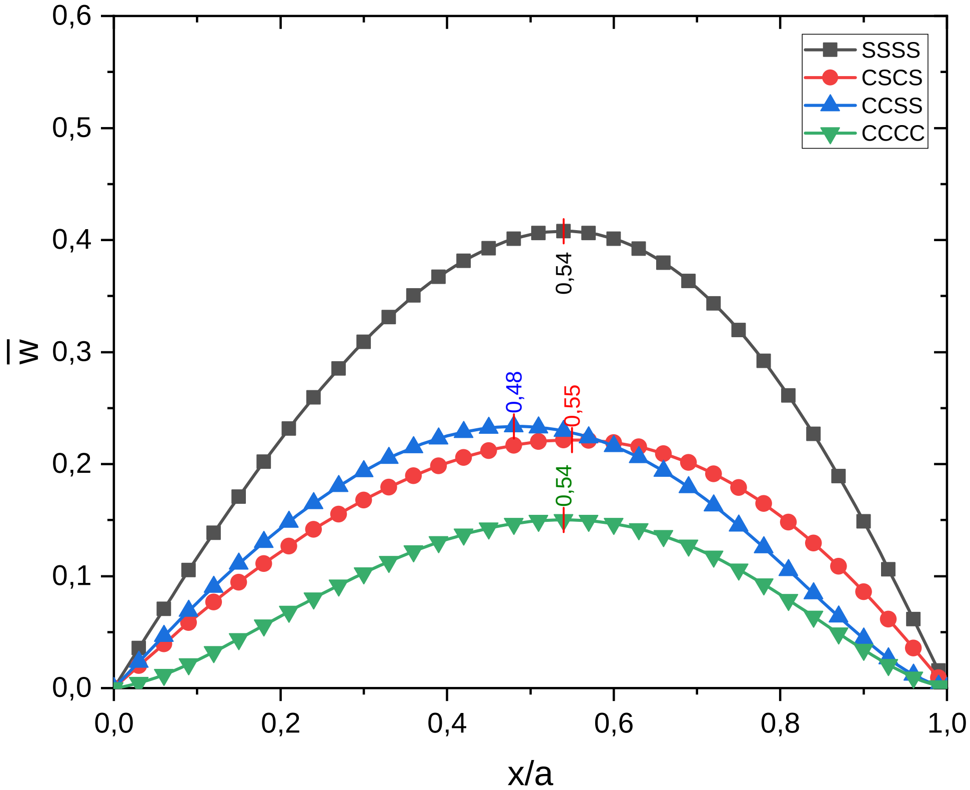

Figure 3.5: Effect of boundary conditions on non-dimensional deflection for a porous (typeI) sandwich plate <mixture type=A> (1–1–1) $n_z = n_x = 2, \xi = 0.1; y/b = 0.5$

porosity increases. For $\xi = 0$, the maximum deflection is approximately $\bar{w} = 0.54$, while for $\xi = 0.3$, it reaches about $\bar{w} = 0.57$, showing a gradual upward shift in deflection. The quantitative difference in deflection highlights the softening effect that porosity has on the structure.

From a structural perspective, the figure demonstrates the balance between stiffness and flexibility in FGM plates. Increasing porosity enhances flexibility but reduces stiffness, which could affect the load-bearing capacity of the structure. This trade-off is crucial when designing FGM structures, particularly when stiffness needs to be preserved while allowing for controlled flexibility. Overall, the figure effectively showcases the significant role of porosity in influencing the mechanical behavior of FGM plates.

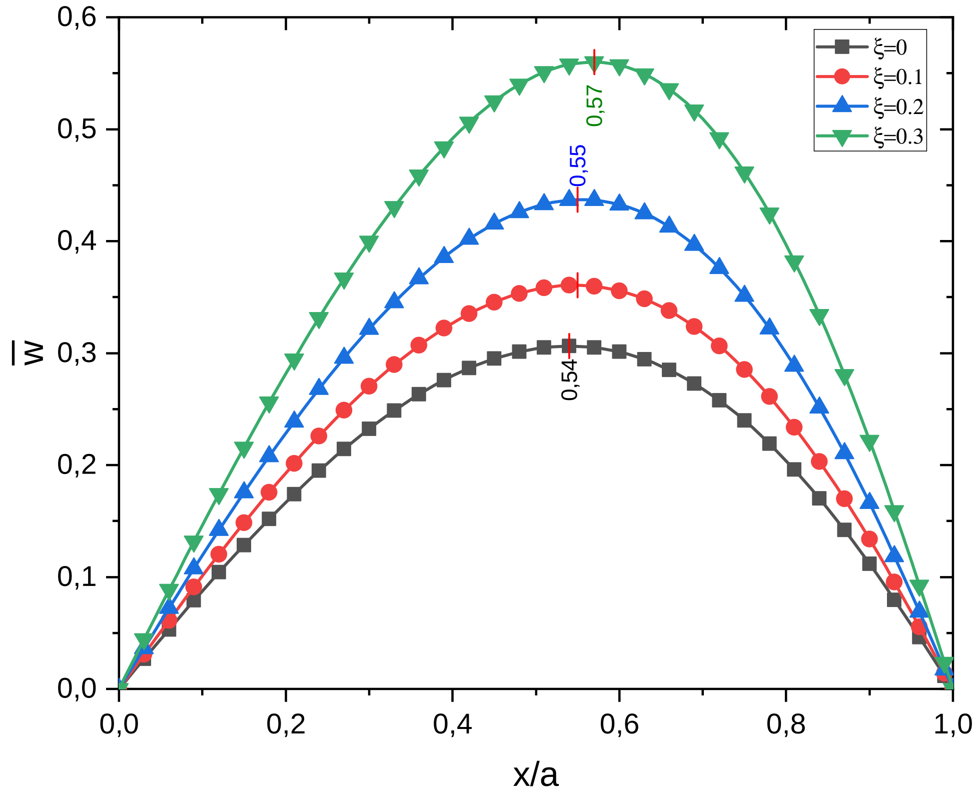

Figure 3.6: Effect of porosity value on non-dimensional deflection of an FGM sandwich plate $n_x = n_z = 2$ sandwich type $1-0-1$ FGM type=A;porosity type=typeI

3.4 Optimization Remarks

In the context of static bending analysis for FGMs, the goal of optimizing the material's gradient indexes n_x and n_z is to achieve a balance between stiffness and flexibility in the structure. By carefully adjusting these indexes, we can control the deflection of the shell panel under loading conditions, which directly impacts its mechanical performance.

3.4.1 Optimizing Gradient indexes

- While higher deflections may be undesirable for certain load-bearing applications, optimizing the gradient indexes could be beneficial for designs that require enhanced flexibility or controlled deformation.
- For structures that must maintain high stiffness with minimal deflection, lower gradient index values might be preferable.
- In applications where a higher degree of deflection is acceptable or required, increasing the gradient indexes can be an effective strategy to allow for more bending without compromising structural integrity.

The optimization of these parameters should therefore be guided by the specific performance requirements of the shell panels in their intended application, balancing the need for stiffness and deflection accordingly.

3.5 Conclusion

In this chapter, a detailed examination of the results from the static bending analysis of various functionally graded (FG) shell panel geometries was presented. The investigation covered multiple geometries, including spherical, cylindrical, hyperbolic, and elliptical configurations, under mechanical loads. The flexural behavior of these panels was studied in conjunction with four different sandwich compositions, providing a broad view of how geometry and material gradation influence structural performance.

The static bending responses were analyzed based on the mathematical model outlined in the previous chapter, which utilizes the Higher-order Shear Deformation Theory (TSDT) and Voigt micromechanical model for property estimation. The combination of these models enabled an accurate representation of the bending behavior for FG shells under mechanical loading.

Key findings from this analysis include:

- **The effect of sandwich layup configurations:** Different layer arrangements significantly influenced the stress distribution across the thickness of the shell panels, highlighting the importance of layer sequencing in achieving optimal structural behavior.

- **The impact of shell geometry:** The curvature and shape of the shell panels played a substantial role in determining the deflection and stress patterns. Notably, geometries with higher curvature, such as spherical and hyperbolic shells, exhibited different bending behaviors compared to flatter geometries.

- **The role of gradient index values:** The gradient index values were shown to have a direct correlation with deflection and stress distribution, allowing for control over structural performance. This underscores the potential for optimizing FG materials in sandwich structures by adjusting these parameters.

The results presented in this chapter provide a comprehensive understanding of how material composition, sandwich layer configuration, and geometry affect the static bending behavior of FG shell panels. These insights form a crucial foundation for the ongoing exploration of more advanced topics, such as nonlinear and dynamic analysis, in the broader context of functionally graded materials.

Chapter 4

Free vibration analysis of Bi-directional functionally graded material

4.1 Introduction

Free vibration analysis plays a crucial role in structural engineering, providing insights into the dynamic behavior of structures without external forces or excitations. By examining the natural frequencies and mode shapes of a structure, engineers can glean valuable information essential for design optimization, structural stability assessment, and failure prevention. One key aspect of free vibration analysis is its ability to predict resonance phenomena. Resonance occurs when the frequency of an external force matches one of the natural frequencies of the structure, leading to amplified vibrations and potential structural failure. Understanding these resonant frequencies is vital for designing structures that can withstand dynamic loads without experiencing detrimental effects. Furthermore, free vibration analysis helps engineers assess the stability of a structure under various loading conditions. By examining mode shapes associated with different natural frequencies, engineers can identify potential areas of stress concentration, deformation, or instability. This information is crucial for optimizing designs and ensuring structural safety. Moreover, free vibration analysis aids in design optimization by identifying critical parameters such as material properties, geometric configurations, and boundary conditions that influence the dynamic response of the system. Engineers can use this knowledge to refine designs, minimize unwanted vibrations, and enhance performance while minimizing weight and cost. Additionally, understanding the natural frequencies and mode shapes of a structure enables engineers to predict its dynamic response to external forces, such as wind, earthquakes, or machinery operation. This knowledge is essential for assessing structural integrity, comfort, and safety in buildings, bridges, vehicles, and other engineering systems subjected to dynamic loads. In summary, free vibration analysis is a fundamental tool in structural engineering, providing essential insights into the dynamic behavior of structures and enabling engineers to design safe, reliable, and efficient systems for a wide range of applications.

4.2 Solution Methodology

In this section, the four mixtures of Functionally Graded Materials (FGM) are revisited for free vibration analysis. The equilibrium equation governing the vibrational behavior of the FGM shell panel under various conditions is derived using the variational principle, as detailed in Equation (2.47). Throughout this analysis, the primary focus is on obtaining the first mode of the fundamental frequency across all discussed cases, unless otherwise specified. To achieve this, a custom-made computer code developed in the FORTRAN environment is employed to compute the desired frequency responses. The mechanical properties of the FGM constituents, outlined in Table 3.1, are utilized for computational purposes. The analysis explores the effects of different conditions on the structural frequencies, with comprehensive discussions provided throughout the study.

4.3 Results & Discussion

Frequency responses are computed using a custom-made computer code developed in FORTRAN, tailored to the linear mathematical formulation. The convergence behavior of the numerical model is evaluated and juxtaposed with findings from existing literature. Subsequently, the linear model is validated by comparing its responses with previously published results. To demonstrate the robustness and applicability of the model, a diverse array of numerical examples is solved, encompassing various geometrical and material parameters and support conditions. For consistency, a non-dimensional frequency parameter formulation is adopted in the following format: $\overline{\omega} = \frac{\omega}{h}\sqrt{\frac{\rho_0}{E_0}}$, Where ρ_0=1Kg/m^3,and E$_0$=1Gpa. Detailed discussions on the influence of different parameters on the linear vibration responses of the FG shell panel under varying conditions are provided.

4.3.1 Validation Study

The assumptions used to generate the data in Table 4.1 are explained in the caption. The convergence study shows that as the polynomial degree (P) increases, the natural frequencies for all modes stabilize, particularly from $P = 6$ onward, demonstrating the adequacy of higher-order approximations. For the gradient index (n_z), increasing its value from 0 to 10 results in a noticeable reduction in natural frequencies across all modes, highlighting the softening effect of material gradation on the shell's stiffness. Higher modes exhibit larger natural frequencies, which aligns with expected vibrational behavior. Additionally, the computed results closely match those reported in HSDT-based studies ([96] and [97]), validating the accuracy of the method in capturing the vibrational characteristics of the functionally graded cylindrical shell panel. Consequently, a value of $P = 7$ is used for generating results throughout the remainder of the thesis, except for contour plots, where $P = 5$ is employed to speed-up the data generation process.

Table 4.1: Convergence study of the first four natural frequencies $\breve{\omega} = \omega \times a^2 \sqrt{\frac{12\times\rho_m\times(1-\nu_m^2)}{(E_m\times h^2)}}$ for clamped Si_3N_4/SUS304 square uni-directional FGM cylindrical shell panel;a/h=10;a/R_x=0.1;R_y=∞;n_x=0

Gradient n_z	**P Degree**	Mode Number 1	2	3	4
0	2	215.720	290.494	290.494	1542.420
	3	130.374	285.504	286.002	299.975
	4	74.499	211.963	212.148	282.333
	5	74.383	143.261	143.421	200.680
	6	74.320	142.419	142.587	199.960
	7	74.287	141.801	141.970	199.396
	8	74.271	141.729	141.898	199.269
	9	74.259	141.695	141.864	199.209
	HSDT [96]	72.961	138.555	138.555	195.537
	HSDT [97]	74.518	144.663	145.740	206.992
0.2	2	175.498	237.422	237.611	1255.041
	3	106.016	232.220	233.092	244.505
	4	60.602	172.081	172.351	230.715
	5	60.509	116.448	116.606	163.073
	6	60.457	115.766	115.931	162.492
	7	60.432	115.257	115.422	162.022
	8	60.419	115.200	115.365	161.923
	9	60.409	115.173	115.338	161.875

Continued on next page

Gradient	P	Mode Number			
nz	**Degree**	1	2	3	4
	HSDT [96]	60.027	113.881	114.027	160.624
	HSDT [97]	57.479	111.717	112.531	159.855
2.0	2	114.022	156.843	157.021	843.473
	3	69.318	152.393	153.200	159.655
	4	40.607	112.757	112.957	152.150
	5	40.532	77.716	77.817	108.645
	6	40.496	77.231	77.337	108.204
	7	40.475	76.923	77.027	107.917
	8	40.465	76.878	76.983	107.837
	9	40.458	76.859	76.963	107.803
	HSDT [96]	39.146	74.292	74.387	104.769
	HSDT [97]	40.750	78.817	79.407	112.457
10.0	2	96.257	134.168	134.232	695.338
	3	58.856	130.653	131.394	134.460
	4	35.179	96.083	96.202	129.870
	5	35.110	67.174	67.250	93.792
	6	35.079	66.748	66.827	93.396
	7	35.059	66.496	66.575	93.160
	8	35.051	66.456	66.535	93.086
	9	35.044	66.438	66.517	93.056
	HSDT [96]	33.367	63.287	63.367	89.197
	HSDT [97]	35.852	69.075	69.609	98.386

In the second example, the aim is to demonstrate the versatility of the algorithm by conducting a comparative study of non-dimensional frequencies for various types of shells and different theories. The results of this study are presented in Table 4.2, where the power-law index variation (n_z, n_x= 0) is explored. The functionally graded material (FGM) utilized in this analysis consists of a mixture of Al/Al_2O_3. The shell is simply supported at all four edges, with a length to thickness ratio of a/h = 5. It's worth noting that a single layer is employed in this example, with the FGM material characterized by a ceramic volume fraction expressed as $V_c = (\frac{2z+h}{2h})^{n_z}$. Remarkably, the results align closely with those reported by [98] utilizing different theories, underscoring the accuracy and reliability of the approach.

Table 4.2: comparison study of the fundamental frequency $\varpi = \omega\ h\ \sqrt{\frac{\rho_c}{E_c}}$ for doubly curved shell with different theories ($n_x = 0$)

R_x/a	R_y/b	Model	n_z				
			0	1	5	10	∞
5	∞	Present	0.21143	0.16284	0.13508	0.12956	0.10811
		PSDT [98]	0.21186	0.16352	0.13736	0.13019	0.10802
		TSDT [98]	0.21182	0.16354	0.13589	0.13016	0.10800
		HSDT [98]	0.21199	0.16352	0.13600	0.13019	0.10809
		ESDT [98]	0.21222	0.16360	0.13584	0.13019	0.09108
		FSDT [98]	0.21482	0.16546	0.14013	0.13458	0.10953
		CST [98]	0.23192	0.17643	0.15119	0.14666	0.09954
5	5	Present	0.21391	0.16459	0.13612	0.13054	0.10936
		PSDT [98]	0.21452	0.16558	0.13871	0.13143	0.10938
		TSDT [98]	0.21449	0.16561	0.13728	0.13140	0.10936
		HSDT [98]	0.21465	0.16558	0.13738	0.13143	0.10944
		ESDT [98]	0.21488	0.16566	0.13723	0.13143	0.09222
		FSDT [98]	0.21744	0.16748	0.14142	0.13574	0.11086
		CST [98]	0.23431	0.17821	0.15224	0.14759	0.10056
5	-5	Present	0.20931	0.16159	0.13428	0.12870	0.10703
		PSDT [98]	0.21036	0.16256	0.13675	0.12957	0.10726
		TSDT [98]	0.21033	0.16259	0.13526	0.13954	0.10724
		HSDT [98]	0.21050	0.16256	0.13537	0.12957	0.10732
		ESDT [98]	0.21073	0.16265	0.13522	0.12957	0.09044
		FSDT [98]	0.21333	0.16452	0.13955	0.13400	0.10877
		CST [98]	0.23046	0.17558	0.15072	0.14616	0.09891
5	7.5	Present	0.21305	0.16395	0.13575	0.13020	0.10893
		PSDT [98]	0.21351	0.16478	0.13818	0.13095	0.10886
		TSDT [98]	0.21347	0.16480	0.13673	0.13092	0.10884
		HSDT [98]	0.21364	0.16478	0.13684	0.13095	0.10893
		ESDT [98]	0.21387	0.16486	0.13669	0.13095	0.09179
		FSDT [98]	0.21644	0.16669	0.14091	0.13530	0.11036
		CST [98]	0.23342	0.17752	0.15183	0.14723	0.10018

In the upcoming example (table 4.3), the goal is to ensure that the bi-directionality in terms of FGM is well formulated in the code. To achieve this, a comparative study with results reported by Vinh [88] has been conducted for a flat shell panel. The plate is assumed to be simply supported, and the four FGM mixtures have been included. Very similar results have been demonstrated, highlighting the accuracy of the formulation in capturing the frequency of the bi-directional flat panel.

Table 4.3: Dimensionless Frequency $\bar{\omega}$ parameter for SSSS bi-directional functionally graded sandwich shell

Mixture	**n$_x$**	**n$_z$**	**Source**	1−0−1	2−1−2	2−1−1	1−1−1	2−2−1	1−2−1
A	0	1	Present	1.72394	1.68028	1.63089	1.63562	1.57474	1.55824
			TSDT [88]	1.72752	1.68556	1.63651	1.64135	1.58055	1.56262
	1	1	Present	1.49556	1.46164	1.42574	1.42809	1.38413	1.36970
			TSDT [88]	1.49807	1.46481	1.42910	1.43129	1.38738	1.37218
	5	1	Present	1.30861	1.28293	1.25861	1.25840	1.22877	1.21620
			TSDT [88]	1.31063	1.28515	1.26091	1.26055	1.23093	1.21801
B	0	1	Present	1.42399	1.39784	1.38105	1.37254	1.34251	1.32746
			TSDT [88]	1.42697	1.40118	1.38365	1.37572	1.34486	1.32982
	1	1	Present	1.48766	1.45473	1.42051	1.42248	1.38017	1.36623
			TSDT [88]	1.49048	1.45811	1.42395	1.42578	1.38342	1.36871
	5	1	Present	1.45130	1.42226	1.38345	1.39399	1.35184	1.34411
			TSDT [88]	1.45428	1.42568	1.38719	1.39728	1.35541	1.34659
C	0	1	Present	0.16013	0.17422	0.18660	0.18813	0.20543	0.21358
			TSDT [88]	0.15975	0.17346	0.18567	0.18717	0.20431	0.21277
	1	1	Present	0.22588	0.24182	0.25575	0.25727	0.27618	0.28538
			TSDT [88]	0.22553	0.24122	0.25502	0.25659	0.27539	0.28486
	5	1	Present	0.31519	0.33180	0.34583	0.34764	0.36613	0.37605
			TSDT [88]	0.31479	0.33126	0.34521	0.34709	0.36551	0.37561
D	0	1	Present	1.24363	1.30069	1.33396	1.35405	1.39642	1.44200
			TSDT [88]	1.24447	1.30143	1.33474	1.35468	1.39705	1.44076
	1	1	Present	1.14550	1.18812	1.21396	1.22800	1.26067	1.29291
			TSDT [88]	1.14651	1.18907	1.21496	1.22889	1.26156	1.29375
	5	1	Present	1.07035	1.10043	1.11937	1.12848	1.15223	1.17442
			TSDT [88]	1.07158	1.10166	1.12064	1.12969	1.15347	1.17564

4.3.2 Parametric Study

4.3.2.1 Gradient indexes effects on non-dimensional frequency

In this section, a comprehensive vibration analysis is performed for various shell geometries, including spherical, cylindrical, and hyperbolic shapes. The study focuses on the influence of gradient indexes n_x and n_z, along with the effects of porosity and other relevant parameters on the vibrational behavior of these structures. Tables 4.4 to 4.7 present the non-dimensional frequencies for each shell geometry across four different material mixtures (A, B, C, and D). These results provide a detailed insight into the vibrational characteristics of the functionally graded shell panels.

The observed trends in frequency variation are consistent with previous studies, such as those by [88], where similar behaviors were reported for flat plate configurations. Specifically, for material types A and B, an increase in either gradient index n_x or n_z results in a decrease in the non-dimensional frequency parameter, regardless of the shell geometry being analyzed (spherical, cylindrical, or hyperbolic paraboloidal shell). This consistent pattern across different geometries highlights the significant role of gradient indexes in controlling the vibrational properties of functionally graded shells.

In the case of material type C, a unique behavior is observed where the non-dimensional frequency remains constant for varying values of n_z in the $1-0-1$ sandwich configuration. However, when n_x is increased, the frequency decreases, aligning with the trends seen in types A and B. This indicates that while n_z may have little to no effect in certain configurations, n_x plays a crucial role in influencing vibrational characteristics.

Moreover, in other thickness scenarios examined for type C, similar trends to those of types A and B are observed, but the rate of frequency variation with respect to the gradient indexes is noticeably slower. This suggests that the thickness ratio and gradient index interplay in a complex manner, impacting the vibrational response in a way that is dependent on both material distribution and shell geometry.

In summary, the results presented in these tables underscore the intricate relationship between gradient indexes, and material composition on the vibrational behavior of functionally graded shell panels. These findings further emphasize the importance of carefully selecting gradient index values and material compositions to optimize the vibrational performance of shell structures under different operating conditions.

Table 4.4: Frequency parameter $\bar{\omega}$ for SSSS bi-directional FGM shell panel type A

R_x/a	R_y/b	n_x	n_z	1−0−1	2−1−2	2−1−1	1−1−1	2−2−1	1−2−1
5	5	0	0	1.92158	1.93548	1.90100	1.92052	1.86497	1.85718
			1	1.79376	1.74383	1.69774	1.69515	1.63713	1.61285
			5	1.47459	1.41586	1.38449	1.36963	1.33225	1.30135
		1	0	1.67195	1.67471	1.64633	1.65967	1.61565	1.61061
			1	1.55637	1.51814	1.48369	1.48189	1.43909	1.42040
			5	1.31662	1.27402	1.25271	1.24085	1.21542	1.19262
		5	0	1.46936	1.46352	1.44372	1.44848	1.41882	1.40959
			1	1.36788	1.33865	1.31839	1.31193	1.28637	1.26729
			5	1.19397	1.16479	1.15449	1.14244	1.12912	1.11055
5	∞	0	0	1.84545	1.86884	1.83417	1.85986	1.80405	1.80352
			1	1.73803	1.69283	1.64521	1.64723	1.58805	1.56875
			5	1.43352	1.37621	1.34352	1.33082	1.29244	1.26341
		1	0	1.60916	1.61889	1.59063	1.60819	1.56434	1.56409
			1	1.50804	1.47304	1.43789	1.43883	1.39558	1.37973
			5	1.27748	1.23563	1.21368	1.20287	1.17693	1.15500
		5	0	1.41020	1.41025	1.38977	1.39890	1.36822	1.36424
			1	1.32101	1.29445	1.27227	1.26939	1.24199	1.22664
			5	1.15448	1.12586	1.11383	1.10382	1.08899	1.07221
5	-5	0	0	1.80921	1.83570	1.80037	1.82878	1.77205	1.77509
			1	1.70930	1.66593	1.61700	1.62162	1.56129	1.54486
			5	1.41144	1.35494	1.32129	1.31010	1.27100	1.24338
		1	0	1.57858	1.59069	1.56227	1.58154	1.53750	1.53939
			1	1.48307	1.44937	1.41378	1.41605	1.37247	1.35811
			5	1.25698	1.21563	1.19331	1.18320	1.15700	1.13573
		5	0	1.38196	1.38407	1.36253	1.37407	1.34184	1.34107
			1	1.29757	1.27208	1.24799	1.24774	1.21837	1.20589
			5	1.13455	1.10630	1.09258	1.08449	1.06817	1.05316
5	7.5	0	0	1.89207	1.90978	1.87529	1.89721	1.84165	1.83665
			1	1.77236	1.72431	1.67769	1.67683	1.61844	1.59603
			5	1.45891	1.40071	1.36887	1.35480	1.31706	1.28683

Continued on next page

R_x/a	R_y/b	n_x	n_z	1−0−1	2−1−2	2−1−1	1−1−1	2−2−1	1−2−1
		1	0	1.64769	1.65324	1.62492	1.63992	1.59599	1.59282
			1	1.53782	1.50086	1.46616	1.46541	1.42245	1.40485
			5	1.30162	1.25930	1.23775	1.22628	1.20065	1.17816
		5	0	1.44644	1.44295	1.42297	1.42938	1.39944	1.39216
			1	1.34982	1.32164	1.30075	1.29557	1.26942	1.25167
			5	1.17876	1.14979	1.13893	1.12756	1.11374	1.09576

Table 4.5: Frequency parameter $\bar{\omega}$ for SSSS bi-directional functionally graded sandwich shell type B

R_x/a	R_y/b	n_x	n_z	1−0−1	2−1−2	2−1−1	1−1−1	2−2−1	1−2−1
5	5	0	0	1.58743	1.57859	1.58246	1.56488	1.55666	1.52768
			1	1.48634	1.45464	1.43360	1.42593	1.39856	1.37707
			5	1.29031	1.25398	1.21800	1.22511	1.18340	1.18215
		1	0	1.66877	1.66792	1.63769	1.65221	1.60685	1.60410
			1	1.55219	1.51411	1.47925	1.47859	1.43582	1.41852
			5	1.31624	1.27411	1.25275	1.24119	1.21572	1.19314
		5	0	1.59544	1.59189	1.55516	1.57964	1.52626	1.54140
			1	1.49594	1.46369	1.43102	1.43373	1.39702	1.38238
			5	1.29176	1.25417	1.24726	1.22447	1.21484	1.18061
5	∞	0	0	1.51786	1.51760	1.52990	1.50953	1.50873	1.47898
			1	1.43557	1.40805	1.39072	1.38198	1.35173	1.33617
			5	1.25135	1.21590	1.18031	1.18748	1.14596	1.14490
		1	0	1.60029	1.60741	1.57993	1.59681	1.55380	1.55471
			1	1.50095	1.46676	1.43235	1.43372	1.39143	1.37661
			5	1.27640	1.23523	1.21341	1.20284	1.17702	1.15529
		5	0	1.53920	1.54314	1.50202	1.53522	1.47779	1.50164
			1	1.45398	1.42474	1.38841	1.39655	1.35680	1.34709
			5	1.25709	1.21981	1.21123	1.19015	1.17917	1.14610
5	-5	0	0	1.48729	1.49033	1.50501	1.48435	1.48533	1.45620
			1	1.41204	1.38606	1.36933	1.36094	1.33108	1.31620
			5	1.23212	1.19700	1.16123	1.16877	1.12708	1.12638

Continued on next page

R_x/a	R_y/b	n_x	n_z	1−0−1	2−1−2	2−1−1	1−1−1	2−2−1	1−2−1
		1	0	1.56801	1.57782	1.55249	1.56900	1.52761	1.52916
			1	1.47510	1.44240	1.40851	1.41038	1.36848	1.35459
			5	1.25566	1.21505	1.19301	1.18303	1.15704	1.13592
		5	0	1.52204	1.52797	1.48447	1.52079	1.46093	1.48765
			1	1.43924	1.41037	1.37198	1.38229	1.34058	1.33279
			5	1.24231	1.20481	1.19506	1.17494	1.16292	1.13051
5	7.5	0	0	1.56023	1.55477	1.56206	1.54329	1.53812	1.50874
			1	1.46658	1.43654	1.41705	1.40888	1.37684	1.36125
			5	1.27526	1.23928	1.20349	1.21059	1.16898	1.16778
		1	0	1.64221	1.64454	1.61528	1.63087	1.58637	1.58515
			1	1.53246	1.49592	1.46121	1.46138	1.41878	1.40247
			5	1.30097	1.25920	1.23766	1.22647	1.20086	1.17859
		5	0	1.57257	1.57207	1.53370	1.56164	1.50676	1.52540
			1	1.47906	1.44809	1.41405	1.41890	1.38107	1.36838
			5	1.27810	1.24066	1.23315	1.21101	1.20090	1.16711

Table 4.6: Frequency parameter $\bar{\omega}$ for SSSS bi-directional functionally graded sandwich shell type C

R_x/a	R_y/b	n_x	n_z	1−0−1	2−1−2	2−1−1	1−1−1	2−2−1	1−2−1
5	5	0	0	1.32100	1.37866	1.32100	1.43635	1.37866	1.52926
			1	1.32100	1.32917	1.29781	1.34326	1.31339	1.36928
			5	1.32100	1.30195	1.28767	1.29657	1.28707	1.29423
		1	0	1.24666	1.28004	1.24666	1.31642	1.28004	1.37884
			1	1.24666	1.25143	1.23421	1.25966	1.24190	1.27490
			5	1.24666	1.23683	1.22771	1.23410	1.22529	1.23183
		5	0	1.16784	1.18855	1.16784	1.21193	1.18855	1.25386
			1	1.16784	1.17045	1.15815	1.17498	1.16223	1.18342
			5	1.16784	1.16142	1.15175	1.15890	1.14840	1.15544
5	∞	0	0	1.24686	1.29936	1.24686	1.35532	1.29936	1.44776
			1	1.24686	1.25550	1.23411	1.27040	1.24798	1.29784
			5	1.24686	1.23292	1.23173	1.23151	1.23352	1.23442

Continued on next page

R_x/a	R_y/b	n_x	n_z	1−0−1	2−1−2	2−1−1	1−1−1	2−2−1	1−2−1
		1	0	1.18514	1.21465	1.18514	1.24960	1.21465	1.31153
			1	1.18514	1.19017	1.17981	1.19886	1.18624	1.21492
			5	1.18514	1.17888	1.17849	1.17883	1.17761	1.18002
		5	0	1.11956	1.13585	1.11956	1.15679	1.13585	1.19642
			1	1.11956	1.12219	1.11563	1.12675	1.11837	1.13521
			5	1.11956	1.11631	1.11292	1.11585	1.11040	1.11477
5	-5	0	0	1.21647	1.26642	1.21647	1.32120	1.26642	1.41267
			1	1.21647	1.22521	1.20787	1.24028	1.22090	1.26800
			5	1.21647	1.20468	1.20840	1.20481	1.21097	1.20963
		1	0	1.15749	1.18529	1.15749	1.21948	1.18529	1.28087
			1	1.15749	1.16260	1.15501	1.17140	1.16088	1.18767
			5	1.15749	1.15271	1.15572	1.15371	1.15540	1.15624
		5	0	1.10174	1.11556	1.10174	1.13485	1.11556	1.17254
			1	1.10174	1.10428	1.10025	1.10867	1.10225	1.11683
			5	1.10174	1.09997	1.09889	1.10034	1.09653	1.10006
5	7.5	0	0	1.29187	1.34755	1.29187	1.40461	1.34755	1.49738
			1	1.29187	1.30023	1.27276	1.31465	1.28768	1.34124
			5	1.29187	1.27481	1.26567	1.27098	1.26602	1.27070
		1	0	1.22271	1.25460	1.22271	1.29043	1.25460	1.35267
			1	1.22271	1.22759	1.21304	1.23600	1.22025	1.25157
			5	1.22271	1.21428	1.20858	1.21259	1.20677	1.21168
		5	0	1.14859	1.16764	1.14859	1.19014	1.16764	1.23126
			1	1.14859	1.15122	1.14114	1.15578	1.14472	1.16426
			5	1.14859	1.14339	1.13620	1.14167	1.13320	1.13916

Table 4.7: Frequency parameter $\bar{\omega}$ for SSSS bi-directional functionally graded sandwich shell type D

R_x/a	R_y/b	n_x	n_z	1−0−1	2−1−2	2−1−1	1−1−1	2−2−1	1−2−1
5	5	0	0	1.92158	1.92158	1.92158	1.92158	1.92158	1.92158
			1	1.34300	1.40525	1.43652	1.46020	1.50064	1.54627
			5	1.02516	1.08428	1.13116	1.15612	1.21851	1.28884

Continued on next page

R_x/a	R_y/b	n_x	n_z	1−0−1	2−1−2	2−1−1	1−1−1	2−2−1	1−2−1
		1	0	1.67195	1.67195	1.67195	1.67195	1.67195	1.67195
			1	1.22750	1.27379	1.29901	1.31489	1.34691	1.37989
			5	1.00889	1.04838	1.08553	1.09737	1.14542	1.19085
		5	0	1.46936	1.46936	1.46936	1.46936	1.46936	1.46936
			1	1.14444	1.17779	1.19350	1.20722	1.22820	1.25389
			5	0.99999	1.02765	1.04910	1.06032	1.08972	1.12310
5	∞	0	0	1.84545	1.84545	1.84545	1.84545	1.84545	1.84545
			1	1.26628	1.32449	1.35677	1.37807	1.41949	1.46389
			5	0.96384	1.00577	1.05305	1.07113	1.13425	1.20134
		1	0	1.60916	1.60916	1.60916	1.60916	1.60916	1.60916
			1	1.16416	1.20764	1.23321	1.24773	1.28012	1.31248
			5	0.95608	0.98455	1.02149	1.02902	1.07696	1.12032
		5	0	1.41020	1.41020	1.41020	1.41020	1.41020	1.41020
			1	1.08716	1.11804	1.13528	1.14638	1.16866	1.19240
			5	0.95182	0.97163	0.99528	1.00058	1.03185	1.06076
5	-5	0	0	1.80921	1.80921	1.80921	1.80921	1.80921	1.80921
			1	1.23284	1.28934	1.32229	1.34217	1.38413	1.24747
			5	0.93735	0.97287	1.02085	1.03559	1.09934	1.16432
		1	0	1.57858	1.57858	1.57858	1.57858	1.57858	1.57858
			1	1.13583	1.17806	1.20367	1.21759	1.24995	1.28190
			5	0.93263	0.95699	0.99373	0.99958	1.04723	1.08962
		5	0	1.38196	1.38196	1.38196	1.38196	1.38196	1.38196
			1	1.06138	1.09120	1.10997	1.11900	1.14254	1.16454
			5	0.93002	0.94694	0.97321	1.97438	1.00789	1.03330
5	7.5	0	0	1.89207	1.89207	1.89207	1.89207	1.89207	1.89207
			1	1.31305	1.37372	1.40535	1.42815	1.46895	1.51414
			5	1.00121	1.05360	1.10057	1.12292	1.18553	1.25465
		1	0	1.64769	1.64769	1.64769	1.64769	1.64769	1.64769
			1	1.20283	1.24802	1.27339	1.28874	1.32092	1.35366
			5	0.98830	1.02347	1.06054	1.07070	1.11872	1.16334
		5	0	1.44644	1.44644	1.44644	1.44644	1.44644	1.44644
			1	1.12213	1.15452	1.17073	1.18353	1.20493	1.22996

Continued on next page

R_x/a	R_y/b	n_x	n_z	1−0−1	2−1−2	2−1−1	1−1−1	2−2−1	1−2−1
			5	0.98124	1.00580	1.02792	1.03701	1.06698	1.09879

To provide a clearer understanding of how the gradient indexes n_x and n_z influence the frequency parameter, contour plots (4.1) have been generated for a simply supported (SSSS) sandwich spherical shell panel with a (1−1−1) thickness configuration. These plots offer a visual representation of the frequency variations across four different material mixtures (A, B, C, and D). The most pronounced changes in the frequency parameter occur within the range of $0 < (n_x, n_z) < 2$, where both indexes have a substantial impact. As either n_x or n_z exceeds this range, the rate of frequency variation slows considerably, suggesting that beyond certain values, the gradient indexes exert diminishing effects on the frequency parameter.

For mixtures A, C, and D, a notable trend emerges: the maximum frequency values are consistently observed when $n_x = n_z = 0$. This indicates that when the shell panel consists predominantly of ceramic material (ceramic 1), it exhibits higher vibrational frequencies. For instance, in mixture A, the shell panel is composed of ceramic face sheets and a metallic core, while mixture C features a metallic bottom layer, a ceramic 1 core, and a ceramic top face sheet. Mixture D, on the other hand, consists entirely of ceramic 1 throughout the shell. The predominance of ceramic material in these mixtures enhances the stiffness of the shell, resulting in higher frequency values. Conversely, as n_x and n_z increase towards infinity, the shell composition shifts towards a predominantly metallic structure, resulting in lower frequency values due to the reduced stiffness of the metallic material.

In contrast, mixture B exhibits a different frequency variation pattern, primarily influenced by the gradient index n_z. As shown in Table 4.5, the highest frequency values are observed when $n_z = 0$, and as this index increases, the frequency parameter progressively decreases. This behavior suggests that the material composition in mixture B—comprising different layers—leads to a significant sensitivity of the frequency parameter to changes in n_z. Interestingly, in this case, n_x has minimal influence on the frequency parameter, indicating that the variation in the frequency response is largely dominated by changes in the vertical material distribution, rather than the horizontal gradient.

In summary, the contour plots highlight the intricate relationship between the material gradient indexes and the vibrational behavior of functionally graded shell panels. While mixtures A, C, and D demonstrate similar trends where both gradient indexes significantly affect the frequency response, mixture B stands out due to its heightened sensitivity to n_z, revealing the nuanced influence of material distribution on the dynamic properties of functionally graded structures.

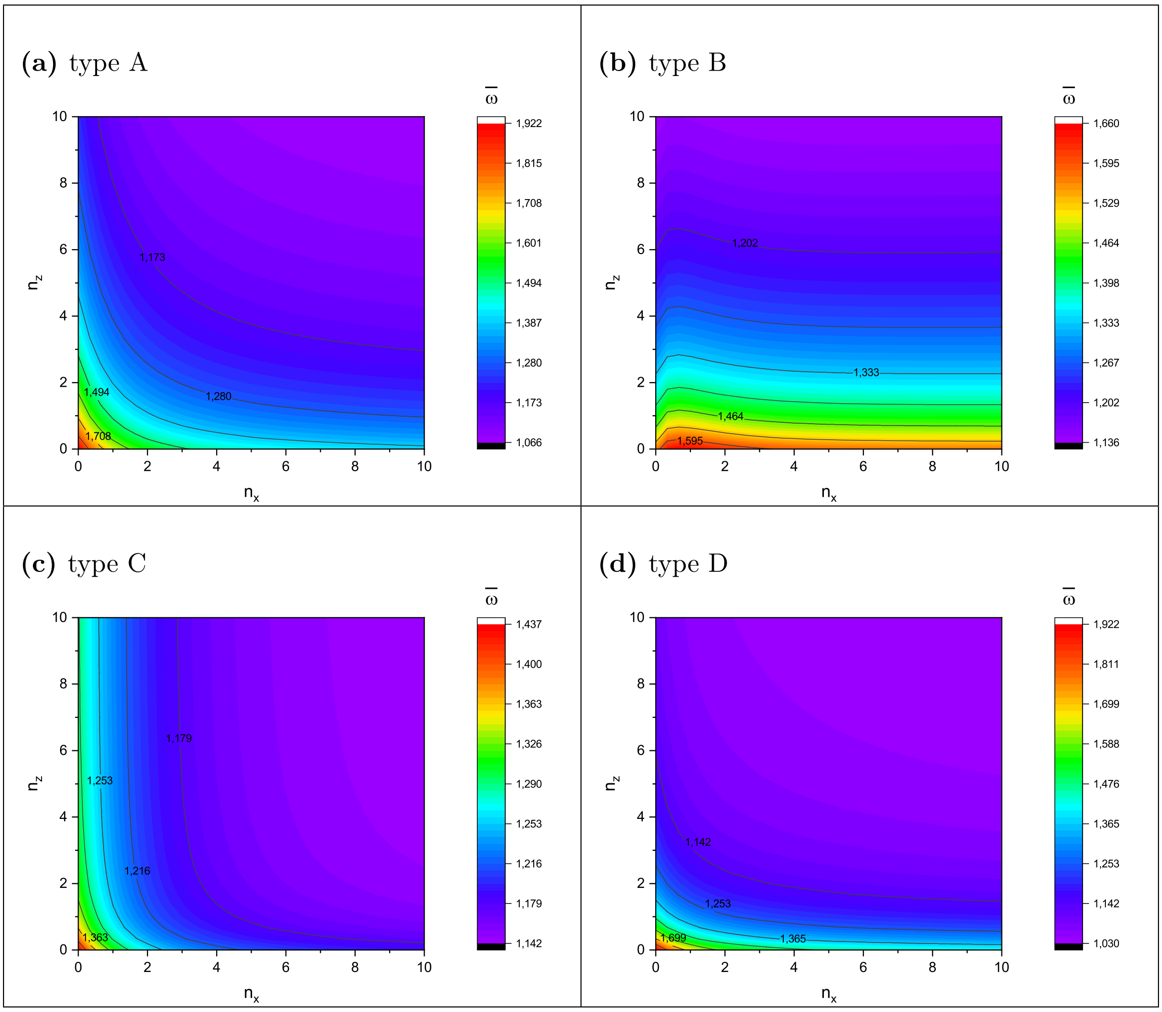

Figure 4.1: Effect of gradient index (n_x/n_z) on dimensionless frequency parameter for spherical Sandwich 1−1−1 shell panel,h/a=0.1

4.3.2.2 Porosity Effect on non-dimensional Frequency

Tables 4.8 to 4.11 provide a comprehensive analysis of the impact of porosity on various mixtures and shell geometries, utilizing different distribution schemes to illustrate the effects. The findings, supported by Figure 4.2, reveal a clear and consistent trend: an increase in porosity fraction generally correlates with a decrease in non-dimensional frequency values across most scenarios. This relationship underscores the significant role that porosity plays in influencing the dynamic behavior of functionally graded shell panels.

Notably, the comparative analysis of different porosity types indicates that types II and

III exhibit almost indistinguishable effects on frequency, suggesting that their distributions may not significantly alter the vibrational characteristics. In contrast, porosity type IV demonstrates the least impact on frequency, highlighting its relative insignificance compared to the others. On the other hand, type I, characterized by an even porosity distribution, shows the most pronounced influence, emphasizing how uniform material distribution can enhance or diminish vibrational performance.

Interestingly, certain scenarios present a more complex behavior: an increase in porosity leads to a rise in frequency values, albeit at a slower rate. This phenomenon is illustrated in Figure 4.2.a, where specific instances demonstrate that under certain conditions, higher porosity can contribute to increased frequency. This counterintuitive behavior can be attributed to several factors, including the power-law index, the specific type of porosity employed, and the thickness ratio of the shell panels. The interplay of these parameters creates a nuanced response that warrants further exploration.

In summary, the analysis captured in these tables and figures emphasizes the multifaceted influence of porosity on the vibrational characteristics of functionally graded shell panels. The varying effects of different porosity types and the unexpected scenarios where frequency increases with porosity highlight the need for careful consideration of material distribution in the design and optimization of shell structures. These insights are crucial for engineers and researchers aiming to leverage the properties of porous materials to enhance structural performance in practical applications.

Table 4.8: porosity effect on non-dimensional frequency $\bar{\omega}$ for an FGM sandwich shell with $n_x = n_z = 2, h/a = 0.1$ and SSSS boundary conditions FGM type A

R_x/a	R_y/b	Porosity type	ξ	1−0−1	1−1−1	1−2−1	2−1−2	2−2−1	2−1−1
∞	∞		0	1.32938	1.26216	1.21296	1.29314	1.23054	1.26637
		typeI	0.1	1.29920	1.20984	1.15428	1.24885	1.18003	1.22235
			0.2	1.26140	1.14848	1.08671	1.19648	1.12133	1.17082
		typeII	0.1	1.32211	1.23997	1.18624	1.27628	1.20897	1.24970
			0.2	1.31451	1.21645	1.15805	1.25849	1.18619	1.23217
		typeIII	0.1	1.32223	1.24034	1.18668	1.27656	1.20933	1.24998
			0.2	1.31501	1.21800	1.15990	1.25966	1.18769	1.23332
		typeIV	0.1	1.33588	1.25146	1.19491	1.28924	1.21847	1.26015

Continued on next page

R_x/a	R_y/b	Porosity type	ξ	1−0−1	1−1−1	1−2−1	2−1−2	2−2−1	2−1−1
			0.2	1.34071	1.24025	1.17607	1.28480	1.20590	1.25333
5	5		0	1.38347	1.31254	1.26185	1.34491	1.28347	1.28347
		typeI	0.1	1.35049	1.25929	1.20317	1.29893	1.23326	1.23326
			0.2	1.30854	1.19656	1.13556	1.24405	1.17462	1.17462
		typeII	0.1	1.37461	1.28978	1.23505	1.32708	1.26175	1.26175
			0.2	1.36510	1.26558	1.20675	1.30811	1.23870	1.23870
		typeIII	0.1	1.37475	1.29016	1.23550	1.32738	1.26211	1.26211
			0.2	1.36574	1.26717	1.20861	1.30937	1.24022	1.24022
		typeIV	0.1	1.38773	1.30073	1.24330	1.33944	1.27053	1.27053
			0.2	1.39013	1.28826	1.22389	1.33323	1.25701	1.25701
5	∞		0	1.34042	1.27235	1.22285	1.30363	1.24207	1.27826
		typeI	0.1	1.30962	1.21993	1.16433	1.25904	1.19205	1.23437
			0.2	1.27091	1.15840	1.09693	1.20619	1.13382	1.18287
		typeII	0.1	1.33277	1.25007	1.19618	1.28657	1.22060	1.26148
			0.2	1.32472	1.22644	1.16804	1.26854	1.19789	1.24379
		typeIII	0.1	1.33290	1.25044	1.19662	1.28686	1.22096	1.26176
			0.2	1.32525	1.22800	1.16989	1.26972	1.19939	1.24495
		typeIV	0.1	1.34633	1.26139	1.20472	1.29935	1.22982	1.27162
			0.2	1.35054	1.24989	1.18579	1.29447	1.21707	1.26440
5	7.5		0	1.36695	1.29712	1.24688	1.32907	1.26764	1.30461
		typeI	0.1	1.33482	1.24417	1.18823	1.28362	1.21752	1.26020
			0.2	1.29415	1.18189	1.12066	1.22952	1.15906	1.20786
		typeII	0.1	1.35856	1.27454	1.22011	1.31154	1.24602	1.28743
			0.2	1.34964	1.25055	1.19186	1.29294	1.22311	1.26926
		typeIII	0.1	1.35870	1.27492	1.22056	1.31183	1.24638	1.28772
			0.2	1.35023	1.25213	1.19372	1.29416	1.22462	1.27046
		typeIV	0.1	1.37187	1.28565	1.22849	1.32407	1.25498	1.29728
			0.2	1.37500	1.27356	1.20926	1.31840	1.24176	1.28933

Table 4.9: porosity effect on non-dimensional frequency $\bar{\omega}$ on FGM sandwich shell with $n_x = n_z = 2, h/a = 0.1$ and SSSS boundary conditions FGM type B

R_x/a	R_y/b	Porosity type	ξ	1−0−1	1−1−1	1−2−1	2−1−2	2−2−1	2−1−1
∞	∞		0	1.39786	1.32491	1.27034	1.35869	1.29079	1.32819
		typeI	0.1	1.37151	1.27838	1.21744	1.31948	1.24767	1.28981
			0.2	1.33728	1.22447	1.15752	1.27306	1.19909	1.24549
		typeII	0.1	1.39232	1.30557	1.24647	1.34432	1.27276	1.31418
			0.2	1.38629	1.28520	1.22149	1.32914	1.25400	1.29955
		typeIII	0.1	1.39241	1.30589	1.24687	1.34456	1.27306	1.31442
			0.2	1.38670	1.28654	1.22312	1.33014	1.25523	1.30051
		typeIV	0.1	1.40452	1.31595	1.25457	1.35583	1.28057	1.32224
			0.2	1.40931	1.30647	1.23818	1.35222	1.26991	1.31546
5	5		0	1.44499	1.36872	1.31316	1.40367	1.33669	1.37550
		typeI	0.1	1.41586	1.32098	1.25995	1.36258	1.29331	1.33596
			0.2	1.37794	1.26555	1.19970	1.31371	1.24423	1.28999
		typeII	0.1	1.43778	1.34862	1.28901	1.38816	1.31816	1.36044
			0.2	1.42992	1.32741	1.26372	1.37173	1.29883	1.34464
		typeIII	0.1	1.43790	1.34895	1.28941	1.38841	1.31847	1.36069
			0.2	1.43045	1.32880	1.26538	1.37281	1.30009	1.34568
		typeIV	0.1	1.44949	1.35852	1.29668	1.39918	1.32538	1.36792
			0.2	1.45212	1.34773	1.27956	1.39387	1.31363	1.35958
5	∞		0	1.40425	1.33112	1.27674	1.36490	1.29800	1.33539
		typeI	0.1	1.37691	1.28419	1.22377	1.32505	1.25495	1.29669
			0.2	1.34137	1.22978	1.16377	1.27779	1.20638	1.25192
		typeII	0.1	1.39812	1.31152	1.25279	1.35013	1.27984	1.32102
			0.2	1.39146	1.29087	1.22771	1.33453	1.26093	1.30599
		typeIII	0.1	1.39822	1.31185	1.25319	1.35038	1.28014	1.32125
			0.2	1.39191	1.29223	1.22935	1.33556	1.26216	1.30698
		typeIV	0.1	1.40452	1.32176	1.26075	1.36151	1.28742	1.32886
			0.2	1.40931	1.31187	1.24413	1.35736	1.27644	1.32157
5	7.5		0	1.42902	1.35405	1.29899	1.38852	1.32162	1.35983
		typeI	0.1	1.40054	1.30658	1.24582	1.34786	1.27836	1.32059

Continued on next page

R_x/a	R_y/b	Porosity type	ξ	1−0−1	1−1−1	1−2−1	2−1−2	2−2−1	2−1−1
			0.2	1.36349	1.25150	1.18562	1.29956	1.22945	1.27506
		typeII	0.1	1.42221	1.33413	1.27489	1.37327	1.30322	1.34502
			0.2	1.41481	1.31311	1.24967	1.35715	1.28404	1.32950
		typeIII	0.1	1.42233	1.33446	1.27529	1.37353	1.30353	1.34527
			0.2	1.41531	1.31449	1.25132	1.35821	1.28529	1.33052
		typeIV	0.1	1.43408	1.34417	1.28269	1.38445	1.31058	1.35265
			0.2	1.43729	1.33372	1.26574	1.37959	1.29912	1.34470

Table 4.10: porosity effect on non-dimensional frequency $\bar{\omega}$ on FGM sandwich shell with $n_x = n_z = 2, h/a = 0.1$ and SSSS boundary conditions FGM type C

R_x/a	R_y/b	Porosity type	ξ	1−0−1	1−1−1	1−2−1	2−1−2	2−2−1	2−1−1
∞	∞		0	1.14047	1.14236	1.14663	1.14002	1.13909	1.13844
		typeI	0.1	1.13727	1.13990	1.13741	1.13930	1.13763	1.13568
			0.2	1.13001	1.13586	1.12710	1.13598	1.13291	1.12808
		typeII	0.1	1.14402	1.14368	1.14583	1.14263	1.14062	1.13864
			0.2	1.14705	1.14506	1.14525	1.14507	1.14181	1.13814
		typeIII	0.1	1.14394	1.14368	1.14589	1.14259	1.14066	1.13869
			0.2	1.14679	1.14509	1.14548	1.14497	1.14198	1.13841
		typeIV	0.1	1.14851	1.14564	1.13803	1.14806	1.14383	1.14471
			0.2	1.15681	1.14951	1.12854	1.15667	1.14864	1.15076
5	5		0	1.20946	1.20716	1.20930	1.20655	1.19583	1.19500
		typeI	0.1	1.19925	1.19787	1.19399	1.19873	1.18722	1.18517
			0.2	1.18497	1.18634	1.17653	1.18795	1.17502	1.17059
		typeII	0.1	1.20932	1.20512	1.20555	1.20558	1.19393	1.19174
			0.2	1.20876	1.20306	1.20183	1.20446	1.19171	1.18789
		typeIII	0.1	1.20932	1.20520	1.20568	1.20563	1.19404	1.19187
			0.2	1.20884	1.20340	1.20233	1.20467	1.19215	1.18844
		typeIV	0.1	1.21481	1.20758	1.19881	1.21147	1.19707	1.19765
			0.2	1.22026	1.20789	1.18627	1.21657	1.19786	1.19998

Continued on next page

R_x/a	R_y/b	Porosity type	ξ	1−0−1	1−1−1	1−2−1	2−1−2	2−2−1	2−1−1
5	∞		0	1.15434	1.15499	1.15867	1.15314	1.14935	1.14860
		typeI	0.1	1.14830	1.14989	1.14717	1.14963	1.14506	1.14294
			0.2	1.13831	1.14309	1.13430	1.14350	1.13750	1.13260
		typeII	0.1	1.15643	1.15502	1.15680	1.15436	1.14955	1.14740
			0.2	1.15809	1.15514	1.15512	1.15546	1.14946	1.14557
		typeIII	0.1	1.15639	1.15506	1.15689	1.15436	1.14962	1.14748
			0.2	1.15795	1.15529	1.15545	1.15547	1.14973	1.14595
		typeIV	0.1	1.16152	1.15736	1.14958	1.16016	1.15289	1.15354
			0.2	1.16890	1.16004	1.13909	1.16760	1.15629	1.15825
5	7.5		0	1.18782	1.18667	1.18942	1.18557	1.17756	1.17675
		typeI	0.1	1.17911	1.17891	1.17551	1.17932	1.17052	1.16842
			0.2	1.16639	1.16914	1.15976	1.17026	1.16003	1.15538
		typeII	0.1	1.18849	1.18539	1.18637	1.18541	1.17643	1.17424
			0.2	1.18875	1.18414	1.18342	1.18510	1.17500	1.17113
		typeIII	0.1	1.18848	1.18546	1.18648	1.18544	1.17652	1.17435
			0.2	1.18875	1.18441	1.18385	1.18524	1.17538	1.17161
		typeIV	0.1	1.19388	1.18784	1.17948	1.19130	1.17967	1.18026
			0.2	1.20007	1.18906	1.16772	1.19730	1.18146	1.18349

Table 4.11: porosity effect on non-dimensional frequency $\bar{\omega}$ on FGM sandwich shell with $n_x = n_z = 2, h/a = 0.1$ and SSSS boundary conditions FGM type D

R_x/a	R_y/b	Porosity type	ξ	1−0−1	1−1−1	1−2−1	2−1−2	2−2−1	2−1−1
∞	∞		0	1.00241	1.07820	1.14808	1.03868	1.11434	1.06714
		typeI	0.1	0.92245	1.01391	1.09340	0.96727	1.05336	0.99810
			0.2	0.81555	0.93061	1.02427	0.87307	0.97470	0.90702
		typeII	0.1	0.97317	1.05166	1.12781	1.00946	1.09019	1.03956
			0.2	0.94077	1.02262	1.10602	0.97723	1.06388	1.00917
		typeIII	0.1	0.97367	1.05205	1.12806	1.00992	1.09053	1.03999
			0.2	0.94295	1.02432	1.10714	0.97923	1.06539	1.01107

Continued on next page

R_x/a	R_y/b	Porosity type	ξ	1−0−1	1−1−1	1−2−1	2−1−2	2−2−1	2−1−1
		typeIV	0.1	0.99726	1.06488	1.13182	1.02852	1.10364	1.05823
			0.2	0.99200	1.05076	1.11427	1.01787	1.09233	1.04897
5	5		0	1.07688	1.16217	1.23314	1.11999	1.19649	1.14634
		typeI	0.1	0.99782	1.09861	1.17864	1.04959	1.13621	1.07836
			0.2	0.89125	1.01587	1.10914	0.95655	1.05807	0.98853
		typeII	0.1	1.04742	1.13571	1.21257	1.09091	1.17237	1.11897
			0.2	1.01465	1.10661	1.19028	1.05871	1.14592	1.08864
		typeIII	0.1	1.04793	1.13611	1.21285	1.09137	1.17274	1.11941
			0.2	1.01686	1.10837	1.19152	1.06075	1.14753	1.09060
		typeIV	0.1	1.06966	1.14851	1.21760	1.10867	1.18541	1.13598
			0.2	1.06196	1.13373	1.20046	1.09653	1.17345	1.12500
5	∞		0	1.01958	1.09779	1.16782	1.05762	1.13298	1.08498
		typeI	0.1	0.94012	1.03394	1.11343	0.98674	1.07249	1.01653
			0.2	0.83295	0.95115	1.04452	0.89323	0.99439	0.92625
		typeII	0.1	0.99038	1.07137	1.14756	1.02855	1.10897	1.05761
			0.2	0.95799	1.04243	1.12575	0.99644	1.08276	1.02739
		typeIII	0.1	0.99088	1.07176	1.14782	1.02900	1.10932	1.05804
			0.2	0.96017	1.04414	1.12689	0.99845	1.08429	1.02929
		typeIV	0.1	1.01391	1.08461	1.15218	1.04727	1.12244	1.07573
			0.2	1.00804	1.07055	1.13517	1.03634	1.11123	1.06608
5	∞		0	1.05455	1.13708	1.20770	1.09568	1.17170	1.12237
		typeI	0.1	0.97531	1.07339	1.15323	1.02507	1.11134	1.05420
			0.2	0.86851	0.99063	1.08396	0.93185	1.03322	0.96421
		typeII	0.1	1.02519	1.11063	1.18725	1.06659	1.14762	1.09499
			0.2	0.99256	1.08159	1.16515	1.03443	1.12127	1.06472
		typeIII	0.1	1.02569	1.11102	1.18752	1.06705	1.14798	1.09543
			0.2	0.99476	1.08333	1.16634	1.03645	1.12285	1.06665
		typeIV	0.1	1.04794	1.12363	1.19217	1.08475	1.16086	1.11244
			0.2	1.04096	1.10916	1.17513	1.07309	1.14922	1.10199

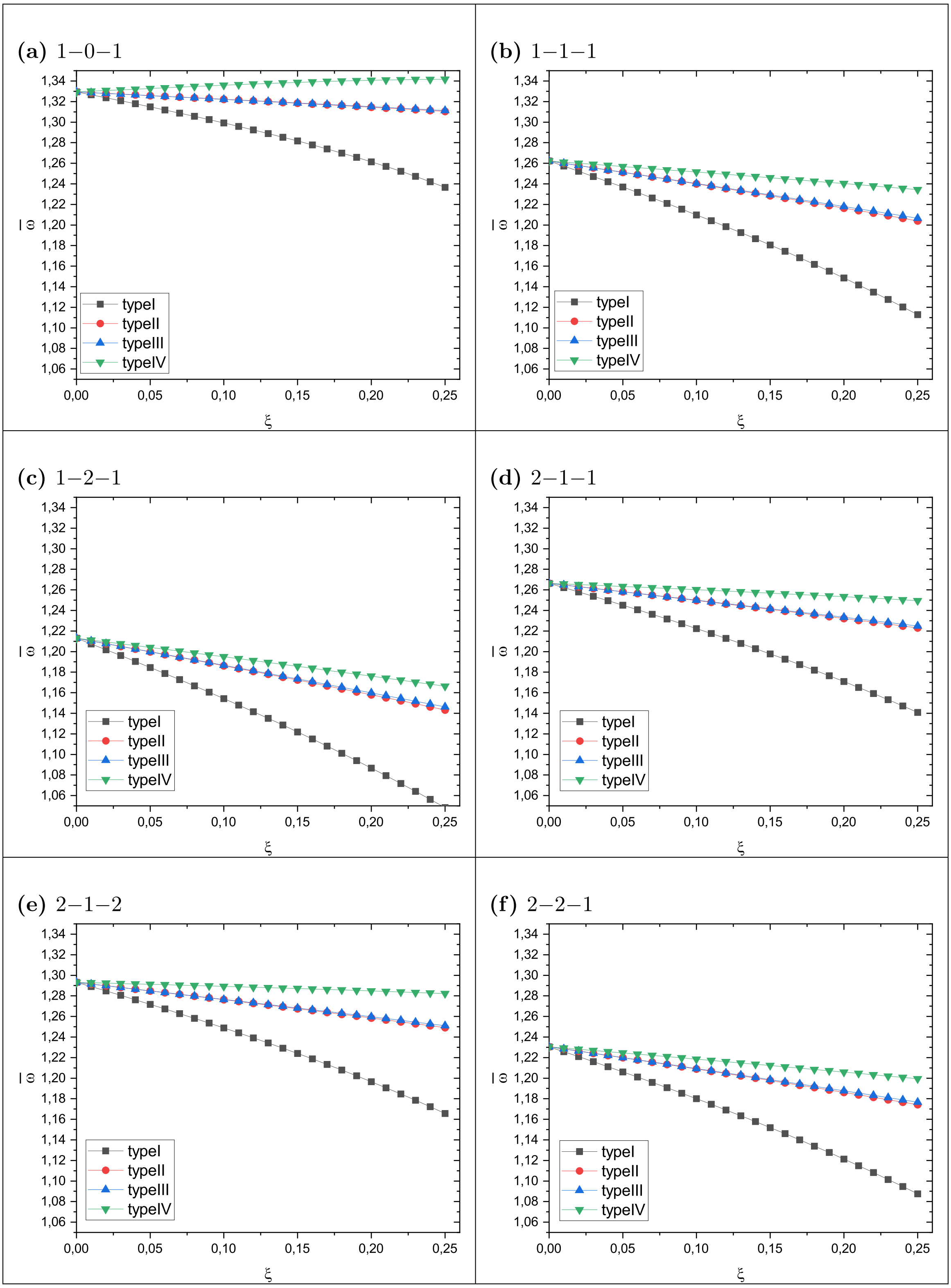

Figure 4.2: Effect of porosity type and value on non-dimensional frequency for different sandwich layup scenarios.

4.4 Optimization Remarks

Avoiding resonance frequency is essential in vibration analysis because resonance occurs when the natural frequency of a structure coincides with the frequency of external vibrations or loads. This can lead to excessive oscillations, which in turn may cause significant damage, reduced performance, or even catastrophic failure. By conducting an optimization study, engineers can adjust the material properties, structural layout, or geometrical parameters to shift the natural frequencies away from these critical resonant frequencies. This helps ensure that the structure operates safely and efficiently within its intended environment, avoiding amplified vibrations and prolonging its lifespan.

4.4.1 Optimization of Gradient indexes effect

The data shows that increasing the gradient indices n_x and n_z generally reduces the frequency parameter $\overline{\omega}$.
To achieve higher vibration frequencies (which may be desirable in some applications), using lower gradient indices seems beneficial, as it leads to the highest values of $\overline{\omega}$. Conversely, for applications where lower vibration frequencies are preferable (such as damping or energy absorption), higher gradient indices may be more suitable.

4.4.2 Optimization of Sandwich Layups effect

for FGM type A and B The layup configuration $1-0-1$ tends to yield higher frequency values compared to the others. This configuration could be recommended for applications where a higher natural frequency is desirable, potentially leading to more robust structures against vibrations.
On the other hand, the $2-2-1$ configuration consistently results in lower frequency values. This configuration might be optimal for designs that require flexibility or where damping properties are critical.
A common trend observed between FGM types C and D is that the highest frequency is recorded for the $1-2-1$ layup configuration. For FGM type D, the lowest frequency is noted for the $1-0-1$ configuration, whereas FGM type C exhibits similar low-frequency values across multiple layup configurations.

4.4.3 porosity on Frequency parameter effect

In the analysis of bi-directional functionally graded (bi-FGM) doubly curved shell panels, porosity is introduced as a manufacturing defect. These defects manifest as voids or pores within the material, which can significantly affect the structural performance, particularly the vibrational characteristics. The study's findings reveal that porosity generally leads to a decrease in the non-dimensional frequency for most FGM types (A, B, D), which indicates a degradation in the stiffness and, consequently, the dynamic stability of the structure.

However, in certain cases—specifically for FGM types A and B with layups $1-0-1$—the introduction of porosity type VI results in an unusual increase in frequency. This deviation suggests that the specific distribution and layup design can interact with the porosity type in a way that mitigates the detrimental effects of the defects. Such an observation opens the door to optimization strategies that could exploit these interactions to enhance performance.

For FGM type C, the effect of porosity is less predictable, with frequency behavior strongly influenced by the geometry, porosity type, and sandwich layup. This variability suggests that an optimization approach must be tailored to the specific design configuration.

4.5 Conclusion

In this comprehensive chapter, an exploration of the free vibration responses exhibited by sandwich FG shell panels of diverse geometries, including spherical, cylindrical, hyperbolic, and elliptical shapes, was undertaken. The analysis encompassed an in-depth examination of the responses across four distinct mixtures, revealing a multifaceted interplay of factors influencing the shell panels' behavior.

Throughout the analysis, it became evident that the intricate interplay of porosity distribution, magnitude, gradient index, curvature ratio, and sandwich layups exerted profound effects on the response characteristics of the shell panels. Each of these factors played a pivotal role in shaping the vibrational behavior, underscoring the nuanced nature of their influence.

By delving into these complexities, valuable insights into the intricate dynamics governing the free vibration responses of sandwich FG shell panels were gained. The findings not only enhance the understanding of these complex systems but also pave the way for further research and innovation in the field. As this chapter concludes, the stage is set to apply these insights to propel advancements in structural design, engineering optimization, and beyond.

Chapter 5

Thermal buckling analysis of bi-FGM doubly curved shell panels

5.1 Introduction

In structural engineering, ensuring the stability and reliability of complex structures under varying environmental conditions is paramount. One critical phenomenon that engineers must contend with is thermal buckling. Thermal buckling occurs when temperature-induced deformations lead to structural instability, potentially resulting in catastrophic failure. Understanding and analyzing thermal buckling phenomena are therefore essential for designing robust and resilient structures, particularly those subjected to extreme thermal environments.

The focus of this thesis is on thermal buckling analysis applied to shell panels constructed from functionally graded materials (FGMs). These panels represent a class of advanced composite structures known for their lightweight, high strength, and tailored mechanical properties. Functionally graded materials exhibit spatial variations in composition and microstructure, allowing for enhanced thermal and mechanical performance compared to traditional homogeneous materials.

The integration of FGMs in shell panels presents both opportunities and challenges in structural design. While FGMs offer superior thermal stability and load-bearing capacity, the complex interplay between material composition, thermal gradients, and geometric configurations necessitates thorough analysis to mitigate the risk of thermal buckling.

The importance of thermal buckling analysis in the context of shell panels made of FGMs cannot be overstated. These panels find widespread applications in aerospace, automotive, marine, and civil engineering industries, where they are subjected to diverse thermal environments ranging from extreme cold to high temperatures. Understanding how ther-

mal fluctuations influence the structural integrity of FGM panels is crucial for ensuring their performance and longevity in service.
By conducting rigorous thermal buckling analysis, engineers can identify critical temperature thresholds at which buckling may occur and assess the structural response under thermal loading conditions. This knowledge enables informed decision-making in structural design, material selection, and optimization processes. Moreover, it contributes to the development of innovative design strategies and advanced manufacturing techniques aimed at enhancing the thermal stability and reliability of FGM shell panels.
In summary, this chapter aims to delve into the intricacies of thermal buckling analysis for shell panels made of functionally graded materials. Through comprehensive investigation and numerical simulations, valuable insights will be gained into the thermal behavior and stability characteristics of these advanced composite structures.

5.2 Solution Methodology

In this chapter, a thermal buckling analysis is conducted on a bi-directional single-layer shell panel with dimensions $a \times b$ and a thickness of h. The shell panel is examined under three distinct temperature distributions: uniform, linear, and non-linear. Both temperature-dependent and temperature-independent material properties are considered. The equation of motion for the system, derived in Chapter 2, serves as the basis for this analysis. It is assumed that the temperature change occurs in the z-direction. The mechanical properties of the FGM constituents used in this chapter are detailed in Table 5.1. The analysis investigates the effects of various conditions on the buckling behavior, with thorough discussions provided throughout the study.

5.3 Results Discussion

The initial phase involves a validation study to ensure the accuracy of the algorithm, including a comparative analysis with findings reported in the literature. In the subsequent phase, novel results concerning bi-directional functionally graded material (FGM) shells under thermal effects will be presented. This section will highlight the influence of various parameters on the buckling behavior.

Table 5.1: Material Properties of the constituents [2,3]

TID/TD	Property		Ni	SUS_3O_4	Si_3N_4	Al_2O_3
TD Properties	$E(Pa)$	P0	223.95e+9	201.04e+9	348.43e+9	349.55e+9
		P-1	0	0	0	0
		P1	-2.794e-4	3.079e-4	-3.070e-4	-3.853e-4
		P2	3.998e-9	-6.534e-7	2.160e-7	4.027e-7
		P3	0	0	-8.946e-11	-1.673e-11
	ν_m	P0	0.31	0.3262	0.24	0.26
		P-1	0	0	0	0
		P1	0	-2.002e-4	0	0
		P2	0	3.797e-7	0	0
		P3	0	0	0	0
	$\alpha(K^{-1})$	P0	9.9209e-6	12.330e-6	5.8723e-6	6.8269e-6
		P-1	0	0	0	0
		P1	8.705e-4	8.086e-4	9.095e-4	1.834e-4
		P2	0	0	0	0
		P3	0	0	0	0
	$k(W/m \cdot K)$	P0	187.66	12.04	9.19	-14.087
		P-1	0	0	0	0
		P1	-4.614e-4	0	0	-1123.6
		P2	6.670e-7	0	0	-6.227e-3
		P3	-1.523e-10	0	0	0
TID Properties	$E(Pa)$		204e+9	2.08e+11	322e+9	380.0e+9
	ν_m		0.31	0.318	0.24	0.3
	$\alpha(K^{-1})$		13.2e-6	1.53e-5	7.47e-6	7.4e-6
	$k(W/m \cdot K)$		90.7	12.04	9.19	10.4

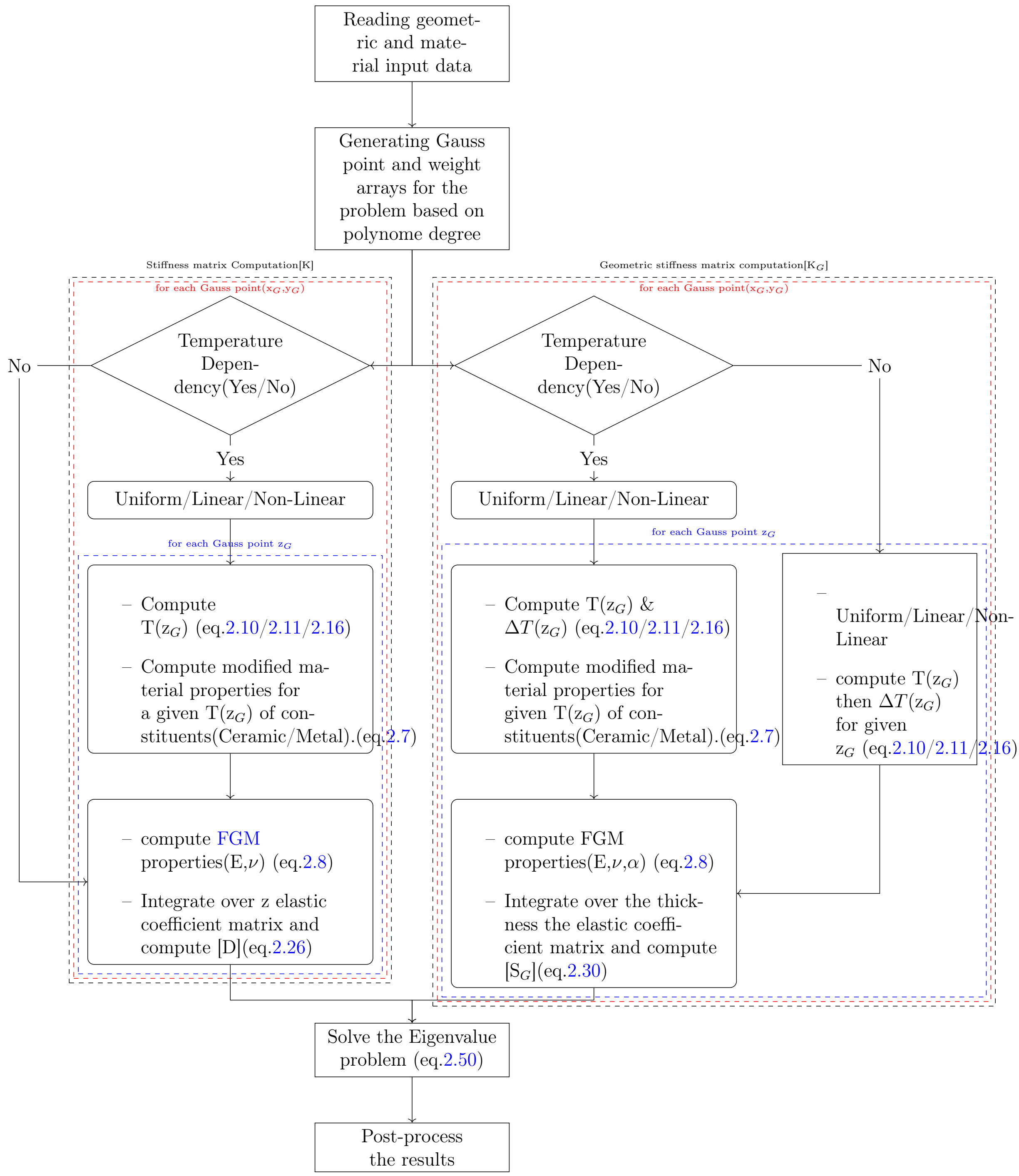

Figure 5.1: Flowchart illustrating the logical framework of the custom-made fortran code in thermal buckling

5.3.1 Validation Study

The initial phase of the study includes a convergence analysis of the proposed algorithm. A fully clamped Ni/Si_3N_4 FG plate, with material properties detailed by 5.1, is subjected to a uniform temperature distribution (n_x=0). The geometric and material properties of the functionally graded plate are defined as a/b = 1 and R_x= R_y=∞, with two distinct thickness ratios considered (a/h = 50 and a/h = 30). The buckling temperature-rise parameter is expressed as $\Delta T_{cr}=\alpha_0 \times \Delta T_{cr} \times 10^3$, where α_0 represents the thermal expansion coefficient of Nickel at T_0= 300K. The results, presented in Table 5.2,indicate a rapid convergence towards the solution, with a polynomial of eighth degree being sufficient. Additionally, there is substantial agreement between the findings and the results available in the existing literature. The reader will notice the significant advantage of the p-version over the h-version, as evidenced by the method's swift convergence rate. Experimentation with the code revealed that a polynomial of p = 8 was sufficient for accurate results.

Table 5.2: Convergence study of Critical buckling temperatures rise ($\Delta T_{cr} = \Delta T_{cr} \times \alpha_0 \times 10^3$) of Ni/$Si_3N_4$ CCCC square plate under the uniform temperature distribution (n_x=0)

Power-law Index (n_z)	Source	polynome degree (P)	ΔT_{cr} a/h=30 TID	a/h=30 TD	a/h=50 TID	a/h=50 TD
0	Present	3	346.69	157.59	341.37	155.17
		5	14.480	6.5821	5.2943	2.4065
		7	14.076	6.3981	5.1387	2.3358
		8	14.070	6.3957	5.1368	2.3349
	FSDT [74]		14.795	6.4324	5.4018	2.3485
	NSDT [99]		14.086	4.9840	5.1098	2.0783
	DQM [100]		14.087	4.9867	5.1235	2.0828
0.5	Present	3	172.87	124.05	170.22	122.13
		5	7.2833	5.2152	2.6636	1.9069
		7	7.0799	5.0695	2.5854	1.8508
		8	7.0772	5.0676	2.5844	1.8502
	FSDT [74]		7.4311	5.0741	2.7137	1.8527
	NSDT [99]		7.0872	4.1135	2.5711	1.6822
	DQM [100]		6.9458	4.0583	2.5260	1.6609

Continued on next page

n_z	Source	(P)	TID	TD	TID	TD
2	Present	3	111.46	100.69	109.61	99.029
		5	4.9861	4.5023	1.8251	1.6481
		7	4.8477	4.3773	1.7716	1.5998
		8	4.8458	4.3757	1.7709	1.5992
	FSDT [74]		5.0803	4.3583	1.8564	1.5929
	NSDT [99]		4.8549	3.6520	1.7621	1.4735
	DQM [100]		4.8657	3.6595	1.7712	1.4798
10	Present	3	85.004	86.338	83.501	84.814
		5	4.0076	4.0842	1.4680	1.4963
		7	3.8969	3.9714	1.4250	1.4525
		8	3.8954	3.9699	1.4245	1.4520
	FSDT [74]		4.0616	3.9274	1.4853	1.4367
	NSDT [99]		3.9039	3.3740	1.4176	1.3493
	DQM [100]		4.0680	3.4825	1.4822	1.3976
∞	Present	3	76.947	81.124	75.639	79.745
		5	3.5236	3.7150	1.2899	1.3599
		7	3.4259	3.6119	1.2521	1.3201
		8	3.4246	3.6105	1.2516	1.3196
	FSDT [74]		3.6309	3.6191	1.3272	1.3229
	NSDT [99]		3.4922	3.1352	1.2678	1.2490
	DQM [100]		3.4271	3.0894	1.2480	1.2328

The second example, detailed in Table 5.3, aims to evaluate the code's capability to handle scenarios with linear and non-linear temperature distributions. A comparative study was conducted by benchmarking the obtained results against those presented by [101]. The plate under consideration is composed of Aluminium and Alumina (Al/Al_2O_3). The material properties of Alumina are provided in Table 5.1, while the Aluminium properties are as follows: (E_m=70GPa, ν_m=0.3, α_m=23$\times$10^{-6}K^{-1},k_m=204 W/m.K). The plate is fully simply supported with an aspect ratio of (a/b = 1) and a thickness ratio of (a/h = 20). In this scenario, the buckling temperature rise parameter is denoted as (ΔT_{cr}) and scaled by a factor of (10^{-3}). The results show the influence of the gradient index (n_z) (n_x= 0) on the buckling temperature rise for both linear and non-linear temperature distributions. The findings align closely with those reported in the literature, demonstrating an error margin of no more than 2.51% in the worst-case scenario.

Table 5.3: Critical buckling temperature change (ΔT_{cr}=$\Delta T_{cr}\times10^{-3}$) of SSSS Al/$Al_2O_3$ TID FGM plate under linear and non-linear temperature rise for different values of power law index n_z (a/h=20,a/b=1)

power law	Linear			Non-linear		
index n_z	Present	[101]	diff (%)	Present	[101]	diff (%)
0	0.8397	0.8343	0.64	0.8397	0.8342	0.65
0.5	0.4772	0.4694	1.63	0.6291	0.6187	1.65
1.0	0.3671	0.3593	2.12	0.5096	0.4987	2.13
1.5	0.3234	0.3158	2.35	0.4494	0.4387	2.38
2.0	0.3053	0.2977	2.49	0.4187	0.4083	2.48
2.5	0.2985	0.2911	2.48	0.4025	0.3924	2.51
3.0	0.2971	0.2898	2.46	0.3937	0.3839	2.49
3.5	0.2983	0.2910	2.45	0.3889	0.3793	2.47
4.0	0.3007	0.2934	2.43	0.3861	0.3767	2.43
4.5	0.3036	0.2963	2.40	0.3844	0.3751	2.42
5.0	0.3065	0.2992	2.38	0.3833	0.3741	2.40
5.5	0.3093	0.3020	2.36	0.3824	0.3733	2.38
6.0	0.3118	0.3045	2.34	0.3816	0.3726	2.36
6.5	0.3141	0.3068	2.32	0.3808	0.3719	2.34
7.0	0.3161	0.3088	2.31	0.3799	0.3711	2.32
7.5	0.3179	0.3106	2.30	0.3791	0.3703	2.32
8.0	0.3194	0.3121	2.29	0.3781	0.3694	2.30
8.5	0.3208	0.3134	2.31	0.3772	0.3685	2.31
9.0	0.3219	0.3145	2.30	0.3761	0.3675	2.29
9.5	0.3228	0.3154	2.29	0.3750	0.3664	2.29
10.0	0.3235	0.3161	2.29	0.3739	0.3653	2.30

In the following analysis (see tables 5.4-5.5-5.6), a comparative study was conducted based on the work of Kar et al. [102] to validate the algorithm's performance in the context of doubly curved shell geometry. The primary objective was to examine the impact of various boundary conditions and curvature ratios (R/a) on different shell geometries and their effect on the buckling load parameter. This investigation encompassed scenarios with both uniform and linear temperature distributions. The selected shell panel is made from Si3N4/SUS304. It is important to note that the material properties used in this study slightly differ from those listed in Table 5.1. For exact property details, referring to the cited source is advised. The thickness aspect ratio is defined as a/h = 10, with temperatures set at T_c = 500K and T_m= 300K (n_x= 0; n_z= 2). The results demonstrate a close alignment with the data published in the reference, confirming the accuracy of the algorithm.

The aim of this chapter is to address the existing gap in research on doubly curved shell geometry, particularly in comparison to other geometries. The literature on this specific issue is limited, making validation challenging. In the initial examples, flat panels were intentionally selected due to their extensive study, facilitating easier comparisons across different cases.

Table 5.4: Critical buckling load parameter (λ_{cr}) of Si_3N_4/SUS_3O_4 FGM ($n_z = 2; n_x = 0$) shell under uniform and linear temperature rise (a/h=10;R/a=5;a/b=1;$T_c = 500K; T_m = 300K$) and different boundary conditions

Shell geometry	BC	Source	Uniform		Linear	
			TID	TD	TID	TD
Spherical R_x=R_y=R	CCCC	Present	12.1184	10.6328	25.5572	23.5608
		[102]	12.2467	10.8100	25.3660	23.4330
		Diff (%)	-1.059	-1.667	0.784	0.542
	SCSC	Present	9.0976	7.9801	19.1588	17.6646
		[102]	9.2807	8.1920	19.1953	17.7351
		Diff (%)	-2.01	-2.65	-0.19	-0.40
	CFCF	Present	6.1625	5.3942	12.9342	11.9181
		[102]	6.2973	5.5585	12.9735	11.9857
		Diff (%)	-2.19	-3.05	-0.30	-0.57
Cylindrical R_x=R, R_y=∞	CCCC	Present	11.6879	10.2561	24.6984	22.7690
		[102]	11.8070	10.4220	24.5041	22.6393
		Diff (%)	-1.02	-1.62	0.79	0.57

Continued on next page

			TID	TD	TID	TD
	SCSC	Present	8.8641	7.7783	18.6996	17.2415
		[102]	8.8062	7.7732	18.2567	16.8700
		Diff (%)	0.65	0.07	2.37	2.15
	CFCF	Present	5.9084	5.1705	12.4377	11.4627
		[102]	6.0618	5.3507	12.5250	11.5730
		Diff (%)	-2.60	-3.48	-0.70	-0.97
Hyperbolic	CCCC	Present	11.8772	10.4234	25.1487	23.1829
R_x=R,		[102]	11.9574	10.5548	24.8663	22.9750
R_y=-R		Diff (%)	-0.65	-1.26	1.12	0.89
	SCSC	Present	8.9298	7.8385	18.8712	17.3989
		[102]	9.0404	7.9801	18.7870	17.3606
		Diff (%)	-1.24	-1.81	0.45	0.22
	CFCF	Present	6.1429	5.3746	12.9688	11.9533
		[102]	6.3112	5.5709	13.0778	12.0843
		Diff (%)	-2.74	-3.65	-0.84	-1.10
Elliptical	CCCC	Present	11.8266	10.3772	24.9666	23.0164
R_x=R,		[102]	11.9542	10.5518	24.7848	22.8975
R_y=2R		Diff (%)	-1.07	-1.68	0.73	0.52
	SCSC	Present	8.9433	7.8464	18.8503	17.3804
		[102]	8.9554	7.9049	18.5442	17.1348
		Diff (%)	-0.14	-0.75	1.62	1.41
	CFCF	Present	5.9750	5.2294	12.5593	11.5738
		[102]	6.1197	5.4018	12.6261	11.6658
		Diff (%)	-2.42	-3.30	-0.53	-0.79

Table 5.5: Comparison study of the Critical buckling load parameter (λ_{cr}) of Si_3N_4/SUS_3O_4 SSSS FGM ($n_z = 2; n_x = 0$) (Spherical/Cylindrical) shell panel under uniform and linear temperature rise and different curvature ratios (R/a); ($T_c = 500K; T_m = 300K$)

Shell geometry	R/a	Source	Uniform		Linear	
			TID	TD	TID	TD
Spherical	10	Present	4.9389	4.3341	10.4023	9.5942
R_x=R_y=R		[102]	5.0175	4.4290	10.3783	9.5917
		Diff (%)	-1.59	-2.19	0.23	0.026
	20	Present	4.8525	4.2599	10.2318	9.4369
		[102]	4.9118	4.3357	10.1708	9.4006
		Diff (%)	-1.22	-1.78	-0.59	0.38
	50	Present	4.8343	4.2449	10.2003	9.4077
		[102]	4.8820	4.3094	10.1159	9.3500
		Diff (%)	-0.99	-1.52	0.83	0.61
	100	Present	4.8339	4.2448	10.2016	9.4088
		[102]	4.8777	4.3056	10.1091	9.3439
		Diff (%)	-0.91	-1.43	0.91	0.69
Cylindrical	10	Present	4.8513	4.2588	10.2292	9.4345
R_x=R,		[102]	4.9105	4.3346	10.1683	9.3983
R_y=∞		Diff (%)	-1.22	-1.78	0.60	0.38
	20	Present	4.8353	4.2456	10.2012	9.4085
		[102]	4.8849	4.3120	10.1208	9.3546
		Diff (%)	-1.03	-1.56	0.79	0.57
	50	Present	4.8338	4.2447	10.2015	9.4087
		[102]	4.8776	4.3055	10.1091	9.3438
		Diff (%)	-0.91	-1.43	0.91	0.69
	100	Present	4.8347	4.2456	10.2044	9.4114

Continued on next page

			TID	TD	TID	TD
		[102]	4.8765	4.3046	10.1079	9.3428
		Diff (%)	-0.86	-1.39	0.95	0.73

Table 5.6: Comparison study of the Critical buckling load parameter (λ_{cr}) of Si_3N_4/SUS_3O_4 SSSS FGM ($n_z = 2; n_x = 0$) (Hyperbolic/Elliptic) shell panel under uniform and linear temperature rise and different curvature ratios (R/a); ($T_c = 500K; T_m = 300K$)

Shell geometry	BC	Source	Uniform		Linear	
			TID	TD	TID	TD
Hyperbolic	10	Present	4.8312	4.2427	10.1982	9.4057
R_x=R,		[102]	4.8712	4.2998	10.0981	9.3338
R_y=-R		Diff (%)	-0.83	-1.35	0.98	0.76
	20	Present	4.8350	4.2460	10.2062	9.4130
		[102]	4.8749	4.3031	10.1057	9.3408
		Diff (%)	-0.83	-1.35	0.98	0.77
	50	Present	4.8360	4.2469	10.2084	9.4150
		[102]	4.8759	4.3040	10.1078	9.3428
		Diff (%)	-0.83	-1.34	0.99	0.77
	100	Present	4.8362	4.2471	10.2087	9.4153
		[102]	4.8761	4.3042	10.1081	9.3430
		Diff (%)	-0.83	-1.34	0.99	0.77
Elliplic	10	Present	4.8866	4.2890	10.2979	9.4980
R_x=R,		[102]	4.9556	4.3743	10.2558	9.4789
R_y=2R		Diff (%)	-1.41	-1.99	0.41	0.20
	20	Present	4.8418	4.2509	10.2120	9.4186
		[102]	4.8962	4.3220	10.1415	9.3735
		Diff (%)	-1.12	-1.67	0.69	0.48

Continued on next page

		TID	TD	TID	TD
50	Present	4.8337	4.2445	10.2002	9.4076
	[102]	4.8795	4.3072	10.1118	9.3463
	Diff (%)	-0.95	-1.48	0.87	0.65
100	Present	4.8342	4.2451	10.2028	9.4100
	[102]	4.8770	4.3050	10.1084	9.3432
	Diff (%)	-0.89	-1.41	-0.93	-0.71

5.3.2 Parametric Study

In this subsection, a thermal buckling analysis of bi-directional functionally graded doubly curved shell panels will be conducted. Notably, the buckling load parameter used here will be scaled by a factor of 10^{-3} for consistency.

5.3.2.1 Gradient indexes effect on buckling temperature Rise

The first example examines the impact of gradient indexes on bi-directional functionally graded shell panels, with findings detailed in Tables 5.7 and 5.8. The analysis is based on the assumption of SSSS boundary conditions, with material properties corresponding to a composite of Si_3N_4 and SUS_3O_4. A thickness ratio of $a/h = 5$ is utilized, and the shell panels are modeled with a square aspect ratio to maintain consistency in the geometry.
The results indicate a significant trend: as the power law indexes increase, the buckling temperature decreases across all examined shell geometries. This finding suggests that the gradient index plays a critical role in influencing the thermal stability of the panels. Additionally, the analysis reveals that the increase in buckling temperature is minimal for a uniform temperature distribution when compared to linear or non-linear temperature distributions. This observation underscores the importance of temperature distribution in assessing the buckling behavior of functionally graded materials.
Interestingly, when considering temperature dependence, the buckling load parameter remains relatively consistent across different scenarios. This suggests that the overall influence of temperature on buckling load may be less pronounced than anticipated, providing valuable insights for the design and analysis of these shell structures.
For enhanced visualization of these findings, similar results are presented in Figure 5.2, which focuses specifically on a spherical shell panel. The figure illustrates the effects of gradient indexes on buckling behavior, with detailed assumptions and conditions provided

in the caption. This comprehensive approach allows for a clearer understanding of how gradient indexes interact with thermal loads, contributing to the broader knowledge base regarding the performance of bi-directional functionally graded shell panels under varying conditions.

Table 5.7: Effect of gradient indexes (n_x and n_z) on buckling temperature rise ($\Delta T_{cr} = 10^{-3} \times \Delta T_{cr}$) of (Spherical/Cylindrical) SSSS Si_3N_4/SUS_304 shell panel (a/h=5;a/b=1)

Shell geometry	n_x	n_z	Uniform		Linear		Non-Linear	
			TID	TD	TID	TD	TID	TD
$R_x=R_y=5$ (Spherical)	0	0	5.8128	5.8052	11.5215	11.5093	11.5215	11.5093
		0.5	4.1644	4.1578	8.8601	8.8470	9.2148	9.2012
		1	3.6772	3.6712	7.8352	7.8227	8.2239	8.2108
		5	3.0201	3.0155	6.2130	6.2038	6.4217	6.4123
	0.5	0	4.1454	4.1391	8.2230	8.2124	8.2230	8.2124
		0.5	3.4817	3.4759	7.1328	7.1218	7.2908	7.2796
		1	3.2434	3.2380	6.6644	6.6537	6.8523	6.8413
		5	2.8785	2.8739	5.8265	5.8177	5.9460	5.9371
	1.0	0	3.6180	3.6122	7.1762	7.1665	7.1762	7.1665
		0.5	3.2136	3.2082	6.5056	6.4955	6.6034	6.5932
		1	3.0583	3.0531	6.2071	6.1972	6.3276	6.3175
		5	2.8080	2.8034	5.6483	5.6397	5.7313	5.7226
	5.0	0	2.8856	2.8805	5.7220	5.7133	5.7220	5.7133
		0.5	2.7815	2.7765	5.5454	5.5365	5.5694	5.5605
		1	2.7391	2.7342	5.4661	5.4573	5.4973	5.4885
		5	2.6706	2.6659	5.3192	5.3108	5.3434	5.3352
$R_x=5,R_y=\infty$ (Cylindrical)	0	0	5.6676	5.6601	11.2798	11.2679	11.2798	11.2679
		0.5	4.0679	4.0614	8.6912	8.6783	9.0408	9.0273
		1	3.5958	3.5900	7.6927	7.6803	8.0757	8.0628
		5	2.9557	2.9511	6.1022	6.0932	6.3076	6.2983
	0.5	0	4.0475	4.0413	8.0567	8.0464	8.0567	8.0464
		0.5	3.3998	3.3941	6.9917	6.9808	7.1476	7.1365

Continued on next page

			TID	TD	TID	TD	TID	TD
		1	3.1684	3.1630	6.5348	6.5242	6.7199	6.7091
		5	2.8132	2.8087	5.7147	5.7061	5.8321	5.8233
	1.0	0	3.5332	3.5275	7.0332	7.0236	7.0332	7.0236
		0.5	3.1384	3.1331	6.3777	6.3677	6.4743	6.4642
		1	2.9876	2.9825	6.0868	6.0770	6.2056	6.1957
		5	2.7439	2.7394	5.5395	5.5310	5.6210	5.6125
	5.0	0	2.8151	2.8101	5.6041	5.5955	5.6041	5.5955
		0.5	2.7174	2.7125	5.4386	5.4299	5.4623	5.4536
		1	2.6776	2.6728	5.3638	5.3551	5.3944	5.3858
		5	2.6104	2.6058	5.2185	5.2103	5.2423	5.2342

Table 5.8: Effect of gradient indexes (n_x and n_z) on buckling temperature rise ($\Delta T_{cr} = 10^{-3} \times \Delta T_{cr}$) of (Hyperbolic/Elliptic) SSSS Si_3N_4/SUS_3O_4 shell panel (a/h=5;a/b=1)

Shell geometry	n_x	n_z	Uniform		Linear		Non-Linear	
			TID	TD	TID	TD	TID	TD
R_x=5,R_y=-5 (Hyperbolic)	0	0	5.6031	5.5956	11.1969	11.1851	11.1969	11.1851
		0.5	4.0303	4.0239	8.6469	8.6339	8.9962	8.9827
		1	3.5660	3.5601	7.6592	7.6468	8.0420	8.0290
		5	2.9308	2.9263	6.0725	6.0635	6.2772	6.2679
	0.5	0	4.0038	3.9977	7.9975	7.9873	7.9975	7.9873
		0.5	3.3652	3.3595	6.9464	6.9356	7.1020	7.0909
		1	3.1373	3.1320	6.4948	6.4842	6.6794	6.6686
		5	2.7857	2.7812	5.6788	5.6702	5.7956	5.7869
	1.0	0	3.4958	3.4902	6.9837	6.9742	6.9837	6.9742
		0.5	3.1066	3.1013	6.3371	6.3271	6.4336	6.4235
		1	2.9584	2.9533	6.0498	6.0400	6.1684	6.1585
		5	2.7170	2.7125	5.5047	5.4963	5.5859	5.5774
	5.0	0	2.7842	2.7792	5.5641	5.5556	5.5641	5.5556
		0.5	2.6916	2.6868	5.4078	5.3992	5.4316	5.4229

Continued on next page

			TID	TD	TID	TD	TID	TD
		1	2.6536	2.6488	5.3360	5.3275	5.3667	5.3581
		5	2.5861	2.5815	5.1888	5.1807	5.2126	5.2047
R_x=5,R_y=2R_x	0	0	5.7301	5.7225	11.3807	11.3687	11.3807	11.3687
(Elliptic)		0.5	4.1088	4.1022	8.7600	8.7470	9.1115	9.0980
		1	3.6300	3.6241	7.7502	7.7378	8.1354	8.1224
		5	2.9829	2.9784	6.1474	6.1383	6.3541	6.3447
	0.5	0	4.0897	4.0834	8.1264	8.1160	8.1264	8.1160
		0.5	3.4348	3.4291	7.0502	7.0393	7.2069	7.1958
		1	3.2003	3.1950	6.5883	6.5777	6.7745	6.7636
		5	2.8411	2.8366	5.7611	5.7524	5.8793	5.8705
	1.0	0	3.5696	3.5639	7.0930	7.0834	7.0930	7.0834
		0.5	3.1705	3.1652	6.4307	6.4207	6.5278	6.5176
		1	3.0177	3.0126	6.1364	6.1266	6.2559	6.2459
		5	2.7713	2.7667	5.5846	5.5760	5.6667	5.6581
	5.0	0	2.8454	2.8404	5.6532	5.6446	5.6532	5.6446
		0.5	2.7446	2.7397	5.4824	5.4737	5.5063	5.4975
		1	2.7036	2.6988	5.4056	5.3969	5.4364	5.4277
		5	2.6360	2.6313	5.2599	5.2516	5.2838	5.2757

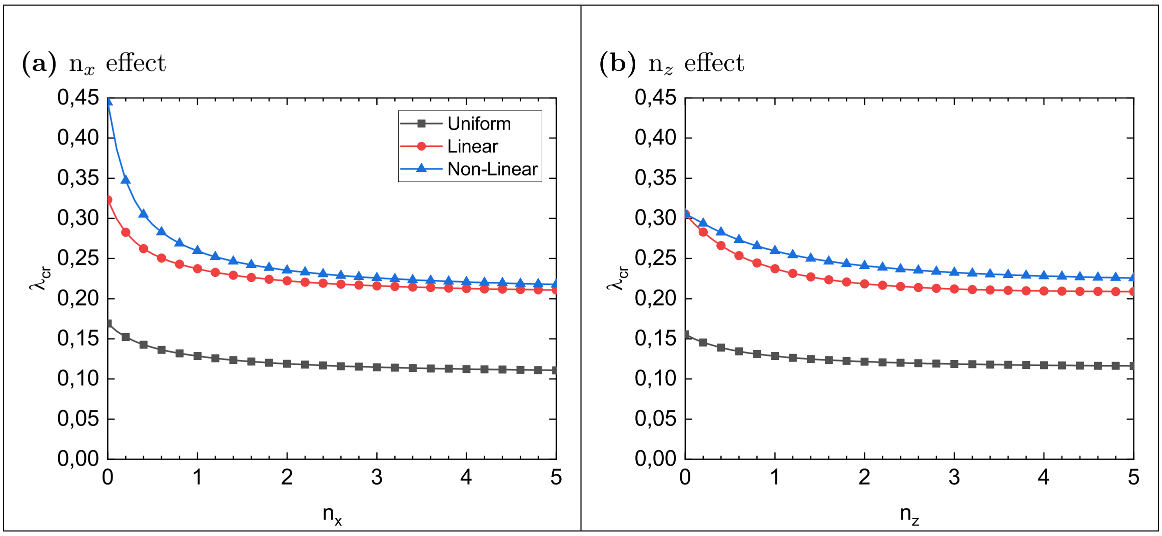

Figure 5.2: Comparison of gradient indexes effects for different temperature distributions on the buckling load parameter (λ_{cr}=$\lambda_{cr}\times10^{-3}$) of Al/$Al_2O_3$ SSSS TID spherical shell panel (R_x/a=R_y/b=5;a/b=1;a/h=2;T_t=350K;T_b=300K). (a) n_z=1. (b) n_x=1

5.3.2.2 Boundary Conditions effect on buckling temperature rise

The role of boundary conditions is paramount in determining the buckling behavior of structural elements. In the second example, three distinct boundary conditions—CFCF (clamped-free-clamped-free), CSCS (clamped-simple-clamped-simple), and CCCC (clamped-clamped-clamped-clamped)—are analyzed to assess their impact on buckling responses. The findings for each boundary condition are detailed in Table 5.9, with assumptions consistent with the previous example, including power law indexes set at $n_x = n_z = 0.5$, a thickness ratio of $a/h = 5$, and an aspect ratio of $a/b = 1$.

The results reveal a clear trend regarding buckling temperature: the CCCC boundary condition exhibits the highest buckling temperature rise, followed by the CSCS condition, and then the CFCF condition. This sequence underscores the increasing rigidity and constraint provided by these boundary conditions, which enhances the structural stability and resistance to buckling.

Moreover, the analysis indicates a notable similarity between Temperature Independent (TID) and Temperature Dependent (TD) materials, with TID materials consistently demonstrating higher buckling temperature values than their TD counterparts. This suggests that the assumption of temperature independence may yield more pronounced estimates in certain scenarios.and the discrepency between those two assumption is expected to be more significant for larger temperature change.

In terms of temperature distribution effects, the non-linear temperature distribution scheme yields the highest buckling temperature values, followed by the linear and uniform distributions. The substantial gap observed between the uniform temperature distribution and the other two distributions emphasizes the limitations of assuming uniform thermal conditions, which may not accurately reflect real-world situations. This trend is consistent across all examined shell panel geometries, reinforcing the critical nature of considering realistic temperature distributions in buckling analyses.

Figure 5.3 further illustrates similar findings under varying conditions, providing a visual representation of the data. Detailed assumptions guiding the generation of this data are outlined in the caption, facilitating a comprehensive understanding and comparison of results. Additionally, two asymmetric boundary conditions, CCFF (clamped-clamped-free-free) and CCSS (clamped-simple-simple-simple), are incorporated into the analysis. Notably, under these conditions, the buckling load parameter remains relatively unchanged with varying n_x values for both the CCSS and CSCS boundary conditions.

In scenarios involving a non-linear temperature distribution, the three boundary condition configurations—CCCC, CCSS, and CSCS—demonstrate closely aligned results for $n_x > 0.2$. This observation suggests that, beyond a certain gradient index threshold, the influence of boundary conditions on the buckling response becomes less pronounced, highlighting the need for further investigation into the interplay between boundary conditions, material properties, and geometric configurations in future studies.

Table 5.9: Effect of boundary conditions on buckling temperature rise ($\Delta T_{cr} = 10^{-3} \times \Delta T_{cr}$) of Si_3N_4/SUS_3O_4 doubly cuved shell panel ($n_x = n_z = 0.5; a/h = 5; a/b = 1$)

Shell geometry	BC	Uniform		Linear		Non-Linear	
		TID	TD	TID	TD	TID	TD
R_x=R_y=5	CCCC	6.7595	6.7482	13.8791	13.8574	14.1894	14.1672
(Spherical)	CSCS	5.2780	5.2694	10.7982	10.7820	11.0146	10.9981
	CFCF	3.1264	3.1216	6.2365	6.2278	6.3012	6.2925
R_x=5,R_y=∞	CCCC	6.6720	6.6608	13.7403	13.7188	14.0488	14.0269
(Cylindrical)	CSCS	5.1888	5.1804	10.6468	10.6309	10.8619	10.8457
	CFCF	3.0945	3.0897	6.1982	6.1896	6.2632	6.2545
R_x=5,R_y=-5	CCCC	6.7030	6.6917	13.8431	13.8214	14.1545	14.1324
(Hyperbolic)	CSCS	5.2377	5.2291	10.7737	10.7575	10.9907	10.9742
	CFCF	3.1281	3.1233	6.2888	6.2801	6.3545	6.3458
R_x=5,R_y=2R_x	CCCC	6.7011	6.6898	13.7799	13.7583	14.0887	14.0667
(Elliptic)	CSCS	5.2162	5.2077	10.6880	10.6720	10.9034	10.8871
	CFCF	3.1023	3.0976	6.2013	6.1927	6.2661	6.2575

5.3.2.3 Aspect-Ratio Effect On Buckling Temperature Rise

In the following example, we will explore the impact of the aspect ratio while maintaining fixed gradient indices ($n_x = n_z = 0.5$). The analysis is conducted under SSSS boundary conditions, with the aspect ratio varying from 1 to 4. The results, summarized in Table 5.10, reveal a significant trend: as the aspect ratio (a/b) increases, there is a corresponding rise in the buckling temperature.

Furthermore, the shell panel demonstrates distinctly higher values for non-linear temperature distributions, followed by linear distributions, and finally uniform temperature distributions. This aligns with previous findings, indicating that Temperature Independent (TID) properties yield greater buckling temperature increases than Temperature Dependent (TD) properties. This pattern is consistent across various geometrical configurations, suggesting a robust relationship between aspect ratio and buckling behavior.

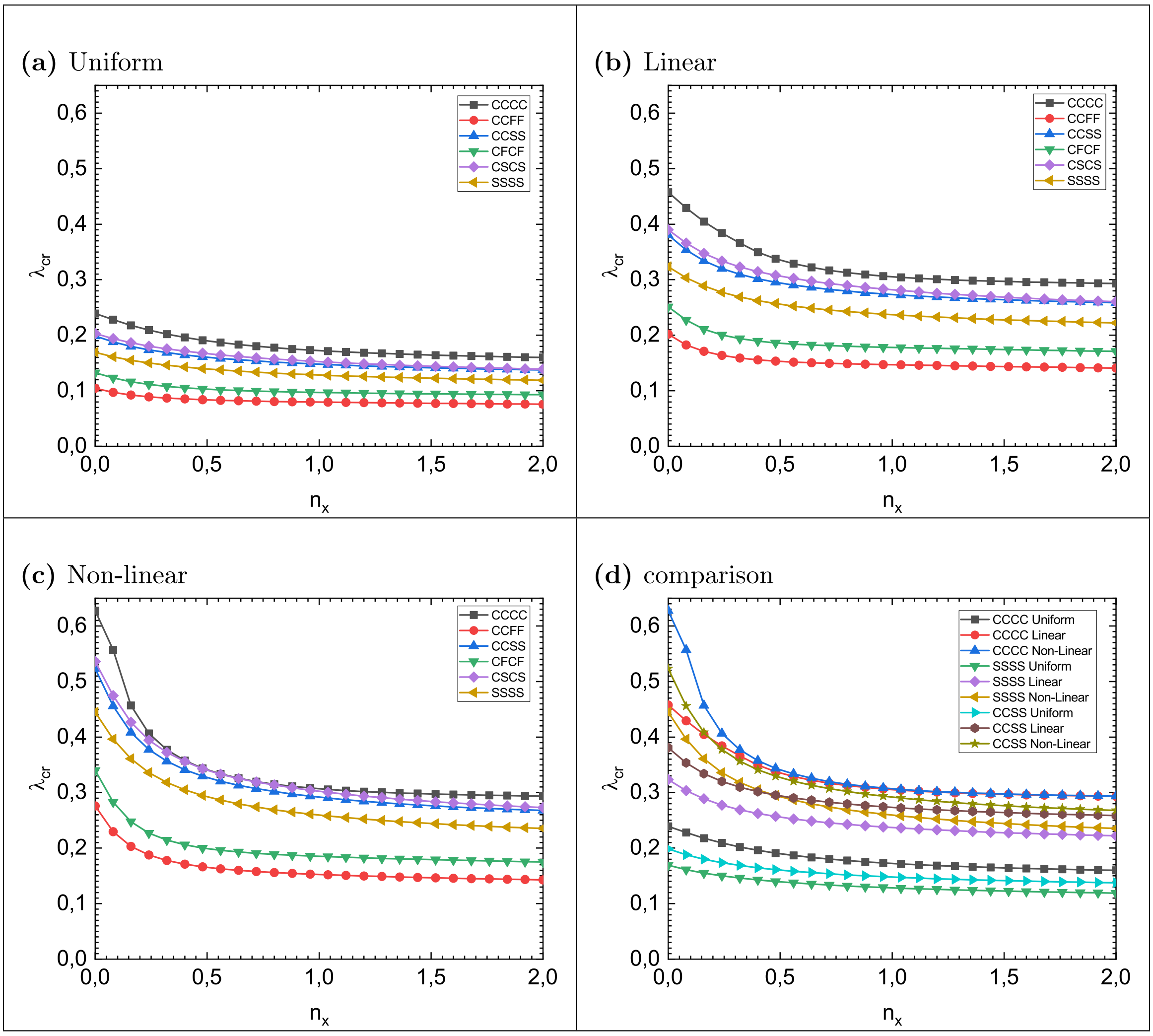

Figure 5.3: Comparison of different boundary conditions effects on the buckling load parameter $\lambda_{cr} = \lambda_{cr} \times 10^{-3}$ of Al/Al_2O_3 SSSS TID spherical shell panel (R_x/a=R_y/b=5;a/b=1;a/h=2;T_t=350K;T_b=300K,n_z=1)

The insights from Table 5.10 pave the way for a more detailed investigation depicted in Figure 5.4, which illustrates the results for a spherical shell panel with the ratios $R_x/a = R_y/b = 5$. This figure delves into the effects of gradient indices and aspect ratio (a/b) on the buckling load parameter across different temperature distributions ($n_z = 0.5$, $h/a = 0.2$).

As illustrated, Figure 5.4 effectively visualizes the trends identified in Table 5.10, emphasizing the exponential variation in the buckling load parameter. Notably, the non-linear and linear temperature distributions consistently yield higher values compared to the uniform temperature distribution, underscoring the importance of temperature profiles in influencing the structural integrity of shell panels. These findings not only enhance our understanding of buckling behavior but also inform future design considerations for structures subjected to varying thermal conditions.

Table 5.10: Effect of aspect ratio on buckling temprature rise ($\Delta T_{cr} = 10^{-3} \times \Delta T_{cr}$) for Si_3N_4/SUS_3O_4 SSSS shell panels ($n_x = n_z = 0.5; a/h = 5$)

Shell geometry	a/b	Uniform		Linear		Non-Linear	
		TID	TD	TID	TD	TID	TD
R_x=R_y=5	1	3.4817	3.4759	7.1328	7.1218	7.2908	7.2796
	2	6.4972	6.4864	13.2936	13.2730	13.5641	13.5432
	3	9.3123	9.2970	18.9245	18.8957	19.2390	19.2098
	4	11.3251	11.3067	21.8963	21.8642	21.9189	21.8868
R_x=5,R_y=∞	1	3.3998	3.3941	6.9917	6.9808	7.1476	7.1365
	2	6.4783	6.4675	13.3371	13.3165	13.6099	13.5889
	3	9.3031	9.2878	19.0013	18.9725	19.3172	19.2879
	4	11.3192	11.3008	21.8964	21.8643	21.9190	21.8869
R_x=5,R_y=-5	1	3.3652	3.3595	6.9464	6.9356	7.1476	7.1365
	2	6.4585	6.4477	13.3796	13.3589	13.6099	13.5889
	3	9.2922	9.2769	19.0748	19.0459	19.3172	19.2879
	4	11.3118	11.2934	21.8964	21.8644	21.9190	21.8869
R_x=5,R_y=2R_x	1	3.4348	3.4291	7.0502	7.0393	7.2069	7.1958
	2	6.4878	6.4770	13.3155	13.2949	13.5871	13.5661
	3	9.3079	9.2926	18.9633	18.9345	19.2785	19.2493

Continued on next page

	TID	TD	TID	TD	TID	TD
4	11.3223	11.3039	21.8963	21.8642	21.9190	21.8869

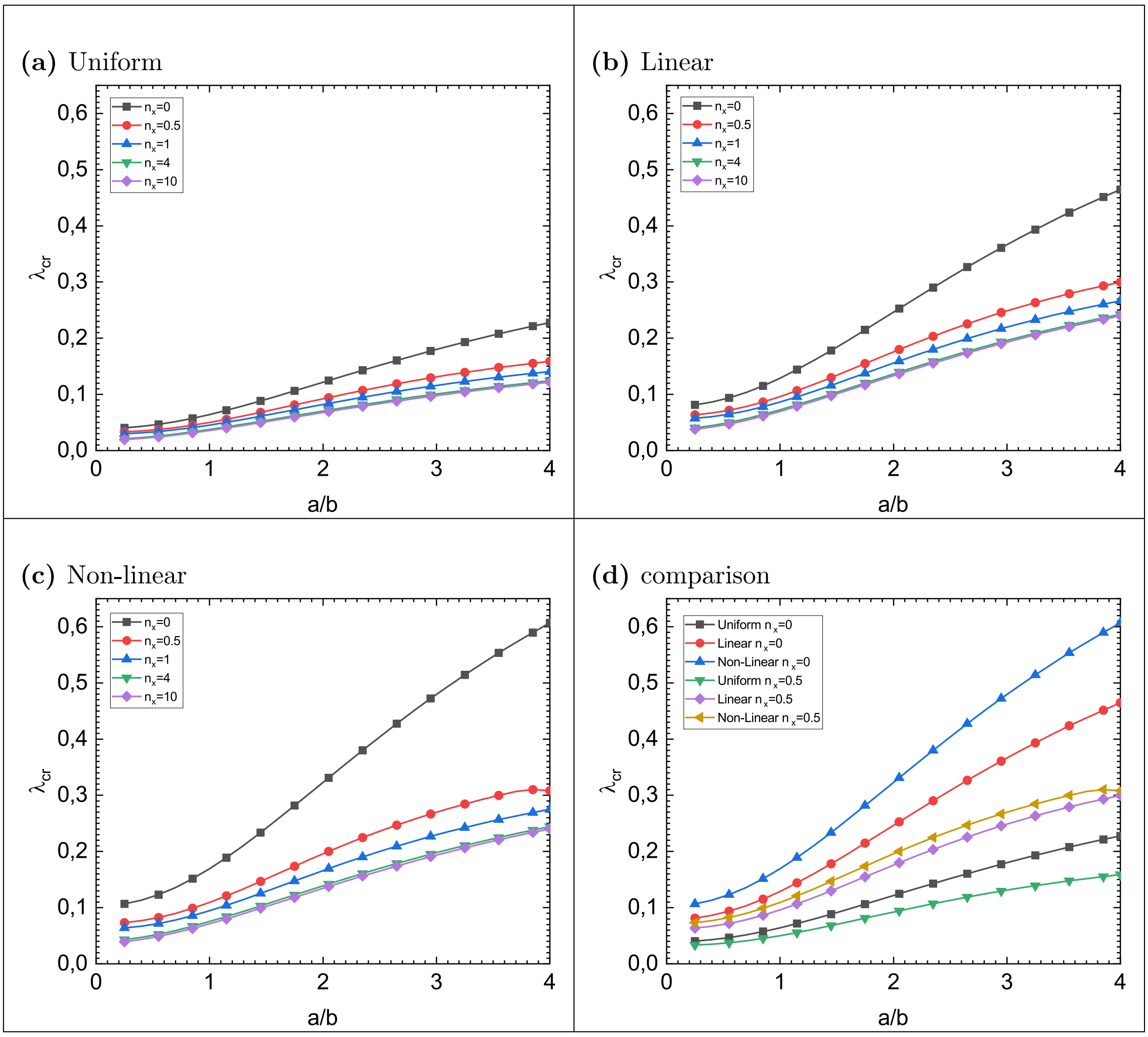

Figure 5.4: Effect of gradient index n_x and aspect ratio (a/b) on the buckling load parameter for different temperature distributions of an SSSS TID Al/Al_2O_3 spherical shell panel ($R_x/a = R_y/b = 5, h/a = 0.2, a/b = 1, n_z$=0.5, $T_t = 350K, T_b = 300K, \lambda_{cr} = \lambda_{cr} \times 10^{-3}$)

5.3.2.4 Gradient indexe n_x effect on Buckling Mode Shape

Figure 5.5 illustrates the first four buckling mode shapes of a spherical shell panel (R_x/a = R_y/b = 10) constructed from a bi-directional Functionally Graded Material (bi-FGM) composed of Al/Al_2O_3. The panel is characterized by a thickness ratio of h/a = 0.25 and an aspect ratio of a/b = 1. A Temperature-Independent (TID) material model is employed, with the CSCS boundary conditions (clamped at the bottom, right, top, and left edges) applied under a uniform temperature distribution. The temperature settings are defined with the top layer at T_t = 350K and the bottom layer at T_b = 300K, and gradient indices are maintained at n_x = n_z = 0.5, as illustrated in the accompanying contour plots.

The mode shapes reveal symmetrical characteristics at y/b = 0.5, yet they exhibit marked asymmetry in the x-direction. This observation suggests that while the shell panel maintains some symmetrical properties, the material gradation leads to deviations influenced by the geometric and thermal conditions. The figures on the right depict the evolution of normalized deflection with varying n_x. Notably, as the gradient index increases—indicating a higher proportion of metallic material—the maximum deflection tends to shift towards the center of the shell panel for the first and third mode shapes. This shift reflects a trend toward symmetry similar to that observed in isotropic shell panels.

However, experimental results indicate that the entire mode shape may undergo significant changes for specific n_x values, with the first mode shape remaining consistently unchanged regardless of these variations. This stability of the first mode shape is particularly noteworthy, as it provides a reliable reference for comparative analysis. The selection of these boundary conditions was specifically designed to mitigate such behavior, facilitating a more accurate comparison of maximum deflection across multiple scenarios. Overall, this investigation highlights the complex interplay between material gradation, boundary conditions.

In Figure 5.6, contour plots illustrate a SSCC spherical shell panel, maintaining the same context as the previous example. In this analysis, the gradient index n_z is held constant at 0.5, while n_x varies from zero to infinity. These plots clearly demonstrate the significant impact of boundary conditions on the behavior of the shell panel, indicating that the maximum deflection for the first mode shape is ideally positioned at the center of the panel. However, this expected behavior is not observed due to the constraints imposed by the specified boundary conditions.

As seen in the previous example, the same mode shape occurs at both n_x = 0 and n_x = ∞, suggesting a threshold where the effects of the gradient index become negligible. However, as n_x continues to vary, the shape of the panel undergoes noticeable changes, highlighting the intricate relationship between boundary conditions and gradient index in determining the mode shape during thermal buckling.

The analysis of these two examples leads to a crucial conclusion: both gradient indexes and boundary conditions are vital in shaping the buckling mode of the shell panel. Understanding this dynamic interplay is essential for predicting and optimizing the structural

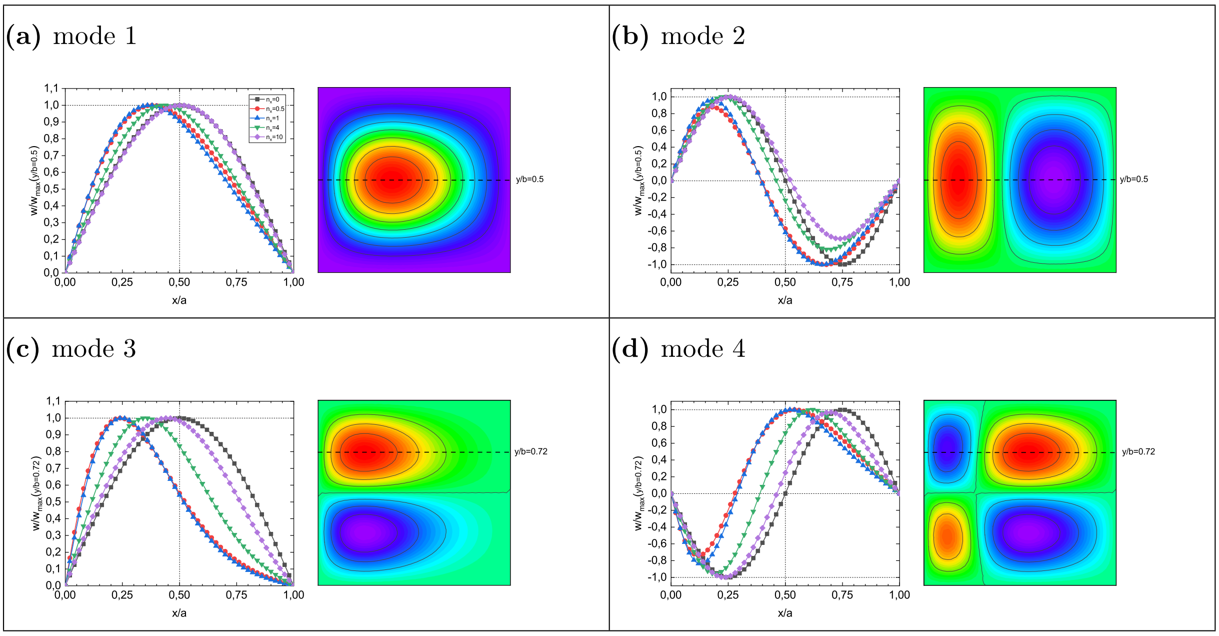

Figure 5.5: Effect of gradient index n_x on the buckling mode shapes of a TID Al/Al_2O_3 CSCS Spherical shell panel under uniform temperature distribution, ($T_t = 350K, T_b = 300K, R_x/a = R_y/b = 10, h/a = 0.25, a/b = 1, n_z$=0.5). (for contour plots $n_x = n_z = 0.5$)

behavior of functionally graded materials under varying thermal conditions. This insight contributes to more effective design strategies for applications involving thermal stresses and buckling phenomena.

5.3.2.5 Thickness Ratio and Temperature Distribution Effect On Buckling Load Parameter

Figure 5.7 explores the effects of both thickness ratio and gradient index (n_x) on the buckling load parameter of a spherical shell panel subjected to various temperature distributions. The shell is made from a bi-directional Functionally Graded Material (FGM) consisting of Al/Al_2O_3 (TID), with a fixed gradient index of $n_z = 0.5$ and fully simply supported boundary conditions (SSSS). In this analysis, the aspect ratio is maintained at $a/b = 1$.

The findings reveal consistent patterns with previous observations: a uniform temperature distribution leads to a lower buckling temperature rise when compared to both linear and non-linear temperature distributions. Interestingly, the latter two distributions exhibit similar behavior, highlighting their comparable effects on the buckling response of the panel.

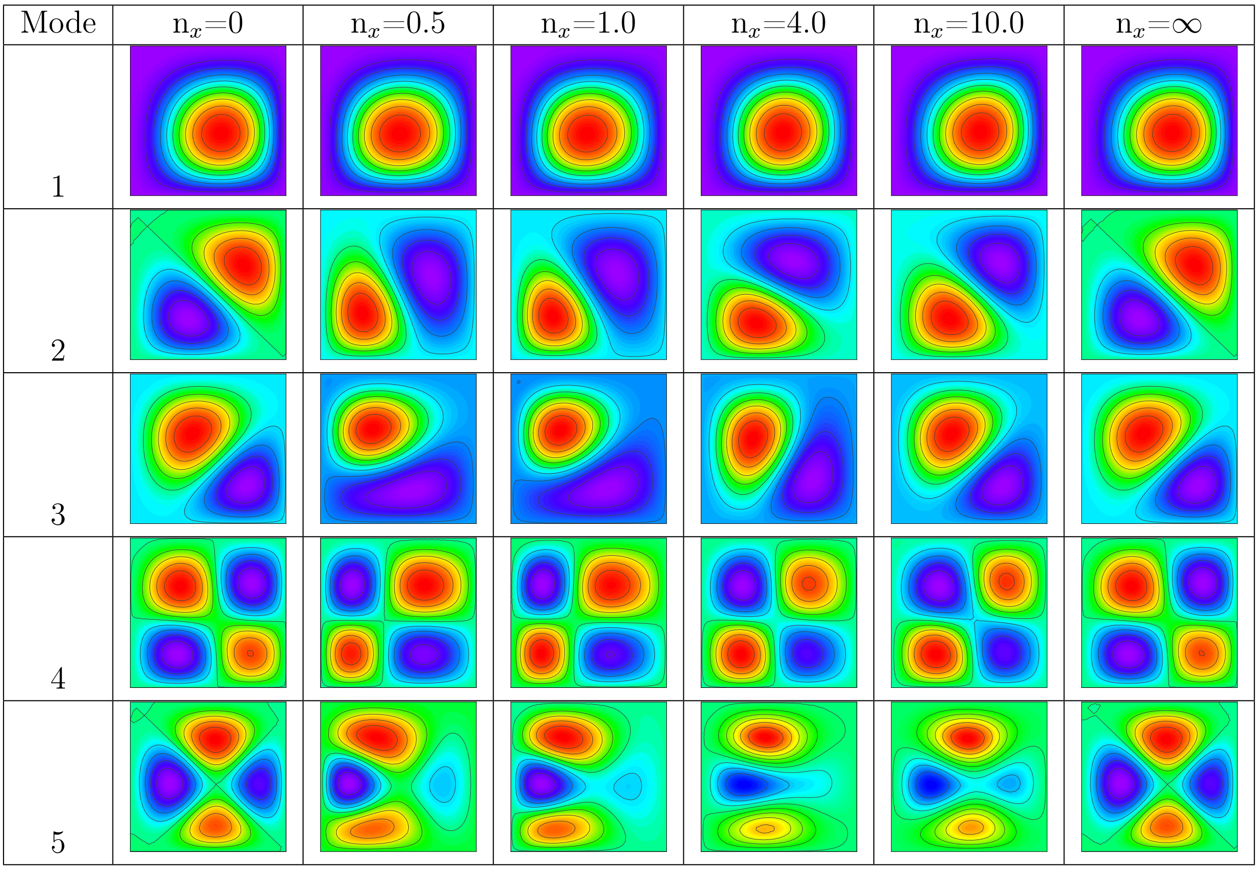

Figure 5.6: Effect of gradient index n_x on the buckling mode shapes of a TID Al/Al_2O_3 SSCC Spherical shell panel under uniform temperature distribution n_z=0.5, (T_t=350K,T_b=300K,R_x/a=R_y/b=5,h/a=0.2,a/b=1)

Furthermore, the influence of the gradient index n_x is notably minimal for thinner shells. However, as the thickness of the shell increases, the role of n_x becomes significantly more pronounced. This suggests that thicker shells are more sensitive to variations in the gradient index, which may affect their structural performance under thermal loading.
Moreover, for n_x values exceeding 4, the impact of the gradient index appears to plateau, indicating a diminishing effect on the buckling response. The plot illustrates that both $n_x = 4$ and $n_x = 10$ display nearly identical trends, reinforcing the notion that beyond a certain threshold, increasing the gradient index does not yield substantial changes in the buckling load parameter.

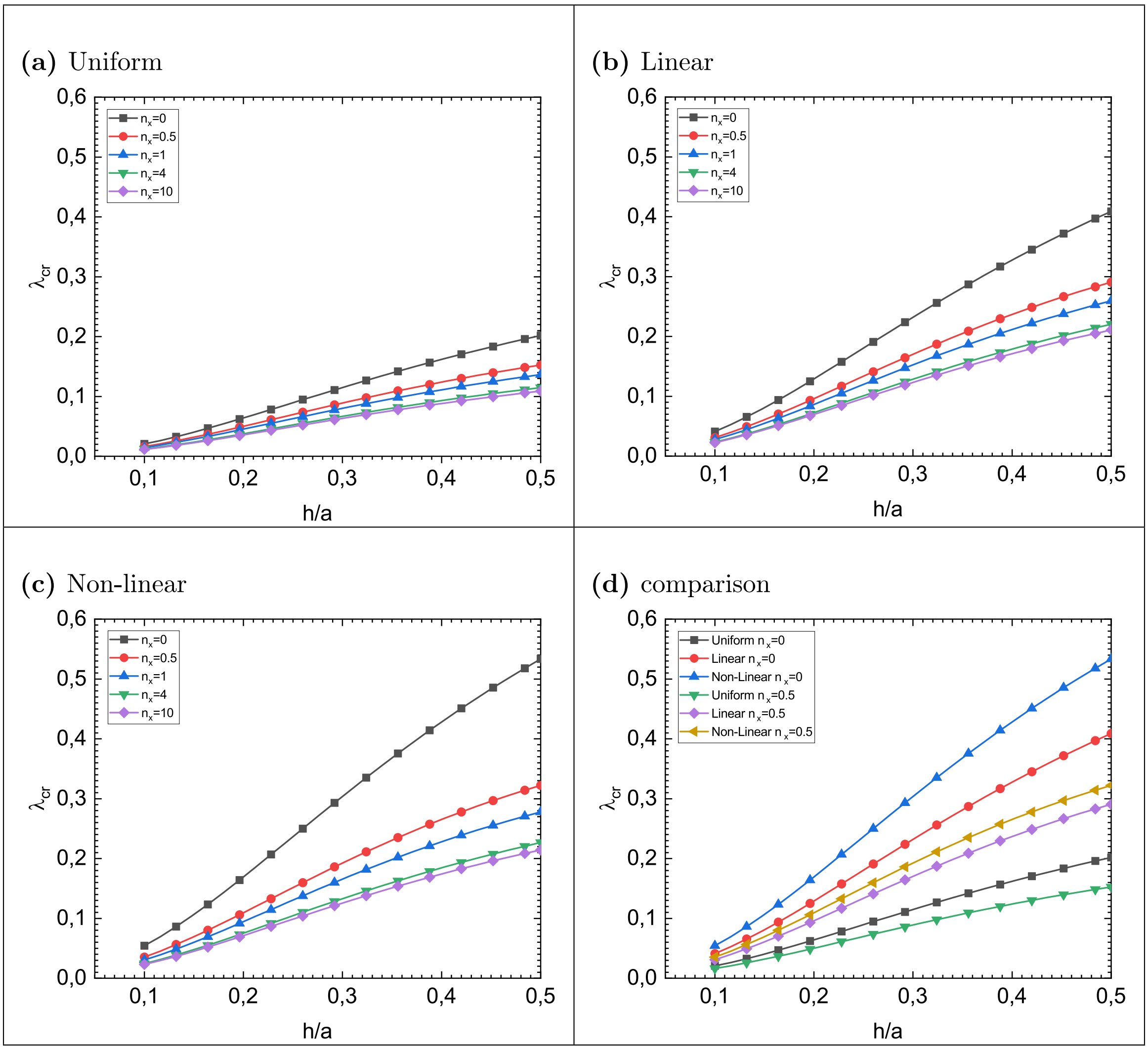

Figure 5.7: Effect of gradient index n_x and thickness ratio (h/a) on the buckling load parameter for different temperature distributions of an SSSS TID Al/Al_2O_3 spherical shell panel ($R_x/a = R_y/b = 5, a/b = 1, n_z = 0.5, T_t = 350K, T_b = 300K, \lambda_{cr} = \lambda_{cr} \times 10^{-3}$)

5.3.2.6 Mixture Bi-Directionality Effect on Normalized Stress Distribution

In this example, the normalized modal stress distribution in the xz-plane for the first buckling mode shape of an isotropic spherical shell is compared to that of a bi-directional Functionally Graded Material (bi-FGM) shell panel composed of Al/Al_2O_3 (see Figure 5.8). The key parameters are defined as follows: thickness ratio (a/h = 5), aspect ratio (a/b = 1), and radius of curvature (R_x/a = R_y/b = 5). The isotropic shell represents a fully ceramic panel with gradient indices set to ($n_x = n_z = 0$), whereas for the bi-directional FGM shell, the gradient indices are set to ($n_x = 0.5$) and ($n_z = 1$).
The boundary conditions applied are fully simply supported (SSSS), and the stress components are evaluated at the critical plane, where maximum values have been recorded. Specifically, for (σ_{xx}), (σ_{yy}), and (τ_{xz}), the stresses are measured at (y/b = 0.5), while (τ_{xy}) and (τ_{yz}) are evaluated at (y/b = 0.0).
In the case of the isotropic spherical shell, a symmetrical stress distribution is observed for (x/a = 0.5). However, for (z/h = 0.0), symmetry is maintained only in the shear stress components (τ_{xz}) and (τ_{yz}), while normal stress components (σ_{xx}) and (σ_{yy}), as well as the shear stress (τ_{xy}), exhibit a shift in the neutral plane due to the shell's inherent curvature. This shift underscores the influence of curvature on stress distribution, even in isotropic materials.
In contrast, the bi-directional functionally graded shell panel exhibits a stress distribution pattern that, while similar to the isotropic case, lacks symmetry. The absence of symmetry in the bi-FGM shell is attributed to the variation in material properties along both the x and z directions, resulting from the gradient indices. Additionally, the points of maximum stress values are displaced in the bi-FGM shell compared to the isotropic one. This shift is indicative of the bi-directional material's response to external loads and thermal effects, which causes stress concentrations to occur in different regions.

5.3.2.7 Thickness and Gradient index Effect on Nomarlized Modal Stress Distribution

Figure 5.9 examines the influence of the gradient index (n_z) on the normalized modal stress distribution through the thickness of a simply supported (SSSS) flat shell panel. Two different thickness ratios are compared: $a/h = 2$ and $a/h = 10$. The material is a temperature-independent (TID) Al/Al_2O_3 composite, and the analysis is performed under uniform temperature distribution for the first buckling mode shape. The stress distributions are normalized to their maximum values at specific locations, denoted in parentheses as coordinates (x/a, y/b).

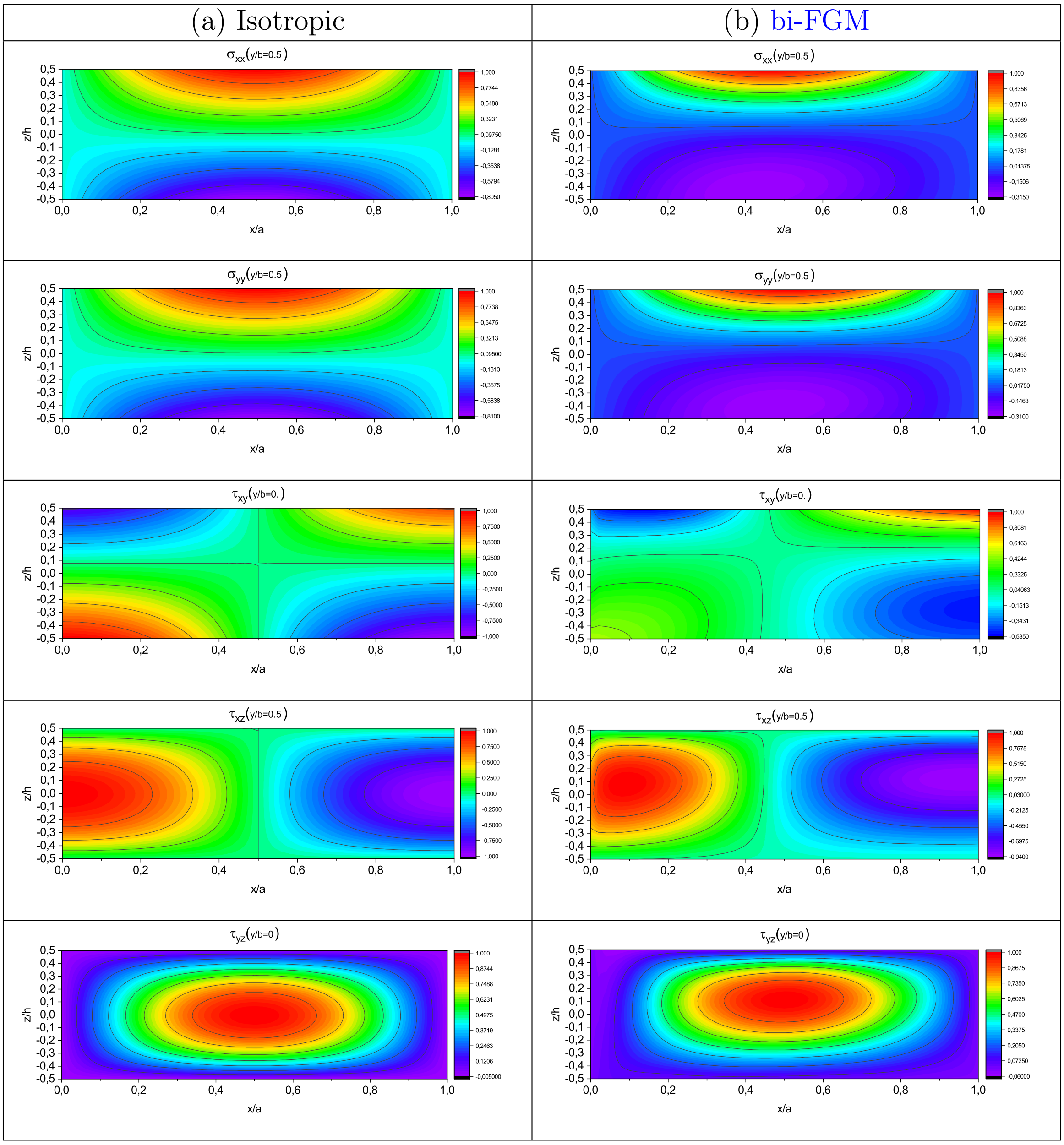

Figure 5.8: Comparison of Normalized modal Stress distribution in xz plane for isotropic versus a bi-directional SSSS TID Al/Al_2O_3 spherical shell panel under linear temperature distribution $(a/h = 5, a/b = 1, R_x/a = R_y/b = 5, T_b = 300K, \Delta T = 1°\text{C}, \sigma_{xx}(y/b = 0.5), \tau_{xz}(y/b = 0.5), \tau_{xy}(y/b = 0.0))$. (a) $\mathrm{n}_x = n_z = 0$. (b) $\mathrm{n}_x = 0.5, n_z = 1$

The plotted stresses include:

- **Shear stress** τ_{xz} for (x/a = 0, y/b = 0.5),
- **Normal stress** σ_{xx} for (x/a = 0.5, y/b = 0.5), and
- **Shear stress** τ_{xy} for (x/a = y/b = 0).

These stress components are crucial for understanding how buckling-induced stresses vary across the shell thickness for panels of differing thicknesses and gradient indexes.
The figure clearly shows that σ_{xx} and τ_{xy} exhibit similar stress patterns for both thin and thick panels, with some notable distinctions. For isotropic shells ($n_z = 0$), the stress distribution across the thickness is symmetrical. In thinner shells (a/h = 10), this distribution is nearly linear, with compressive stress on one face and tensile stress on the opposite face. However, in thicker shells (a/h = 2), the stress distribution becomes more nonlinear, indicating the increased influence of the panel's thickness on how stress develops and redistributes under buckling conditions.
For the shear stress τ_{xz}, both isotropic ($n_z = 0$) and highly graded ($n_z = 10$) panels show the maximum stress occurring at or near the neutral plane of the panel (z/h = 0), especially in thicker panels. This indicates that, despite the gradient in material properties, the neutral plane remains a significant stress-bearing location. A limitation of the present model is the small but non-zero shear stress predicted at the panel's top and bottom surfaces, which is more pronounced in thicker panels (a/h = 2). While this is acknowledged as a theoretical constraint, it remains an acceptable approximation for the stress distribution, especially in moderately thick panels where the stress behavior is more predictable.
For normal stress σ_{xx} and shear stress τ_{xy}, thicker panels (a/h = 2) show a nonlinear stress variation, while thinner panels (a/h = 10) display a more linear pattern. This behavior can be attributed to the increased stiffness of thicker panels, which resist deformation more unevenly, resulting in larger stress gradients across the thickness. Additionally, symmetric stress patterns are observed in the isotropic case, where one face of the panel is in tension and the other in compression. However, for functionally graded materials (FGMs) with non-zero gradient indexes ($n_z \neq 0$), symmetry is lost. In these cases, the stress concentration shifts towards the top surface (z/h = 0.5), where the material properties have been altered by the gradient, leading to an asymmetric stress response.
In summary, this figure highlights how both gradient index and thickness ratio impact the stress distribution within shell panels. While thinner panels exhibit more linear, symmetrical stress distributions, thicker panels demonstrate nonlinearity and asymmetry, particularly when FGM properties are introduced.

Figure 5.10 presents a similar stress analysis for a spherical shell panel as previously

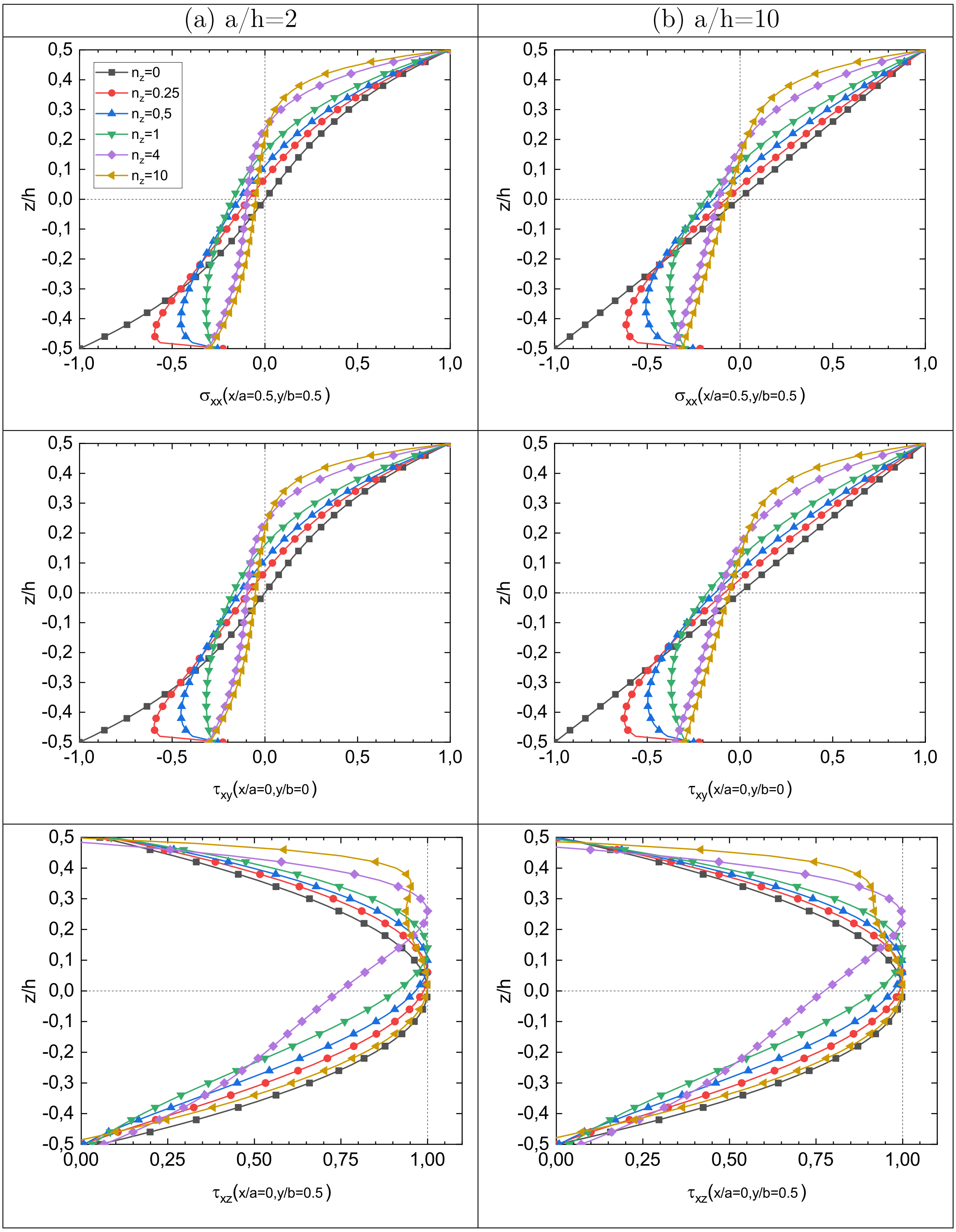

Figure 5.9: Comparison of Normalized modal Stress variation across the thickness of a TID (Uniform temperature distribution) Al/Al_2O_3 SSSS square plate for different thickness ratios;n_x=0(unidirectional FGM)

performed for a flat shell, but with the curvature characterized by ($R_x/a = R_y/b = 5$). The study considers a bi-directional functionally graded material (FGM) with a gradient index of $n_x = 1$, and the material is subjected to a linear temperature distribution (TID) under a small uniform temperature increase of $\Delta T = 1°C$. The thickness ratio of the shell panel is set at $a/h = 5$, allowing for a comparison of stress distribution patterns with those observed in flat panels.

The locations of the maximum stress concentrations are indicated in parentheses in the legend for each stress component.

One of the key differences from the flat panel analysis is that, in this spherical shell configuration, material gradation results in stress shifts occurring not only in the z-direction (through the thickness) but also in the x-direction (along the curvature). This distinction stems from the geometric curvature of the shell, which introduces an additional dimension of stress variation. The effect of the gradient indices (n_x and n_z) is pronounced, particularly in influencing the stress concentrations at specific regions of the shell.

For the shear stress τ_{xz} (Figure 5.10.a), the stress distribution across the shell thickness remains nonlinear, similar to the flat panel case, but the curvature alters the stress gradient slightly. The stresses are more concentrated towards the mid-plane ($z/h = 0$), especially for higher gradient indices ($n_z = 10$). This behavior is more noticeable compared to the flat panel, where stress concentration was more uniform across the shell thickness.

In shear stress τ_{xy} (Figure 5.10.b), the gradient index significantly impacts stress concentration near the top surface of the shell. As n_z increases, the stress distribution becomes more nonlinear, with the maximum shear stress occurring close to the outer surface ($z/h = 0.5$). The curvature of the shell panel intensifies the stress concentration compared to a flat panel, emphasizing the role of geometric properties in determining the stress behavior.

For normal stress σ_{xx} (Figure 5.10.c), the pattern remains similar to that of a flat panel, with compressive stresses at one face and tensile stresses at the other. However, the presence of curvature shifts the point of maximum stress along the x-direction, especially for larger gradient indices ($n_z = 4$ and $n_z = 10$). This shift indicates that the shell's geometry and material gradation work together to concentrate stress at specific locations, highlighting the complex interaction between geometry and material properties in FGM shell structures.

In Figure 5.11, a detailed investigation into the effects of the gradient index n_x and the shell geometry on the normalized axial stress distribution σ_{xx} across the shell's thickness is presented. The analysis was performed consistently at the mid-plane of the shell, with coordinates set at ($x/a = 0.5$, $y/b = 0.5$). This location is representative of the mid-section, where significant stress concentrations typically occur in shell structures under thermal and mechanical loading.

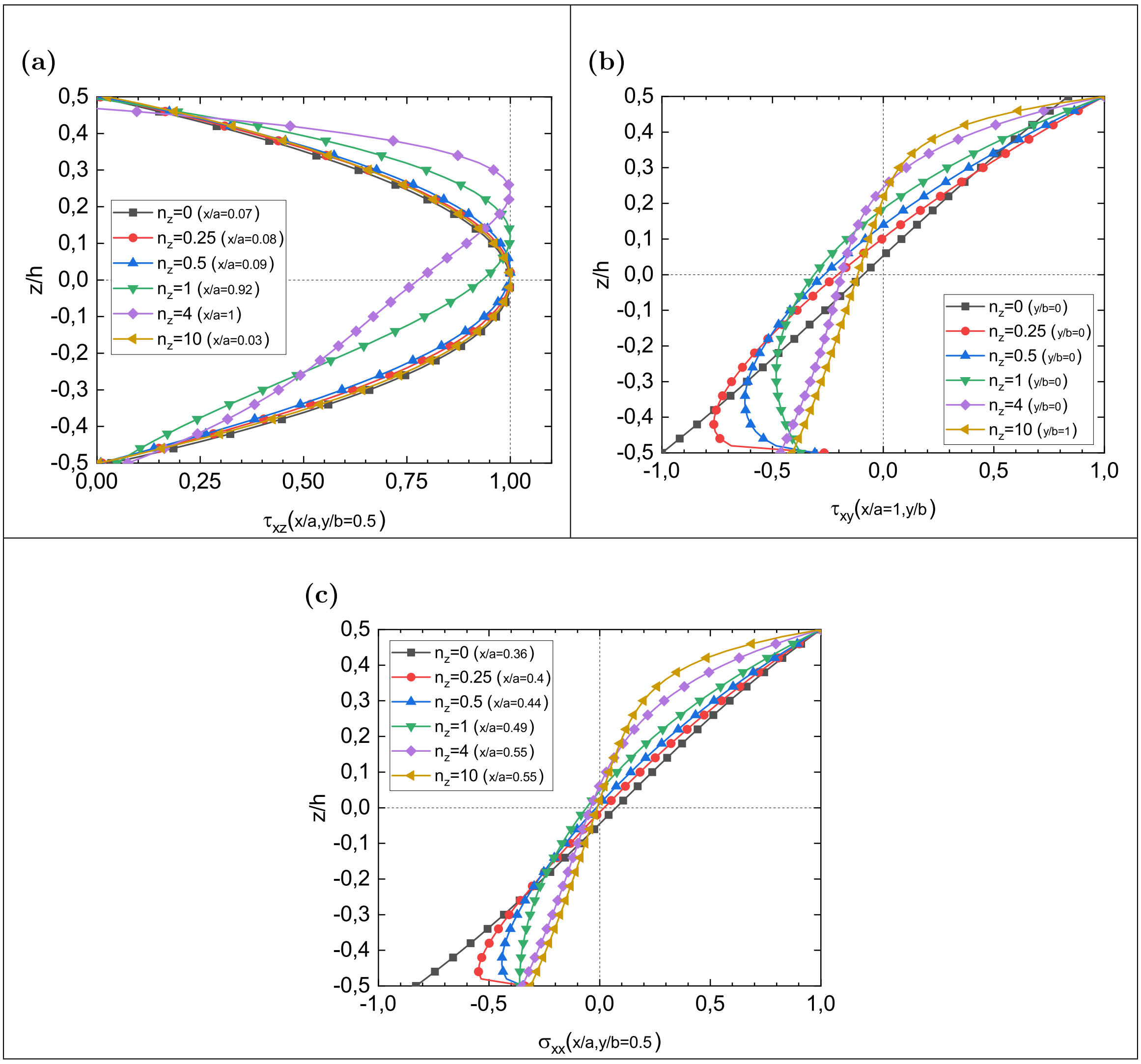

Figure 5.10: Gradient index effect on normalized modal stress distribution across the thickness of Al/Al_2O_3 SSSS TID spherical shell panel under linear temperature distribution (R_x/a=R_y/b=5;a/h=5;a/b=1;n_x=1)

The results highlight a critical observation regarding the shift in the position of maximum stress with varying values of n_x. As expected, in the isotropic case ($n_x = 0$) for all geometries, the maximum stress consistently occurs at the mid-plane of the shell panel (z/h = 0). However, as the material becomes more functionally graded (with increasing n_x), the location of the maximum stress shifts towards the outer surfaces of the shell, particularly for higher values of n_x. This shift reflects the influence of the gradation on the material properties, where the stress distribution changes due to the increasing dominance of the stiffer material components, particularly on the outer layers.
A noteworthy aspect of the analysis is the modification applied to some stress values for comparison purposes. In cases where the maximum modal stress on the bottom surface of the shell is negative, the value has been multiplied by -1 to maintain consistency across the figures. This adjustment ensures that the comparisons between different geometries and gradient indices are meaningful, as the sign of the stress in modal analysis does not carry physical significance. Instead, the focus is on the proportional variations in stress distribution due to the gradient index and shell geometry.
Across the five geometries studied— (a) Plate, (b) Spherical, (c) Cylindrical, (d) Elliptical, and (e) Hyperbolic—there is a clear and consistent trend in the behavior of the normalized axial stress ldistribution. For lower gradient index values ($n_x = 0$ to $n_x = 1$), the stress distributions show nonlinear characteristics, particularly in the spherical and hyperbolic cases. This nonlinear behavior is indicative of the increased influence of the softer material phase in functionally graded shells with lower n_x, leading to a more complex stress distribution through the thickness.
For higher gradient index values ($n_x \geq 4$), a linearized stress distribution is observed across all geometries. This linear behavior is primarily due to the increased metallic content in the material, particularly in cases with $n_x = 4$ and $n_x = 10$, where the material approaches isotropic properties. The dominance of the metallic phase in the functionally graded material leads to stress distribution patterns that closely resemble those of isotropic panels, with a more uniform and predictable variation across the thickness of the shell.
The results also emphasize the role of shell geometry in influencing the stress concentration and distribution. While the plate geometry exhibits the most straightforward linear behavior, the spherical and cylindrical geometries introduce curvature effects that lead to more complex stress variations, especially at lower gradient index values. The elliptical and hyperbolic geometries show intermediate behavior, where the curvature is less pronounced but still affects the stress distribution.
In conclusion, this analysis demonstrates that both the gradient index n_x and the shell geometry have a significant impact on the axial stress distribution. The results provide

insights into how functionally graded materials behave in different geometrical configurations and highlight the importance of selecting appropriate gradient indices for optimizing stress distribution in shell structures under thermal and mechanical loads.

5.4 Optimization Remark

In thermal buckling analysis, optimizing the structure involves maximizing the critical buckling load (λ_{cr}), which represents the thermal load at which instability occurs. A higher λ_{cr} enhances the structure's ability to withstand greater thermal stresses, improves safety by delaying the onset of buckling, and increases the overall stability of the system. By optimizing the design to maximize λ_{cr}, material usage is made more efficient while ensuring that the structure remains reliable and durable in high-temperature environments.

5.4.1 Optimization of Gradient indexes effect

The results reveals several important optimization insights regarding the effect of gradient indexes n_x and n_z on the buckling temperature rise for bi-FGM doubly curved shell panels under various temperature distributions (uniform, linear, and non-linear) and both TD and TID cases. A general trend is observed where increasing n_x and n_z leads to a decrease in the buckling temperature rise across all scenarios, suggesting that lower values of n_x and n_z(meaning ceramic dominant structure) could enhance thermal buckling resistance. However, it is crucial to recognize that these temperature distributions and material behaviors (TD and TID) are assumptions made for analytical purposes. In practice, the actual temperature variation and material response might differ, and it is not certain which assumption is closest to real-world conditions. For instance, the non-linear temperature distribution generally results in the highest buckling temperature rise in this analysis, indicating better thermal stability in theory, while the uniform distribution tends to produce the lowest values, suggesting greater thermal instability. Yet, in reality, the exact temperature distribution and the precise behavior of materials under thermal loads may be more complex and uncertain. Similarly, while the analysis shows that the TD case tends to result in slightly lower buckling temperature rise compared to TID, the true extent of temperature dependency in materials may vary. As a result, these findings provide a useful framework for optimization, but further investigation and experimental validation are required to understand which assumptions align with real-world conditions. Ultimately, the goal should be to design for the worst-case scenarios, considering uncer-

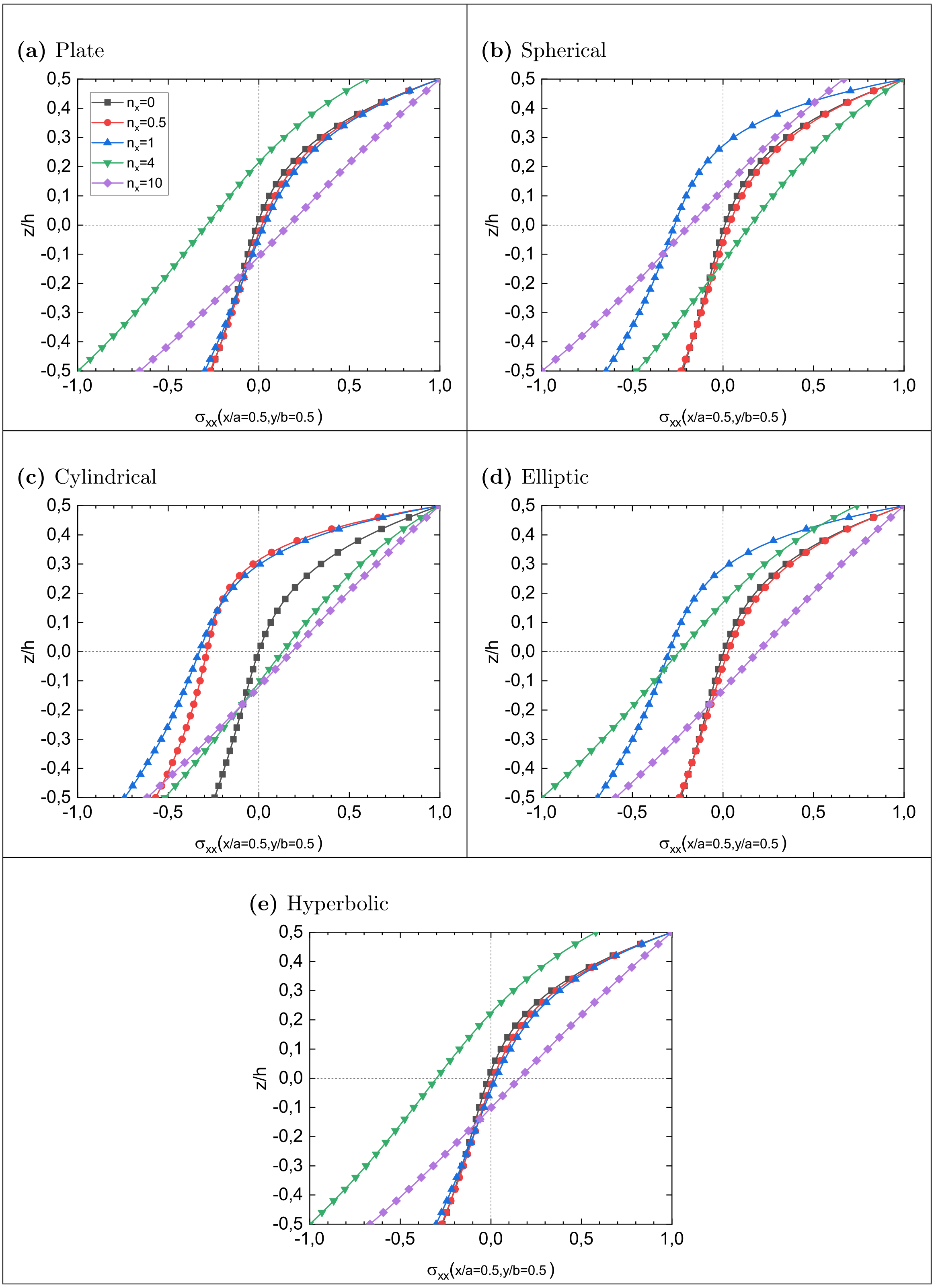

Figure 5.11: effect of n_x variation on normalized axial Stress σ_{xx} across the thickness of SSSS Al/Al_2O_3 shell panel (n_z=4;T_t=350K;T_b=300K linear temperature distribution TID;a/h=5;a/b=1). (a) $R_x/a=R_y/b=\infty$. (b) $R_x/a=R_y/b=5$. (c) $R_x/a=5;R_y/b=\infty$. (d) $R_x/a=5;R_y/b=10$. (e) $R_x/a=5;R_y/b=-5$

tainties in temperature distribution and material behavior, and to optimize by reducing gradient indexes and considering material sensitivity to temperature.

5.4.2 Optimization of Boundary conditions effect

For optimal thermal buckling performance, fully clamped boundary conditions (CCCC) are the most favorable, as they provide the greatest stiffness, resulting in the highest buckling temperature rise. This is due to the fact that clamped edges restrict both translation and rotation, offering maximum resistance to deformation under thermal loads. Simply supported boundaries (CSCS) offer moderate resistance, allowing rotation at some edges, which leads to lower stiffness and a reduced buckling temperature rise compared to fully clamped boundaries. Clamped-free boundaries (CFCF), exhibit the lowest stiffness and, therefore, the lowest buckling temperature rise, making them the least optimal choice for thermal buckling resistance.

5.5 Conclusion

In this chapter, the thermal buckling behavior of bi-directional functionally graded shell panels with various geometries has been examined using higher-order shear deformation theory (HSDT) and the p-version finite element method. The study explores the effects of functionally graded material (FGM) gradient indexes, thickness ratio, aspect ratio, and boundary conditions on buckling behavior. The findings show that each parameter significantly impacts the shell panel's behavior. The accuracy of the numerical results has been thoroughly validated, and the study also investigates the effects of different temperature distributions and the assumption of material dependence or independence. Key points from this investigation include:

- Assuming a uniform temperature distribution can lead to significantly different results for the buckling load parameter compared to using linear or non-linear temperature distributions, which are considered more realistic.
- Whether assuming temperature-dependent or independent material properties, the results have consistently shown minimal differences throughout this study. While this assumption does not significantly affect outcomes for smaller temperature changes,

for substantial temperature variations, assuming temperature independence can be misleading.

- The first buckling mode shape remains consistent regardless of the gradient index values, whether the boundary condition is clamped or simply supported, and corresponds to a bending mode. However, from the second mode onward, the mode shape of the shell panel is significantly influenced by both the gradient index values and the type of boundary condition applied.

- A notable limitation of the theory used is that the shear stress-free condition is not met at the top and bottom surfaces of the shell panel, especially in thicker shells. Nonetheless, the theory provides a realistic and accurate estimation of stress distribution for moderately thick panels. For thicker panels, it is recommended to introduce correction factors to satisfy these conditions.

- The boundary conditions of the shell panel play a crucial role in its buckling behavior. In ascending order (CFCF $<$ CSCS $<$ CCCC), different buckling loads are observed for each scenario.

- In all cases presented in this chapter, both linear and non-linear temperature distributions produce relatively similar results. However, for larger temperature changes and thicker shell panels, the discrepancy between these two assumptions is expected to be more significant.

Generale Conclusion

This thesis presents a detailed analysis of the static bending, free vibration, and thermal buckling behavior of bi-directional functionally graded shell panels, utilizing third-order shear deformation theory (TSDT) and the p-version finite element method (FEM). The findings from each chapter underscore the complex and multifaceted mechanical responses of these advanced materials, providing essential insights for optimizing structural design and enhancing engineering applications.

5.6 Static Bending Analysis

The study of linear flexural behavior for various geometries of functionally graded (FG) shell panels, including spherical, cylindrical, hyperbolic, and elliptical shapes, reveals several key insights:

1) **Sandwich Layup Configuration**: The stress distribution across the structural element is significantly influenced by the configuration of sandwich layups, which has a profound impact on overall structural behavior.

2) **Geometric and Material Influences**: The geometric intricacies of shell panel design, coupled with the composition of functionally graded materials, notably affect the structural responses, adding complexity to the behavior of the panels.

3) **Gradient Index Values**: These values play a crucial role in deflection and stress distribution, serving as a lever for fine-tuning structural performance and optimizing design parameters for enhanced functionality and resilience.

5.7 Free Vibration Analysis

The exploration of free vibration responses for sandwich FG shell panels of diverse geometries underscores the following points:

1) **Influence of Factors**: Porosity distribution, magnitude, gradient index, curvature ratio, and sandwich layups all have profound effects on the vibrational behavior of the shell panels.

2) **Nuanced Dynamics**: The interplay of these factors highlights the complex dynamics governing the free vibration responses, offering valuable insights that enhance understanding and pave the way for further research and innovation in structural design and engineering optimization.

5.8 Thermal Buckling Analysis

The examination of thermal buckling behavior using higher-order shear deformation theory (HSDT) and the p-version FEM reveals critical findings:

1) **Temperature Distribution Assumptions**: Uniform temperature distributions can lead to significantly different buckling load parameters compared to linear or non-linear distributions, which are more realistic.

2) **Material Property Assumptions**: Assuming temperature-independent material properties can be misleading for substantial temperature variations, though minimal differences are observed for smaller changes.

3) **Mode Shape Consistency**: The first buckling mode shape remains consistent across different gradient index values and boundary conditions, while subsequent modes are influenced by these factors.

4) **Shear Stress-Free Condition**: The theory does not meet the shear stress-free condition at the top and bottom surfaces for thicker shells, suggesting the need for correction factors in such cases.

5) **Boundary Conditions**: The buckling behavior is heavily influenced by boundary conditions, with different loads observed in ascending order (CFCF $<$ CSCS $<$ CCCC).

6) **Temperature Distribution Impact**: Linear and non-linear temperature distributions produce similar results for smaller temperature changes, but discrepancies increase for larger changes and thicker panels.

5.9 Synthesis and Implications

The combined findings from the static bending, free vibration, and thermal buckling analyses highlight the critical role of material composition, gradient indexes, geometric configurations, and boundary conditions in determining the mechanical behavior of bi-directional functionally graded shell panels. These insights provide a robust foundation for optimizing the design and performance of FGMs in practical applications. The research underscores the necessity of considering realistic temperature distributions and material dependencies to achieve accurate and reliable predictions of structural behavior under various loading conditions.

Overall, this thesis advances the understanding of FG shell panels and their complex responses, contributing valuable knowledge to the fields of material science and structural engineering. The methodologies and conclusions presented can inform future studies and guide the development of more efficient and resilient structural components in engineering applications.

5.10 Future Scope

- The current investigation of functionally graded (FG) structures can be further enhanced by taking into account the initial geometric imperfections and the presence of elastic foundations.

- The porosity distribution in this study has been treated as a function solely of the thickness direction, reflecting the accumulation of debris on the projection nozzle during the manufacturing process. However, this model could be refined to incorporate additional factors contributing to this type of defect. By exploring these other potential influences, a more comprehensive understanding of porosity behavior could be achieved, leading to improved predictions and quality control in the fabrication of functionally graded materials.

- An in-depth analysis of both damped free vibration and forced vibration can be conducted for functionally graded (FG) shell panels. This investigation could involve examining the dynamic response of the panels under various loading conditions and damping scenarios. By exploring the effects of material grading, geometry, and boundary conditions, the study can provide valuable insights into the vibrational characteristics and stability of FG shell structures. Furthermore, it could incorporate numerical simulations alongside experimental validations to enhance the reliability of the results. This comprehensive approach would not only improve our understanding of the vibrational behavior of FG shell panels but also inform design practices and engineering applications in fields such as aerospace, civil engineering, and mechanical systems.

- The formulation could be advanced to a quasi-three-dimensional solution, which would offer a more realistic representation of the physical behavior of the system. By incorporating this approach, the analysis can capture the nuanced variations in stress and strain distribution throughout the thickness of the structure, rather than simplifying them to a two-dimensional model.This enhancement would enable a better understanding of complex interactions within the material, particularly in scenarios involving varying mechanical properties, boundary conditions, and load applications. Additionally, a quasi-three-dimensional formulation can improve the accuracy of predictions related to stability, deformation, and dynamic response under different operating conditions. Ultimately, this more sophisticated modeling technique could lead to more reliable design and optimization of structures in practical applications, particularly in engineering fields where precise performance assessment is critical.

- The formulation could also be enhanced by adopting Deep Shell Theory, which provides a more comprehensive and generalized framework for analyzing shell structures. This theoretical approach accounts for the intricate interactions between bending and membrane actions, enabling a more accurate representation of the mechanical behavior of shells under various loading conditions.By incorporating Deep Shell Theory, the model can effectively address the complexities associated with varying material properties, geometrical configurations, and boundary constraints. This upgrade would allow for a more robust analysis of stresses, strains, and deformations, particularly in scenarios where traditional shell theories may fall short.Moreover, the application of Deep Shell Theory could facilitate a deeper understanding of phenomena such as buckling, vibration, and dynamic response in shells of varying thicknesses and shapes. Ultimately, this more general formulation would not only enhance predictive capabilities but also expand the potential applications of the model in fields such as aerospace engineering, civil construction, and mechanical design, where the performance of shell structures is critical to overall system integrity and reliability.

- The integration of this formulation with an isogeometric modeling framework represents a significant advancement in the capability to analyze complex geometries.

This combination leverages the strengths of both techniques, allowing for a more seamless representation of intricate shapes and boundaries that are often encountered in engineering applications.One of the primary advantages of this integrated approach is the ability to utilize for instance the Non-Uniform Rational B-Splines (NURBS) for geometric representation. NURBS offer a flexible and precise means of modeling complex surfaces, enabling the accurate capture of features that traditional finite element methods, particularly the h-version, might struggle with due to their reliance on mesh discretization. By employing isogeometric analysis, the need for extensive meshing is reduced, which not only streamlines the computational process but also enhances the fidelity of the simulation results.Together, the integration of p-FEM with isogeometric modeling can significantly enhance the analysis of structures with complex geometries, facilitating more accurate predictions of mechanical behavior under various loading conditions. This approach opens new avenues for research and practical applications, particularly in fields such as aerospace, automotive, and civil engineering, where the performance of components with intricate shapes is critical to overall system reliability and efficiency.

- Conducting a non-linear vibration and post-buckling analysis using this formulation presents a fascinating research opportunity with significant implications for the understanding of structural behavior. Non-linear vibration analysis is essential for accurately capturing the complex response of structures subjected to large deformations, which is particularly relevant in scenarios where traditional linear models may not suffice.By employing this formulation, the study could explore the intricate interactions between material non-linearity, geometric non-linearity, and dynamic effects during both vibration and post-buckling phases. This comprehensive approach would allow for the examination of critical phenomena such as mode coupling, energy transfer, and the influence of various loading conditions on structural stability.Additionally, integrating post-buckling analysis would enable the investigation of the structural integrity and performance of shell panels beyond the initial buckling point, providing insights into their load-carrying capacity and potential failure mechanisms.Such an analysis could have far-reaching applications in diverse fields, including aerospace engineering, where understanding the behavior of lightweight structures under dynamic loads is crucial, and civil engineering, particularly in assessing the resilience of slender structures subjected to environmental forces. Overall, this research direction would contribute significantly to advancing knowledge in structural dynamics and design optimization.

Bibliography

[1] A. Houmat. Mapped infinite p-element for two-dimensional problems of unbounded domains. *Computers and Geotechnics*, 35:608–615, 7 2008.

[2] J. N. Reddy and C. D. Chin. Thermomechanical analysis of functionally graded cylinders and plates. *Journal of Thermal Stresses*, 21:593–626, 1998.

[3] Yufeng Xing and Zekun Wang. Closed form solutions for thermal buckling of functionally graded rectangular thin plates. *Applied Sciences (Switzerland)*, 7, 2017.

[4] Chi Zhang, Fei Chen, Zhifeng Huang, Mingyong Jia, Guiyi Chen, Yongqiang Ye, Yaojun Lin, Wei Liu, Bingqing Chen, Qiang Shen, Lianmeng Zhang, and Enrique J. Lavernia. Additive manufacturing of functionally graded materials: A review. *Materials Science and Engineering: A*, 764:138209, 9 2019.

[5] Ammar Melaibari, Salwa A. Mohamed, Amr E. Assie, Rabab A. Shanab, and Mohamed A. Eltaher. Free vibration characteristics of bidirectional graded porous plates with elastic foundations using 2d-dqm. *Mathematics 2023, Vol. 11, Page 46*, 11:46, 12 2022.

[6] Rahul Kumar, Karan K. Gupta, Jigyasa Singh, and Jeeoot Singh. Radial basis collocation method for free vibration analysis of elastically supported porous bidirectional fgm plate under various types of porosity distribution. *Advances in Materials and Processing Technologies*, 9:368–390, 4 2023.

[7] Rahul Saini, Renu Saini, Ashok Kumar, and Mohamed Amine Khadimallah. Free axisymmetric vibrations of heated non-uniform bi-directional fgm mindlin rings employing quadrature approaches. *Thin-Walled Structures*, 184:110482, 3 2023.

[8] Soheil Hashemi, Pouria Karimi Shahri, Sahar Beigzadeh, Farshad Zamani, Mehdi Gholizadeh Eratbeni, Mahan Mahdavi, Ali Heidari, Himan Khaledi, and

Mohamadreza Rajabi Reza Abadi. Nonlinear free vibration analysis of in-plane bi-directional functionally graded plate with porosities resting on elastic foundations. *https://doi.org/10.1142/S1758825121501313*, 14, 2 2022.

[9] B. Sidda Reddy, K. Vijaya Kumar Reddy, and B. Chinna Ankanna. Free vibration behavior of bi-directional functionally graded plates with porosities using a refined first order shear deformation theory. *Journal of Computational Applied Mechanics*, 51:374–388, 12 2020.

[10] M. M. Alipour, M. Shariyat, and M. Shaban. A semi-analytical solution for free vibration of variable thickness two-directional-functionally graded plates on elastic foundations. *International Journal of Mechanics and Materials in Design 2010 6:4*, 6:293–304, 10 2010.

[11] Guojun Nie and Zheng Zhong. Dynamic analysis of multi-directional functionally graded annular plates. *Applied Mathematical Modelling*, 34:608–616, 3 2010.

[12] Iman Davoodi Kermani, Mostafa Ghayour, and Hamid Reza Mirdamadi. Free vibration analysis of multi-directional functionally graded circular and annular plates. *Journal of Mechanical Science and Technology 2012 26:11*, 26:3399–3410, 1 2013.

[13] M. Shariyat and M. M. Alipour. A power series solution for vibration and complex modal stress analyses of variable thickness viscoelastic two-directional fgm circular plates on elastic foundations. *Applied Mathematical Modelling*, 37:3063–3076, 3 2013.

[14] Mohammad Mahinzare, Mohammad Mostafa Barooti, and Majid Ghadiri. Vibrational investigation of the spinning bi-dimensional functionally graded (2-fgm) micro plate subjected to thermal load in thermal environment. *Microsystem Technologies 2017 24:3*, 24:1695–1711, 9 2017.

[15] Qui X. Lieu, Seunghye Lee, Joowon Kang, and Jaehong Lee. Bending and free vibration analyses of in-plane bi-directional functionally graded plates with variable thickness using isogeometric analysis. *Composite Structures*, 192:434–451, 5 2018.

[16] M. H. Shojaeefard, H. Saeidi Googarchin, M. Mahinzare, and M. Ghadiri. Free vibration and critical angular velocity of a rotating variable thickness two-directional fg circular microplate. *Microsystem Technologies 2017 24:3*, 24:1525–1543, 11 2017.

[17] Chih Ping Wu and Lu Ting Yu. Free vibration analysis of bi-directional functionally graded annular plates using finite annular prism methods. *Journal of Mechanical Science and Technology 2019 33:5*, 33:2267–2279, 5 2019.

[18] Son Thai, Vu X. Nguyen, and Qui X. Lieu. Bending and free vibration analyses of multi-directional functionally graded plates in thermal environment: A three-dimensional isogeometric analysis approach. *Composite Structures*, 295:115797, 9 2022.

[19] Chao Wang, Jin Ming Koh, Tiantang Yu, Neng Gang Xie, and Kang Hao Cheong. Material and shape optimization of bi-directional functionally graded plates by giga and an improved multi-objective particle swarm optimization algorithm. *Computer Methods in Applied Mechanics and Engineering*, 366:113017, 7 2020.

[20] Kasra Nejad, Mohammad, Zamani Ziaee, Sima Niknejad, Abbas Hadi, and Amin Dehshahri. Free vibrations analysis of arbitrary three-dimensionally fgm nanoplates. *Advances in nano research*, 8:115–134, 2020.

[21] N. Ahlawat and R. Lal. Effect of winkler foundation on radially symmetric vibrations of bi-directional fgm non-uniform mindlin's circular plate subjected to in-plane peripheral loading. *Journal of Solid Mechanics*, 12:455–475, 6 2020.

[22] Mostafa Esmaeilzadeh and Mehran Kadkhodayan. Dynamic analysis of stiffened bi-directional functionally graded plates with porosities under a moving load by dynamic relaxation method with kinetic damping. *Aerospace Science and Technology*, 93:105333, 10 2019.

[23] Neha Ahlawat. Numerical solution for buckling and vibration of bi-directional fgm circular plates. *AIP Conference Proceedings*, 2061:020020, 1 2019.

[24] Pankaj Sharma and Ashish Khinchi. On frequency investigation of bi-directional fgm beam under thermal effect. *Materials Today: Proceedings*, 47:6089–6092, 1 2021.

[25] Ye Tang, Xiaofei Lv, and Tianzhi Yang. Bi-directional functionally graded beams: asymmetric modes and nonlinear free vibration. *Composites Part B: Engineering*, 156:319–331, 1 2019.

[26] Abbas Barati, Amin Hadi, Mohammad Zamani Nejad, and Reza Noroozi. On vibration of bi-directional functionally graded nanobeams under magnetic field. *https://doi.org/10.1080/15397734.2020.1719507*, 50:468–485, 2020.

[27] Li Zhao, Jun Zhu, and Xiao D. Wen. Exact analysis of bi-directional functionally graded beams with arbitrary boundary conditions via the symplectic approach. *Structural Engineering and Mechanics*, 59:101–122, 7 2016.

[28] Mesut Şimşek. Bi-directional functionally graded materials (bdfgms) for free and forced vibration of timoshenko beams with various boundary conditions. *Composite Structures*, 133:968–978, 12 2015.

[29] M. Lezgy-Nazargah. Fully coupled thermo-mechanical analysis of bi-directional fgm beams using nurbs isogeometric finite element approach. *Aerospace Science and Technology*, 45:154–164, 9 2015.

[30] Ye Tang and Qian Ding. Nonlinear vibration analysis of a bi-directional functionally graded beam under hygro-thermal loads. *Composite Structures*, 225:111076, 10 2019.

[31] T. T. Truong, T. Nguyen-Thoi, and Jaehong Lee. Isogeometric size optimization of bi-directional functionally graded beams under static loads. *Composite Structures*, 227:111259, 11 2019.

[32] Le Thi Ha. Free vibration of a bi-directional imperfect functionally graded sandwich beams. *Lecture Notes in Mechanical Engineering*, pages 100–111, 2022.

[33] Isa Ahmadi, Jan Sladek, and Vladimir Sladek. Size dependent free vibration analysis of 2d-functionally graded curved nanobeam by meshless method. *Mechanics of Advanced Materials and Structures*, 2023.

[34] N. V. Viet, W. Zaki, and Quan Wang. Free vibration characteristics of sectioned unidirectional/bidirectional functionally graded material cantilever beams based on finite element analysis. *Applied Mathematics and Mechanics (English Edition)*, 41:1787–1804, 12 2020.

[35] S. M.K. Ohab-Yazdi and M. Kadkhodayan. Free vibration of bi-directional functionally graded imperfect nanobeams under rotational velocity. *Aerospace Science and Technology*, 119:107210, 12 2021.

[36] Mohammad Zamani Nejad and Amin Hadi. Non-local analysis of free vibration of bi-directional functionally graded euler–bernoulli nano-beams. *International Journal of Engineering Science*, 105:1–11, 8 2016.

[37] L. Zhao, W. Q. Chen, and C. F. Lü. Symplectic elasticity for bi-directional functionally graded materials. *Mechanics of Materials*, 54:32–42, 11 2012.

[38] J. Fariborz and R. C. Batra. Free vibration of bi-directional functionally graded material circular beams using shear deformation theory employing logarithmic function of radius. *Composite Structures*, 210:217–230, 2 2019.

[39] Tianzhi Yang, Ye Tang, Qian Li, and Xiao Dong Yang. Nonlinear bending, buckling and vibration of bi-directional functionally graded nanobeams. *Composite Structures*, 204:313–319, 11 2018.

[40] Anup Pydah and R. C. Batra. Shear deformation theory using logarithmic function for thick circular beams and analytical solution for bi-directional functionally graded circular beams. *Composite Structures*, 172:45–60, 7 2017.

[41] Prashik Malhari Ramteke and Subrata Kumar Panda. Free vibrational behaviour of multi-directional porous functionally graded structures. *Arabian Journal for Science and Engineering*, 46:7741–7756, 8 2021.

[42] Hau Nguyen-Ngoc, Thanh Cuong-Le, Khuong D. Nguyen, H. Nguyen-Xuan, and Magd Abdel-Wahab. Three-dimensional polyhedral finite element method for the analysis of multi-directional functionally graded solid shells. *Composite Structures*, 305:116538, 2 2023.

[43] Van Loi Nguyen, Minh Tu Tran, Suchart Limkatanyu, and Jaroon Rungamornrat. Free vibration analysis of rotating fgp sandwich cylindrical shells with metal-foam core layer. *Mechanics of Advanced Materials and Structures*, 30:3318–3331, 2023.

[44] Xiaomin Shan, Anzhong Huang, Xiaomin Shan, and Anzhong Huang. Intelligent simulation of the thermal buckling characteristics of a tapered functionally graded porosity-dpependent rectangular small-scale beam. *Advances in Nano Research*, 12:281, 3 2022.

[45] Pham Van Vinh, Nguyen Van Chinh, and Abdelouahed Tounsi. Static bending and buckling analysis of bi-directional functionally graded porous plates using an improved first-order shear deformation theory and fem. *European Journal of Mechanics - A/Solids*, 96:104743, 11 2022.

[46] Lu Wei and Hai Qing. Bending, buckling and vibration analysis of bi-directional functionally graded circular/annular microplate based on mcst. *Composite Structures*, 292:115633, 7 2022.

[47] Alessandro Fiorini and Giuseppe Ruta. Buckling of circular plates with functional grading in two directions. *Meccanica*, 56:245–252, 1 2021.

[48] Shuangpeng Li, Shijie Zheng, and Dejin Chen. Porosity-dependent isogeometric analysis of bi-directional functionally graded plates. *Thin-Walled Structures*, 156:106999, 11 2020.

[49] Qui X. Lieu, Dongkyu Lee, Joowon Kang, and Jaehong Lee. Nurbs-based modeling and analysis for free vibration and buckling problems of in-plane bi-directional functionally graded plates. *Mechanics of Advanced Materials and Structures*, 26:1064–1080, 6 2019.

[50] Thom Van Do, Dinh Kien Nguyen, Nguyen Dinh Duc, Duc Hong Doan, and Tinh Quoc Bui. Analysis of bi-directional functionally graded plates by fem and a new third-order shear deformation plate theory. *Thin-Walled Structures*, 119:687–699, 10 2017.

[51] Minh Chien Trinh, Tanmoy Mukhopadhyay, and Seung Eock Kim. A semi-analytical stochastic buckling quantification of porous functionally graded plates. *Aerospace Science and Technology*, 105:105928, 10 2020.

[52] M. Arefi. Buckling analysis of the functionally graded sandwich rectangular plates integrated with piezoelectric layers under bi-axial loads. *https://doi.org/10.1177/1099636216642393*, 19:712–735, 4 2016.

[53] Abdelhak Zohra, Rabia Benferhat, Hassaine Daouadji Tahar, and Abdelouahed Tounsi. Analysis on the buckling of imperfect functionally graded sandwich plates using new modified power-law formulations. *Structural Engineering and Mechanics*, 77:797–807, 3 2021.

[54] Mohit Dhuria, Neeraj Grover, and Kavita Goyal. Influence of porosity distribution on static and buckling responses of porous functionally graded plates. *Structures*, 34:1458–1474, 12 2021.

[55] Faraz Kiarasi, Masoud Babaei, Kamran Asemi, Rossana Dimitri, and Francesco Tornabene. Three-dimensional buckling analysis of functionally graded saturated porous rectangular plates under combined loading conditions. *Applied Sciences 2021, Vol. 11, Page 10434*, 11:10434, 11 2021.

[56] D. Chen, J. Yang, and S. Kitipornchai. Buckling and bending analyses of a novel functionally graded porous plate using chebyshev-ritz method. *Archives of Civil and Mechanical Engineering*, 19:157–170, 3 2019.

[57] Jie Yang, Da Chen, and Sritawat Kitipornchai. Buckling and free vibration analyses of functionally graded graphene reinforced porous nanocomposite plates based on chebyshev-ritz method. *Composite Structures*, 193:281–294, 6 2018.

[58] Pin Wang, Zhijian Gao, Feng Pan, Zohre Moradi, Tayebeh Mahmoudi, and Mohamed Amine Khadimallah. A couple of gdqm and iteration techniques for the linear and nonlinear buckling of bi-directional functionally graded nanotubes based on the nonlocal strain gradient theory and high-order beam theory. *Engineering Analysis with Boundary Elements*, 143:124–136, 10 2022.

[59] Rong Zhang, Hongbai Bai, and Xiaochao Chen. The consistent couple stress theory-based vibration and post-buckling analysis of bi-directional functionally graded microbeam. *Symmetry 2022, Vol. 14, Page 602*, 14:602, 3 2022.

[60] Somi Naidu Balireddy and Jeyaraj Pitchaimani. Stability and dynamic behaviour of bi-directional functionally graded beam subjected to variable axial load. *Materials Today Communications*, 32:104043, 8 2022.

[61] Chu Feng Gao, Ying Hui Pan, Wucheng Zhang, Jian Xin Rao, and Yong Huang. Buckling of two-directional functionally graded cylindrical beams based on a high-order cylindrical beam model. *https://doi.org/10.1142/S0219455421500991*, 21, 4 2021.

[62] Yan Ming Ren and Hai Qing. Bending and buckling analysis of functionally graded euler–bernoulli beam using stress-driven nonlocal integral model with bi-helmholtz kernel. *https://doi.org/10.1142/S1758825121500411*, 13, 6 2021.

[63] Talal Salem, Nizar Lajnef, Pengcheng Jiao, Xuyang Li, and Imen Zaabar. Postbuckling of multi-direction anisotropic constrained functionally graded material beams. *https://doi.org/10.1117/12.2593628*, 11589:88–96, 3 2021.

[64] Mohamed A. Attia and Salwa A. Mohamed. Thermal vibration characteristics of pre/post-buckled bi-directional functionally graded tapered microbeams based on modified couple stress reddy beam theory. *Engineering with Computers*, 38:2079–2105, 6 2022.

[65] Doan Trac Luat, Do Van Thom, Tran Trung Thanh, Phung Van Minh, Tran Van Ke, Pham Van Vinh, Doan Trac Luat, Do Van Thom, Tran Trung Thanh, Phung Van Minh, Tran Van Ke, and Pham Van Vinh. Mechanical analysis of bi-functionally graded sandwich nanobeams. *Advances in Nano Research*, 11:055, 7 2021.

[66] Rasha M. Abo-bakr, Rabab A. Shanab, and Mohamed A. Attia. Multi-objective optimization for lightweight design of bi-directional functionally graded beams for maximum frequency and buckling load. *Composite Structures*, 278:114691, 12 2021.

[67] Jian Lei, Yuming He, Zhenkun Li, Song Guo, and Dabiao Liu. Postbuckling analysis of bi-directional functionally graded imperfect beams based on a novel third-order shear deformation theory. *Composite Structures*, 209:811–829, 2 2019.

[68] Farshid Allahkarami, Maryam Ghassabzadeh Saryazdi, and Hasan Tohidi. Dynamic buckling analysis of bi-directional functionally graded porous truncated conical shell with different boundary conditions. *Composite Structures*, 252:112680, 11 2020.

[69] Farshid Allahkarami, Hasan Tohidi, Rossana Dimitri, and Francesco Tornabene. Dynamic stability of bi-directional functionally graded porous cylindrical shells embedded in an elastic foundation. *Applied Sciences 2020, Vol. 10, Page 1345*, 10:1345, 2 2020.

[70] Mohsen Taghizadeh, Masoud Babaei, Rossana Dimitri, and Francesco Tornabene. Assessment of critical buckling load of bi-directional functionally graded truncated conical micro-shells using modified couple stress theory and ritz method. *Mechanics Based Design of Structures and Machines*, 2023.

[71] Vu Hoai Nam, Nguyen Thoi Trung, and Le Kha Hoa. Buckling and postbuckling of porous cylindrical shells with functionally graded composite coating under torsion in thermal environment. *Thin-Walled Structures*, 144:106253, 11 2019.

[72] Van Doan Cao, Hoai Nam Vu, and Thi Phuong Nguyen. Nonlinear electro-thermo-torsional buckling analysis of stiffened functionally graded graphene-reinforced composite laminated toroidal shell segments. *Journal of Engineering Mechanics-asce*, 149, 2 2023.

[73] A. Balakrishna Reddy and K. S.Sai Ram. Buckling of functionally graded carbon nanotube reinforced composite cylindrical shell panel with a cutout under uniaxial compression. *Materials Today: Proceedings*, 49:1865–1869, 1 2022.

[74] A. Hajlaoui, E. Chebbi, and F. Dammak. Three-dimensional thermal buckling analysis of functionally graded material structures using a modified fsdt-based solid-shell element. *International Journal of Pressure Vessels and Piping*, 194:104547, 12 2021.

[75] B. W. Abuteir, E. Harkati, D. Boutagouga, S. Mamouri, and K. Djeghaba. Thermo-mechanical nonlinear transient dynamic and dynamic-buckling analysis of functionally graded material shell structures using an implicit conservative/decaying time integration scheme. *Mechanics of Advanced Materials and Structures*, 29:5773–5792, 12 2022.

[76] Mohamed Saad and Lazreg Hadji. Thermal buckling analysis of porous fgm plates. *Materials Today: Proceedings*, 53:196–201, 1 2022.

[77] M. Shariyat. Dynamic thermal buckling of suddenly heated temperature-dependent fgm cylindrical shells, under combined axial compression and external pressure. *International Journal of Solids and Structures*, 45:2598–2612, 5 2008.

[78] Hadi Babaei, Yaser Kiani, and M. Reza Eslami. Thermal buckling and post-buckling analysis of geometrically imperfect fgm clamped tubes on nonlinear elastic foundation. *Applied Mathematical Modelling*, 71:12–30, 7 2019.

[79] Nguyen Dinh Duc, Kim Seung-Eock, and Do Quang Chan. Thermal buckling analysis of fgm sandwich truncated conical shells reinforced by fgm stiffeners resting on elastic foundations using fsdt. *Journal of Thermal Stresses*, 41:331–365, 3 2018.

[80] Y. Kiani and M. R. Eslami. Thermal buckling and post-buckling response of imperfect temperature-dependent sandwich fgm plates resting on elastic foundation. *Archive of Applied Mechanics*, 82:891–905, 7 2012.

[81] H. Bagheri, Y. Kiani, and M. R. Eslami. Asymmetric thermal buckling of temperature dependent annular fgm plates on a partial elastic foundation. *Computers Mathematics with Applications*, 75:1566–1581, 3 2018.

[82] J. Torabi, Y. Kiani, and M. R. Eslami. Linear thermal buckling analysis of truncated hybrid fgm conical shells. *Composites Part B: Engineering*, 50:265–272, 7 2013.

[83] B. N. Pandya and T. Kant. Finite element analysis of laminated composite plates using a higher-order displacement model. *Composites Science and Technology*, 32:137–155, 1 1988.

[84] Vijay K. Singh and Subrata K. Panda. Nonlinear free vibration analysis of single/doubly curved composite shallow shell panels. *Thin-Walled Structures*, 85:341–349, 12 2014.

[85] R. Javaheri and M. R. Eslami. Thermal buckling of functionally graded plates. *https://doi.org/10.2514/2.1626*, 40:162–169, 5 2012.

[86] Kulmani Mehar, Subrata Kumar Panda, Yuvarajan Devarajan, and Gautam Choubey. Numerical buckling analysis of graded cnt-reinforced composite sandwich shell structure under thermal loading. *Composite Structures*, 216, 2019.

[87] Concepts and applications of finite element analysis.singapore, 2009.

[88] Pham Van Vinh. Analysis of bi-directional functionally graded sandwich plates via deformation theory and finite element method. 2021.

[89] Olek Zienkiewicz, Robert Taylor, and J. Z. Zhu. The finite element method: its basis and fundamentals: Seventh edition. *The Finite Element Method: its Basis and Fundamentals: Seventh Edition*, pages 1–714, 2013.

[90] Barna Szabó, Alexander Düster, and Ernst Rank. The p-version of the finite element method. *Encyclopedia of Computational Mechanics*, 8 2004.

[91] A. M. Zenkour. A comprehensive analysis of functionally graded sandwich plates: Part 1—deflection and stresses. *International Journal of Solids and Structures*, 42:5224–5242, 9 2005.

[92] Van Hau Nguyen, Trung Kien Nguyen, Huu Tai Thai, and Thuc P. Vo. A new inverse trigonometric shear deformation theory for isotropic and functionally graded sandwich plates. *Composites Part B: Engineering*, 66:233–246, 11 2014.

[93] Ashraf M. Zenkour. Bending analysis of functionally graded sandwich plates using a simple four-unknown shear and normal deformations theory:. *http://dx.doi.org/10.1177/1099636213498886*, 15:629–656, 8 2013.

[94] A. M.A. Neves, A. J.M. Ferreira, E. Carrera, M. Cinefra, C. M.C. Roque, R. M.N. Jorge, and C. M.M. Soares. Static, free vibration and buckling analysis of isotropic and sandwich functionally graded plates using a quasi-3d higher-order shear deformation theory and a meshless technique. *Composites Part B: Engineering*, 44:657–674, 1 2013.

[95] Aicha Bessaim, Mohammed S.A. Houari, Abdelouahed Tounsi, S. R. Mahmoud, and El Abbes Adda Bedia. A new higher-order shear and normal deformation theory for the static and free vibration analysis of sandwich plates with functionally graded isotropic face sheets:. *http://dx.doi.org/10.1177/1099636213498888*, 15:671–703, 9 2013.

[96] S. Pradyumna and J. N. Bandyopadhyay. Free vibration analysis of functionally graded curved panels using a higher-order finite element formulation. *Journal of Sound and Vibration*, 318:176–192, 11 2008.

[97] J. Yang and Hui Shen Shen. Free vibration and parametric resonance of shear deformable functionally graded cylindrical panels. *Journal of Sound and Vibration*, 261:871–893, 4 2003.

[98] Atteshamuddin S Sayyad and Yuwaraj M Ghugal. Static and free vibration analysis of doubly-curved functionally graded material shells. *Composite Structures*, 269(May):114045, 2021.

[99] Vuong Nguyen Van Do and Chin Hyung Lee. A new n th-order shear deformation theory for isogeometric thermal buckling analysis of fgm plates with temperature-dependent material properties. *Acta Mechanica*, 230:3783–3805, 10 2019.

[100] K. M. Liew, J. Yang, and S. Kitipornchai. Thermal post-buckling of laminated plates comprising functionally graded materials with temperature-dependent properties. *Journal of Applied Mechanics*, 71:839–850, 11 2004.

[101] Vuong Nguyen Van Do, Minh Tung Tran, and Chin Hyung Lee. Nonlinear thermal buckling analyses of functionally graded plates by a mesh-free radial point interpolation method. *Engineering Analysis with Boundary Elements*, 87:153–164, 2 2018.

[102] Vishesh R. Kar, Subrata K. Panda, and Trupti R. Mahapatra. Thermal buckling behaviour of shear deformable functionally graded single/doubly curved shell panel with td and tid properties. *Advances in materials Research*, 5:205–221, 2016.

Appendix A

Mathematical Formulation

A.1 Element matrices

A.1.1 Strain Array elements

$$
\begin{aligned}
&{\varepsilon^0}_{xx} = \frac{\partial u_0}{\partial x} + \frac{w_0}{R_x}; && {\varepsilon^0}_{yy} = \frac{\partial v_0}{\partial y} + \frac{w_0}{R_y}; && {\varepsilon^0}_{xy} = \frac{\partial u_0}{\partial y} + \frac{\partial v_0}{\partial x} \\
&{\varepsilon^0}_{xz} = \theta_x + \frac{\partial w_0}{\partial x} - \frac{u_0}{R_x}; && {\varepsilon^0}_{yz} = \theta_y + \frac{\partial w_0}{\partial y} - \frac{u_0}{R_y}; && {k^1}_{xx} = \frac{\partial \theta_x}{\partial x} \\
&{k^1}_{yy} = \frac{\partial \theta_y}{\partial y}; && {k^1}_{xy} = \frac{\partial \theta_x}{\partial y} + \frac{\partial \theta_y}{\partial x}; && {k^1}_{xz} = 2\overline{u_0} - \frac{\theta_x}{R_x} \\
&{k^1}_{yz} = 2\overline{v_0} - \frac{\theta_y}{R_y}; && {k^2}_{xx} = \frac{\partial \overline{u_0}}{\partial x}; && {k^2}_{yy} = \frac{\partial \overline{v_0}}{\partial y} \\
&{k^2}_{xy} = \frac{\partial \overline{u_0}}{\partial y} + \frac{\partial \overline{v_0}}{\partial x}; && {k^2}_{xz} = 3\overline{\theta_x} - \frac{\overline{u_0}}{R_x} && {k^2}_{yz} = 3\overline{\theta_y} - \frac{\overline{v_0}}{R_y} \\
&{k^3}_{xx} = \frac{\partial \overline{\theta_x}}{\partial x}; && {k^3}_{yy} = \frac{\partial \overline{\theta_y}}{\partial y}; && {k^3}_{xy} = \frac{\partial \overline{\theta_x}}{\partial y} + \frac{\partial \overline{\theta_y}}{\partial x} \\
&{k^3}_{xz} = -\frac{\overline{\theta_x}}{R_x}; && {k^3}_{yz} = -\frac{\overline{\theta_y}}{R_y}
\end{aligned}
\tag{A.1}
$$

A.1.2 Stifness matrix elements

$$
\begin{aligned}
&[B]_{(1,1)} = \frac{\partial u_0}{\partial x}; \quad [B]_{(1,3)} = \frac{w_0}{R_x}; \quad [B]_{(2,2)} = \frac{\partial v_0}{\partial y}; \quad [B]_{(2,3)} = \frac{w_0}{R_y}\\
&[B]_{(3,1)} = \frac{\partial u_0}{\partial y}; \quad [B]_{(3,2)} = \frac{\partial v_0}{\partial x}; \quad [B]_{(4,1)} = -\frac{u_0}{R_x}; \quad [B]_{(4,3)} = \frac{\partial w_0}{\partial x}\\
&[B]_{(4,4)} = \theta_x; \quad [B]_{(5,2)} = -\frac{v_0}{R_y}; \quad [B]_{(5,3)} = \frac{\partial w_0}{\partial y}; \quad [B]_{(5,5)} = \theta_y\\
&[B]_{(6,4)} = \frac{\partial \theta_x}{\partial x}; \quad [B]_{(7,5)} = \frac{\partial \theta_y}{\partial y}; \quad [B]_{(8,4)} = \frac{\partial \theta_x}{\partial y}; \quad [B]_{(8,5)} = \frac{\partial \theta_y}{\partial x}\\
&[B]_{(9,1)} = 2\overline{u_0}; \quad [B]_{(9,4)} = -\frac{\theta_x}{R_x}; \quad [B]_{(10,5)} = -\frac{\overline{\theta_y}}{R_y}; \quad [B]_{(10,7)} = 2\overline{v_0}\\
&[B]_{(11,1)} = \frac{\partial \overline{u_0}}{\partial x}; \quad [B]_{(12,2)} = \frac{\partial \overline{v_0}}{\partial y}; \quad [B]_{(13,6)} = \frac{\partial \overline{u_0}}{\partial y}; \quad [B]_{(13,7)} = \frac{\partial \overline{v_0}}{\partial x}\\
&[B]_{(14,6)} = -\frac{\overline{u_0}}{R_x}; \quad [B]_{(14,8)} = 3\overline{\theta_x}; \quad [B]_{(15,7)} = -\frac{\overline{v_0}}{R_y}; \quad [B]_{(15,9)} = 3\overline{\theta_y}\\
&[B]_{(16,8)} = \frac{\partial \overline{\theta_x}}{\partial x}; \quad [B]_{(17,9)} = \frac{\partial \overline{\theta_y}}{\partial y}; \quad [B]_{(18,8)} = \frac{\partial \overline{\theta_x}}{\partial y}; \quad [B]_{(18,9)} = \frac{\partial \overline{\theta_x}}{\partial x}\\
&[B]_{(19,8)} = -\frac{\overline{\theta_x}}{R_x}; \quad [B]_{(20,9)} = -\frac{\overline{\theta_y}}{R_y}
\end{aligned}
\tag{A.2}
$$

A.1.3 Geometric Stifness matrix elements

$$
\begin{aligned}
&[B_G]_{(1,1)} = \frac{\partial u_0}{\partial x}; \quad [B_G]_{(1,3)} = \frac{w_0}{R_x}; \quad [B_G]_{(2,1)} = \frac{\partial u_0}{\partial y}; \quad [B_G]_{(3,2)} = \frac{\partial v_0}{\partial x}\\
&[B_G]_{(4,2)} = \frac{\partial v_0}{\partial y}; \quad [B_G]_{(4,3)} = \frac{w_0}{R_y}; \quad [B_G]_{(5,1)} = -\frac{u_0}{R_x}; \quad [B_G]_{(5,3)} = \frac{\partial w_0}{\partial x}\\
&[B_G]_{(6,2)} = -\frac{v_0}{R_y}; \quad [B_G]_{(6,3)} = \frac{\partial w_0}{\partial y}; \quad [B_G]_{(7,4)} = \frac{\partial \theta_x}{\partial x}; \quad [B_G]_{(8,4)} = \frac{\partial \theta_x}{\partial y}\\
&[B_G]_{(9,5)} = \frac{\partial \theta_y}{\partial x}; \quad [B_G]_{(10,5)} = \frac{\partial \theta_y}{\partial y}; \quad [B_G]_{(11,4)} = -\frac{\theta_x}{R_x}; \quad [B_G]_{(12,5)} = -\frac{\theta_y}{R_y}\\
&[B_G]_{(13,6)} = \frac{\partial \overline{u_0}}{\partial x}; \quad [B_G]_{(14,6)} = \frac{\partial \overline{u_0}}{\partial y}; \quad [B_G]_{(15,7)} = \frac{\partial \overline{v_0}}{\partial x}; \quad [B_G]_{(16,7)} = \frac{\partial \overline{v_0}}{\partial y}\\
&[B_G]_{(17,6)} = -\frac{\overline{u_0}}{R_x}; \quad [B_G]_{18,7} = -\frac{\overline{v_0}}{R_y}; \quad [B_G]_{(19,8)} = \frac{\partial \overline{\theta_x}}{\partial x}; \quad [B_G]_{(20,8)} = \frac{\partial \overline{\theta_x}}{\partial y}\\
&[B_G]_{(20,8)} = \frac{\partial \overline{\theta_x}}{\partial y}; \quad [B_G]_{(21,9)} = \frac{\partial \overline{\theta_y}}{\partial x}; \quad [B_G]_{(22,9)} = \frac{\partial \overline{\theta_y}}{\partial y}; \quad [B_G]_{(23,8)} = -\frac{\overline{\theta_x}}{R_x}\\
&[B_G]_{(24,9)} = -\frac{\overline{\theta_y}}{R_y}
\end{aligned}
\tag{A.3}
$$

A.1.4 matrix $[T_l]_{(5\times20)}$ of equation 2.26

$$[T_l] = \begin{bmatrix} 1 & 0 & 0 & 0 & 0 & z & 0 & 0 & 0 & 0 & z^2 & 0 & 0 & 0 & 0 & z^3 & 0 & 0 & 0 & 0 \\ 0 & 1 & 0 & 0 & 0 & 0 & z & 0 & 0 & 0 & 0 & z^2 & 0 & 0 & 0 & 0 & z^3 & 0 & 0 & 0 \\ 0 & 0 & 1 & 0 & 0 & 0 & 0 & z & 0 & 0 & 0 & 0 & z^2 & 0 & 0 & 0 & 0 & z^3 & 0 & 0 \\ 0 & 0 & 0 & 1 & 0 & 0 & 0 & 0 & z & 0 & 0 & 0 & 0 & z^2 & 0 & 0 & 0 & 0 & z^3 & 0 \\ 0 & 0 & 0 & 0 & 1 & 0 & 0 & 0 & 0 & z & 0 & 0 & 0 & 0 & z^2 & 0 & 0 & 0 & 0 & z^3 \end{bmatrix} \tag{A.4}$$